A Pressure Instrument for Measuring Skin Friction on Rough Walls

Thesis by
P. Victor Storm

Department of Mechanical Engineering
McGill University, Montréal, Québec, Canada

Submitted July 1991

A Thesis submitted to the Faculty of Graduate Studies and Research
in partial fulfillment of the requirements for the degree of
Master's of Engineering.

Abstract

Skin friction drag contributes significantly to the total drag of a streamline body and is very dependent on surface roughness conditions. Knowledge of the skin friction on a surface of arbitrary roughness is very desirable; however, since shear stresses are typically two to three orders of magnitude smaller than the dynamic pressures encountered in most fluid flows, skin friction is one of the most difficult flow quantities to measure in practice. Existing methods of measurement either do not apply to a rough surface, or are impractical for use outside the controlled conditions of the laboratory. A need exists for a rugged device capable of measuring the skin friction on a surface of unknown roughness.

The aim of this research is to propose and experimentally investigate a pressure instrument for determining the skin friction on a flat surface over the entire range of roughness from smooth to fully rough. An instrument consisting of three pitot tubes and one static tube is found to be the simplest device satisfying these requirements. The principle of operation of the proposed "three tube" instrument depends on the existence of a logarithmic mean velocity profile in the wall region of the turbulent boundary layer.

The three tube instrument is tested on both smooth and rough surfaces in the boundary layer produced on the floor of the McGill University 914 mm x 610 mm wind tunnel, over the Reynolds number range from approximately $R_\theta = 5 \times 10^3$ to $R_\theta = 18 \times 10^3$. The roughness is created using sandpaper of sizes #40 and #24 glued to the wind tunnel floor, and the experiments are performed over a range of non-dimensional roughness $k_s^+ \equiv k_s u_\tau / \nu$ from 0 to approximately 85.

The local skin friction coefficients determined using the three tube instrument are compared to those obtained by several other means. For the smooth wall tests, results of well-known skin friction laws, Preston tubes, a Clauser plot, and a skin friction balance are compared to those of the three tube instrument.

For the roughness investigations, the skin friction balance and Perry's graphical method are used as the basis for comparison. Over the range of non-dimensional roughness examined, the results of the three tube instrument agree with those obtained by these other techniques. The agreement is within the experimental uncertainty of approximately 10 percent. Better accuracy and reduced experimental error are expected with improved instrumentation and measurement techniques.

Résumé

La traînée dûe à la contrainte de cisaillement à la paroi contribue considérablement à la traînée totale sur un objet profilé, et elle dépend de la rugosité à la surface. La connaissance du frottement à une paroi de rugosité arbitraire est donc très importante. Cependant, l'ordre de grandeur des forces de cisaillement est habituellement cent à mille fois plus petits que celui d'inertie dans la plupart des écoulements. Ainsi, le frottement représente une des quantités les plus difficiles à mesurer en situation pratique. Les méthodes existantes qui sont basées sur l'hypothèse de similarité ne peuvent s'adapter aux surfaces rugueuses. De plus, une mesure directe par balance de frottement pourrait être effectuée à une surface de presque n'importe quelle condition, mais est extrêmement difficile et peu réaliste hors de l'environnement contrôlé en laboratoire. Evidemment, un besoin existe pour un appareil robuste qui est capable de mesurer la contrainte de cisaillement à la paroi pour une rugosité indéterminée.

Cette recherche expérimentale propose et analyse un instrument de mesure de pression qui détermine la contrainte de cisaillement sur une surface plane, couvrant une échelle de rugosité partant du régime à comportement lisse, jusqu'au régime aérodynamique ≪pleinement rugueux≫. Un instrument qui consiste en trois tubes de Pitot et un tube statique est l'appareil le plus simple qui satisfasse ces objectifs. Cet appareil se sert de la distribution logarithmique de vitesse dans la région de paroi de la couche limite turbulente.

Cet instrument à ≪trois tubes≫ a été mis à l'essai sur le plancher de la soufflerie 914 mm x 610 mm de l'Université McGill, pour une marge de nombre de Reynold allant de $R_\theta = 5 \times 10^3$ à $R_\theta = 18 \times 10^3$. Les rugosités étaient créées par deux surfaces de papier sablé, de formats #40 et #24, collées au plancher de la soufflerie. Les expériences étaient effectuées sur une plage de la rugosité adimensionelle, $k_s^+ \equiv k_s u_\tau / \nu$, s'étendant de zero à environ 85.

Les coefficients de frottement locaux, déterminés par l'instrument à trois tubes, sont comparés à ceux obtenus par d'autres moyens. Pour les mesures à la paroi lisse, les résultats sont comparés aux lois bien connues, aux tubes de Preston, et à une balance de frottement; pour celles des parois rugueuses, seulement une balance de frottement a été utilisée. Les résultats sont en accord compte tenu de l'incertitude expérimentale de ± 10 pour-cent. On s'attend à une meilleure exactitude avec une instrumentation et des méthodes de mesure améliorées.

Acknowledgments

Much thanks and credit are due to my supervisor, Dr. B. G. Newman, for his guidance and direction, and who's experience in fluid mechanics was indeed tremendously useful as a source of expertise, knowledge and influence.

Special thanks goes to Dr. John Dickinson of l'Université Laval for the use of his skin friction balance and the considerable help he provided. I am very grateful for his co-operation in this research. Credit is also due to Yvon Chalifour of l'Université Laval for his machining work in customizing the skin friction balance for this investigation.

I would also like to thank Steve Markhauser, technician for the aerodynamics laboratories at McGill University, for building most of the experimental apparatus; and Stéphane Cyr and John Saabas for many delightful discussions on turbulence, boundary layers, and related topics.

This research was financially supported by the Natural Sciences and Engineering Research Council of Canada.

Table of Contents

List of Figures

Nomenclature

Greek Symbols

δ	Boundary layer thickness
δ^*	Displacement thickness
Δ	Non-dimensional pressure gradient $(\nu/\rho u_\tau^3)(d\overline{p}/dx)$
Δ_{ij}	Total pressure difference $\overline{P}_i - \overline{P}_j$
ϵ	Location of y origin below top of roughness
ς	Geometrical factor, s_{23}/s_{12}, of instrument
θ	Momentum thickness
κ	Von Kármán constant (≈ 0.41)
λ	Skin friction parameter $\sqrt{2/c_f}$
μ	Fluid dynamic viscosity
ν	Fluid kinematic viscosity μ/ρ
ρ	Fluid density
τ	Total shear stress
τ_w	Wall shear stress

Roman Symbols

A	Constant term in logarithmic velocity defect law
B	Universal log law constant (≈ 5.5)
c_f	Local skin friction coefficient $\tau_w/\overline{Q}$
d_0	Pitot tube diameter
d_e	Pitot tube displacement
H	Shape factor δ^*/θ
i	Pitot tube number index
k	Characteristic roughness dimension
k_s	Nikuradse sand roughness scale
k_s^+	Non-dimensional sand roughness $k_s u_\tau/\nu$
$\overline{p}$	Temporal mean static pressure
$\overline{P}$	Temporal mean total pressure
$\overline{P}_i$	Mean total pressure at i^{th} pitot tube
$\overline{q}$	Temporal mean dynamic pressure $\frac{1}{2}\rho\overline{u}^2$
$\overline{q}_i$	Mean dynamic pressure at i^{th} pitot tube
$\overline{Q}$	Temporal mean free-stream dynamic pressure $\frac{1}{2}\rho\overline{U}^2$
R_x	Reynolds number $x\overline{U}/\nu$
R_θ	Reynolds number $\theta\overline{U}/\nu$
s_{ij}	Pitot tube separation $y_i - y_j$
$\overline{u}$	X-coordinate temporal mean velocity
u'	X-coordinate fluctuating turbulent velocity
$\overline{u}_i$	X-coordinate mean velocity at i^{th} pitot tube
u_{ij}	X-coordinate average mean velocity $(\overline{u}_i + \overline{u}_j)/2$
u_τ	Wall friction velocity $\sqrt{\tau_w/\rho}$
u^+	Non-dimensional mean velocity $\overline{u}/u_\tau$
$\overline{U}$	Temporal mean local free-stream velocity
$\Delta u/u_\tau$	Velocity shift function due to roughness
$\overline{v}$	Y-coordinate temporal mean velocity
v'	Y-coordinate fluctuating turbulent velocity
$\overline{w}$	Z-coordinate temporal mean velocity
x	Coordinate parallel to free-stream flow
y	Coordinate perpendicular to wall
y_i	Vertical position of i^{th} pitot tube
y_{ij}	Vertical position $(y_i + y_j)/2$
y^+	Non-dimensional vertical position yu_τ/ν

Chapter 1

INTRODUCTION

1.1 Aim of the Present Research

The aim of this research is to develop a pressure instrument for the measurement of skin friction on a flat surface. The instrument is desired for determination of skin friction on both smooth and rough surfaces, and is to be rugged enough for use in practical applications, particularly in a marine environment.

Theoretical considerations of the simplest possible pressure instruments are given, beginning with a single pitot tube, followed by multi-tube devices. Both one and two tube instruments are rejected theoretically as being insufficient to satisfy the requirements as stated above. A three tube instrument, however, is shown to be sufficient for the determination of local skin friction on both smooth and rough walls. The principle of operation of the proposed three tube instrument is developed and the device is investigated experimentally to determine its validity over a wide range of surface roughness.

1.2 Range of the Investigation

The three tube instrument was tested at a fixed station on the floor of the McGill 914 mm x 610 mm wind tunnel. The free-stream velocity was varied from about 20 m/s to 45 m/s, providing a range of Reynolds number from approximately $R_\theta = 5000$ to $R_\theta = 18000$, where θ is the momentum thickness.

Tests were performed on a smooth wall and on roughness created using two different sizes of sandpaper, #40 and #24, glued to the floor. The investigations were performed over a range of the non-dimensional roughness parameter $k_s^+ \equiv$

$k_s u_\tau/\nu$ from zero for the smooth wall to approximately 85 for the #24 sandpaper at the maximum Reynolds number. These tests therefore investigate the three roughness régimes from smooth to fully rough walls.

All experiments were performed in a small favourable pressure gradient, whose magnitude was limited to the range $-0.0005 \leq \Delta \leq -0.0001$, where $\Delta \equiv (\nu/\rho u_\tau^3)(dp/dx)$. No investigation was made into the applicability of the instrument in large favourable or adverse pressure gradients.

1.3 Outline of the Thesis

The thesis is roughly divided into two parts: the first half being devoted to the theoretical considerations of the pressure instrument, and the second half describes the experimental investigation and results.

Chapters 2 to 4 are intended to provide a summary of relevant material leading up to the theoretical development of the proposed instrument. Chapter 2 presents an historical background of investigations into both smooth and rough wall turbulent boundary layers, with an emphasis on the law of the wall and roughness. Chapter 3 gives a brief summary of relevant equations of the turbulent boundary layer, concentrating on the mean velocity profile equations for both smooth and rough wall boundary layers which are of great importance in this research. The established methods of determining skin friction are described in Chapter 4 to provide a framework in which the proposed instrument is to be considered.

Chapter 5 introduces the proposed three tube instrument, providing a rationale for the device and its principle of operation. Other instruments which were considered but rejected are also described in this chapter.

The experimental research is presented in the last three chapters. Chapter 6 describes the experimental apparatus and procedure. Chapter 7 gives the experimental results and discussion, including an uncertainty analysis, and Chapter 8 presents the conclusions of this research.

Several appendices are also included to provided extra details on certain theoretical and experimental aspects of this research. These appendices are intended to be supplemental and may be omitted without loss of comprehension.

Chapter 2

HISTORICAL BACKGROUND

This chapter presents a brief historical summary of experimental and analytical work relevant to this research. For brevity, emphasis is placed on the logarithmic region of the turbulent boundary layer and investigations into rough wall boundary layers; much other work concerning turbulent boundary layers is omitted.

2.1 The Turbulent Boundary Layer and the Logarithmic Region

The concept of the boundary layer was first proposed by Prandtl [37] in 1904; however, most investigations into turbulent boundary layers did not begin until the 1920's. During this period, von Kármán [58] proposed a similarity hypothesis for the mean velocity in the turbulent boundary layer. This hypothesis stated that in the region where the turbulent shear dominates the difference between the mean velocity and the free-stream velocity, non-dimensionalized by the wall friction velocity, is independent of viscosity; hence, it is a unique function of y/δ for all flat plate turbulent boundary layers in the absence of a longitudinal pressure gradient.

Shortly afterwards, Prandtl [38] reasoned that there exists a region of the boundary layer near the wall where the wall shear stress would have such a large influence on the flow that all the properties of the flow would be independent of the outer flow variables. In this *law of the wall,* the mean velocity profile depends only on the fluid properties, conditions at the wall, and distance from the wall. Prandtl [39] also proposed that in the upper part of the wall region the turbulent

mixing length is proportional to the distance from the wall, thereby obtaining a logarithmic distribution of the mean velocity profile.

This *logarithmic region* was later derived from several other approaches. Millikan [61] showed that the logarithmic velocity profile is a consequence of the law of the wall and von Kármán's similarity law applying simultaneously in this region of the boundary layer. The dimensional analysis leading to this result is presented by Rotta [44], Head and Rechenberg [18], and Patel and Head [31]. The logarithmic velocity profile was also derived by Townsend [55] through the idea of local equilibrium in the rates of production and dissipation of turbulence energy. Furthurmore, Rotta [43] showed that the logarithmic region can also be derived using the idea that the velocity gradient is independent of viscosity in this region because the laminar shear stress is insignificant in comparison to the turbulent shear stress.

Experimental verification of the logarithmic velocity distribution has been made by many researchers. The first attempt to determine the constants of the logarithmic profile was in 1930 by Nikuradse [61]. The constants were investigated extensively later by Coles [10,11], Coles and Hirst [12], and Clauser [7]. Ludwieg and Tillmann [20] demonstrated that the logarithmic law is valid in boundary layers with mild pressure gradients, while Patel and Head [30,31] showed that the log law breaks down in strong adverse pressure gradients and in highly accelerated boundary layer flows. Coles and Hirst [12] determined the range of validity of the log law in smaller adverse pressure gradients.

In 1956, Clauser [8] demonstrated that the logarithmic profile is universally true for both fully developed pipe flows and boundary layers; shortly afterwards Coles [11] showed that at small Reynolds numbers, $R_\theta \leq 500$, the logarithmic profile extends throughout most of the boundary layer.

2.2 Roughness and the Logarithmic Region

The earliest studies into flows over rough surfaces took place in pipes and channels, since the resistance could be calculated from the loss of head. Investigations into the roughness problem was performed as early as 1858 by Darcy [19], but the first significant results were obtained by Nikuradse [27] in 1933. His work with sand-roughened pipes led to the discovery of three different roughness

régimes which depend on the size of the roughness elements. These three régimes are *effectively smooth*, *intermediate rough*, and *fully rough* in order of increasing roughness size. Nikuradse's sand grain roughness height has since been widely used as the standard for roughness measurement. Schlichting [45] discovered in 1936 that the roughness density and geometry were also needed to describe the roughness effect adequately, and he found a method of determining the equivalent sand roughness from the velocity profile produced on a surface whose roughness is other than sand. In 1944, Moody [24] measured the resistance of commercially rough pipes and presented the results graphically, creating what is now referred to as the Moody diagram.

The first analytical work on developing boundary layers on a rough surface was performed in 1934 by von Kármán, who analyzed Nikurdse's pipe data to produce a friction law for a flat plate in the fully rough régime [59]. Von Kármán's relation was an implicit expression for the skin friction; consequently, Prandtl and Schlichting obtained an analytical expression for the fully rough régime, which gives the skin friction explicitly [40].

Early experimental work on boundary layer development over a rough plate was done by Tillmann (1945), Bains (1950) [19], and Moore (1951) [25], the latter using roughness consisting of square bars placed transverse to the flow. An important experimental investigation was performed by Hama (1954) using wire screen roughness [17]. He showed that the difference between the skin friction on a rough surface and that on a smooth surface at the same Reynolds number can be determined from the logarithmic velocity profile.

Much experimental work on rough wall boundary layers was performed by Perry and Joubert who showed that, with the correct origin for the vertical position, the rough wall turbulent boundary layer also contains a logarithmic region [32]. Furthermore, they demonstrated that the effect of the roughness on the logarithmic region is a reduction of the velocity by an amount which depends on the roughness parameter k_s^+, but is independent of the vertical position [32]. Later, Perry [34] also showed that this velocity shift is independent of the pressure gradient.

Chapter 3

TURBULENT BOUNDARY LAYER EQUATIONS

This chapter contains a review of the equations of a turbulent boundary layer useful for the purpose of this research. This review is intended as a brief summary only and is included here merely for completeness. The reader familiar with this material may prefer to skip this chapter and continue in Chapter 4; those who wish more detail can consult any reference devoted to turbulence and boundary layers. Consistent with the usual convention, the co-ordinate system is right-handed cartesian, with x in the direction of the free-stream flow, and y normal to the flat surface.

3.1 Equations of Continuity and Momentum

The general two-dimensional boundary layer equations for an incompressible, Newtonian fluid of constant viscosity were developed by Prandtl from the equation of continuity and the Navier-Stokes equation. Through the application of Reynolds averaging to these instantaneous equations, one obtains turbulent boundary layer equations for the time-averaged mean flow. The steady-state equations of continuity and momentum are

$$\frac{\partial \overline{u}}{\partial x} + \frac{\partial \overline{v}}{\partial y} = 0, \tag{3.1}$$

$$\overline{u}\frac{\partial \overline{u}}{\partial x} + \overline{v}\frac{\partial \overline{u}}{\partial y} + \frac{\partial}{\partial x}(\overline{u'^2}) + \frac{\partial}{\partial y}(\overline{u'v'}) = -\frac{1}{\rho}\frac{\partial \overline{p}}{\partial x} + \nu\frac{\partial^2 \overline{u}}{\partial y^2}, \tag{3.2}$$

and

$$\frac{\partial}{\partial y}(\overline{v'^2}) = -\frac{1}{\rho}\frac{\partial \overline{p}}{\partial y}. \tag{3.3}$$

In most circumstances, the terms containing $\overline{u'^2}$ and $\overline{v'^2}$ are small in comparison with the other terms and can be neglected. Hence, the static pressure is approximately invariant with y at any given x-wise position, and the x-momentum equation becomes

$$\overline{u}\frac{\partial \overline{u}}{\partial x} + \overline{v}\frac{\partial \overline{u}}{\partial y} + \frac{\partial}{\partial y}(\overline{u'v'}) = -\frac{1}{\rho}\frac{d\overline{p}}{dx} + \nu\frac{\partial^2 \overline{u}}{\partial y^2}. \tag{3.4}$$

The turbulent boundary layer equations for the mean flow differ from the laminar equations only by the term containing $\overline{u'v'}$, a correlation between the streamwise and normal velocity fluctuations. This term behaves mathematically like an additional shear stress, due to the turbulence mixing. The total shear stress, τ, is then defined as the sum of the turbulent and laminar components:

$$\tau \equiv -\rho\overline{u'v'} + \mu\frac{\partial \overline{u}}{\partial y}. \tag{3.5}$$

Using this definition, and writing the pressure derivative in terms of the free-stream velocity, the mean flow continuity and x-momentum equations for a turbulent boundary layer become

$$\frac{\partial \overline{u}}{\partial x} + \frac{\partial \overline{v}}{\partial y} = 0, \tag{3.6}$$

$$\overline{u}\frac{\partial \overline{u}}{\partial x} + \overline{v}\frac{\partial \overline{u}}{\partial y} = \overline{U}\frac{d\overline{U}}{dx} + \frac{1}{\rho}\frac{\partial \tau}{\partial y}. \tag{3.7}$$

The appropriate smooth wall boundary conditions are

$$\overline{u}(x,0) = \overline{v}(x,0) = 0, \qquad \overline{u}(x,\delta) = \overline{U}(x). \tag{3.8}$$

For rough wall boundary layers the latter boundary condition holds equally well; however, the former conditions are not applicable. The true surface boundary conditions require vanishing mean velocity components everywhere on the surface of the roughness elements. Except for regular roughness of a simple geometry, the rough wall boundary conditions would be topologically complex and impossible to apply analytically.

3.2 Momentum Integral Equation

An equation for the local skin friction coefficient can be obtained by direct integration of the x-momentum equation over the boundary layer. The details of this integration are given in Appendix A; however the final result is the momentum integral equation:

$$\frac{d\theta}{dx} + (2+H)\frac{\theta}{\overline{U}}\frac{d\overline{U}}{dx} = \frac{c_f}{2}, \tag{3.9}$$

where

$$H \equiv \frac{\delta^*}{\theta}, \tag{3.10}$$

$$\delta^* \equiv \int_0^\infty \left(1 - \frac{\overline{u}}{\overline{U}}\right) dy, \tag{3.11}$$

$$\theta \equiv \int_0^\infty \frac{\overline{u}}{\overline{U}}\left(1 - \frac{\overline{u}}{\overline{U}}\right) dy, \tag{3.12}$$

and

$$c_f \equiv \frac{\tau_w}{\frac{1}{2}\rho\overline{U}^2}. \tag{3.13}$$

This momentum integral equation describes the balance of forces acting on a slice of the boundary layer of thickness dx. The terms are, respectively, the change in the fluid's inertia, the pressure force and the wall shear force. This equation is strictly incorrect for turbulent boundary layers because of the omission of the terms containing $\overline{u'^2}$ and $\overline{v'^2}$ from the turbulent boundary layer equations given in the previous section. This omission may result in an error of c_f by as much as three percent in the absence of a pressure gradient, and may be considerably worse when a pressure gradient exists.

3.3 Mean Velocity Profile Equations

The general turbulent boundary layer equations for steady two-dimensional flow on a flat plate can not be solved analytically because of the turbulent shear $-\rho\overline{u'v'}$, for which no exact analytical description exists. Fortunately, much understanding of the turbulent boundary layer can be achieved by dimensional analysis, and therefore, this approach will be taken here. However, due to limited space, only the equations relevant to this research will be derived. For a more detailed description of the dimensional analysis, the interested reader may consult any reference dealing with turbulent boundary layers [4,44,46,61,63].

The basis of the boundary layer dimensional analysis is the consideration of the mean velocity profile $\overline{u}$, and its dependence on certain independent variables. At a particular stream-wise position, a complete list of the relevant independent variables would include the vertical position y, the fluid properties ρ and μ, surface parameters τ_w and k_s, free-stream parameters $\overline{U}$ and δ, and the longitudinal pressure gradient $d\overline{p}/dx$. Thus, one has

$$\overline{u} = \mathcal{F}(y, \rho, \mu, \tau_w, k_s, \overline{U}, \delta, \frac{d\overline{p}}{dx}) \tag{3.14}$$

where the symbol $\mathcal{F}$ will be used to indicate some unknown functional relationship in general. In the present investigation, one is only concerned with flows in a very small pressure gradient, so it is assumed that $d\overline{p}/dx$ can be dropped from the list of relevant independent variables. Also, the classical development of boundary layer dimensional analysis starts with the consideration of smooth walls only; therefore, the smooth and rough wall dimensional analysis will be developed separately.

3.3.1 Smooth Wall Dimensional Analysis

Figures 3.1 and 3.2 show the mean velocity profile of a typical turbulent boundary layer on a smooth flat plate in zero pressure gradient. By considering the total shear stress in the boundary layer, it is useful to split up the boundary layer into a wall and a wake region. The wall region is defined as the region close enough to the wall that the total shear stress can be treated as constant and equal to the wall value. In the wake region, the total shear stress drops from the wall value to zero at the edge of the boundary layer.

In the wall region Prandtl [38] reasoned that, since the shear stress is constant and equal to that of the wall, the mean velocity must be determined by the wall conditions, and not by the outer flow variables, such as free-stream velocity, boundary layer thickness, or even pressure gradient. Thus,

$$\overline{u} = \mathcal{F}(y, \rho, \mu, \tau_w), \tag{3.15}$$

and non-dimensionalizing gives

$$\frac{\overline{u}}{u_\tau} = f\left(\frac{y u_\tau}{\nu}\right), \tag{3.16}$$

where $u_\tau = \sqrt{\tau_w/\rho}$ is called the wall friction velocity. This expression is known as Prandtl's law of the wall and the function f is called the wall law function.

The wall region can be further divided into three sub-regions depending on the relative importance of the laminar and turbulent components of the shear stress. Immediately next to the wall, the velocity gradient is large and the turbulence is damped out by the influence of the wall. Therefore the laminar shear stress dominates, giving rise to a purely viscous region, known as the viscous sublayer, in which

$$\tau_w = \mu \frac{\partial \overline{u}}{\partial y}, \tag{3.17}$$

and, upon integration, the velocity profile is linear and given by

$$u^+ = y^+, \tag{3.18}$$

where $u^+ \equiv \overline{u}/u_\tau$ and $y^+ \equiv y u_\tau/\nu$. The viscous sublayer extends to approximately $y^+ = 5$, which, at low Reynolds numbers, is about one percent of the boundary layer thickness.

Just above the viscous sublayer, between $y^+ \approx 5$ and $y^+ \approx 30$, is the buffer or blending region, where the laminar and turbulent shear stress components are equal in importance. In this region the production of turbulence is very large [4]; therefore, it is an important region in the understanding of the mechanism creating the turbulence. However, this region is of little interest in the dimensional analysis used to arrive at a description of the mean velocity profile.

The upper, and by far the largest, part of the wall region is characterized by a dominant turbulent shear stress. The large scale turbulent eddies in this region contain most of the turbulent energy and account for the turbulent stress. Direct dissipation of energy from these eddies by the action of viscosity is negligible, and therefore the structure of these large eddies and the turbulent stress are independent of viscosity. Since the mean velocity gradient is determined by the turbulent shear alone, it also is independent of viscosity [44]. Hence

$$\frac{\partial \overline{u}}{\partial y} = \mathcal{F}(y, \rho, \tau_w), \tag{3.19}$$

and therefore

$$\frac{y}{u_\tau}\frac{\partial \overline{u}}{\partial y} = \mathcal{F}(0) \equiv \frac{1}{\kappa}, \tag{3.20}$$

since a function of no criteria of similarity is necessarily a constant. The constant, κ, is called the von Kármán constant. Integrating this expression, one obtains

$$\frac{\overline{u}}{u_\tau} = \frac{1}{\kappa} \ln y + c, \tag{3.21}$$

where c is the constant of integration. Now combining this expression with Prandtl's law of the wall gives the logarithmic velocity profile

$$\frac{\overline{u}}{u_\tau} = \frac{1}{\kappa} \ln \frac{y u_\tau}{\nu} + B, \tag{3.22}$$

where B is a universal constant. Using the non-dimensional variables, this logarithmic profile can be written as

$$u^+ = \frac{1}{\kappa} \ln y^+ + B. \tag{3.23}$$

The values of the two constants have been determined experimentally to be $\kappa \approx 0.41$ and $B \approx 5.5$. This equation is known as the log law, and the region in which it applies is called the logarithmic region. This region extends from about $y^+ = 30$ to typically $y/\delta = 0.2$; however, the upper limit depends on the Reynolds number and the stream-wise pressure gradient.

To complete the dimensional analysis treatment of the smooth wall turbulent boundary layer, von Kármán's similarity concept is given. In the entire boundary layer above the buffer region the laminar shear stress is negligible and the turbulent shear stress dominates. When this is the case, von Kármán [59] reasoned that the wall tends to act merely as a source of retardation, reducing the local mean velocity below the free-stream value in a manner which is independent of the viscosity, but dependent on the wall shear stress and the distance over which the effect has occurred. In a zero longitudinal pressure gradient, this concept is expressed mathematically as

$$\overline{U} - \overline{u} = \mathcal{F}(y, \rho, \tau_w, \delta), \tag{3.24}$$

and non-dimensionalizing gives

$$\frac{\overline{U} - \overline{u}}{u_\tau} = g\left(\frac{y}{\delta}\right). \tag{3.25}$$

This expression is referred to as the velocity defect law, and g is the velocity defect function. This law extends down from the free-stream, and overlaps with

the law of the wall in the logarithmic region. For this reason, the logarithmic region is sometimes referred to in the literature as the overlap region. Here, the velocity defect law takes the form

$$\frac{\overline{U}-\overline{u}}{u_\tau} = -\frac{1}{\kappa}\ln\frac{y}{\delta} + A \tag{3.26}$$

where $A \approx 2.35$ for a flat wall with no longitudinal pressure gradient. This constant is not universal, however, since it depends on the geometry and the pressure gradient.

3.3.2 Rough Wall Dimensional Analysis

In a dimensional analysis of a rough wall boundary layer the first problem one faces is actually characterizing the roughness itself. For an arbitrary rough surface the size, shape, geometry and distribution of the roughness are all important parameters of the surface. However, in an extensive investigation into flows through sand-roughened pipes, Nikuradse [27] found that the effect of the roughness on the flow can be characterized by a single length scale of the roughness which he took to be the sand grain size. Hence, for any rough surface, the effect of the roughness on the flow can be determined in terms of a single length scale of the roughness, k. However, due to the great deal of research into sand roughness, it has become conventional to characterize a rough surface by its equivalent sand roughness, k_s. This enables the derivation of universal friction laws for all rough surfaces, such as the Moody diagram [24], but has the drawback that the sand equivalent roughness can not be determined directly from the surface geometry. For an arbitrary rough surface, k_s is not known a priori, and can only be determined from the boundary layer mean velocity profile. Nevertheless, the simplicity of having a single universal roughness parameter outweighs the disadvantage of the indirect means required to determine this parameter for a given surface.

The other significant difference between the smooth and rough walls is the uncertainty in the origin of the vertical position above a rough surface. The origin of y can not be arbitrarily defined, since the boundary layer equations derived in the following dimensional analysis are only applicable to a specific origin, taken to be a distance ϵ below the top of the roughness elements. As with the equivalent

sand roughness, ϵ can not be determined from the surface geometry alone, but can only be obtained from the boundary layer velocity profile. This does not, however, introduce another independent variable into the dimensional analysis, since the same constraint was applied implicitly to the smooth wall boundary layer. The difference is that, while the origin for y was clearly defined and known on the smooth wall, it is now an unknown independent variable in the rough wall analysis.

Despite these two differences, the rough wall turbulent boundary layer dimensional analysis follows a similar development to that of the smooth wall. The boundary layer still contains the wall and wake regions as previously described, but now the roughness length scale, k_s, must be taken into account accordingly, and the vertical position, y, must now be treated as unknown. As with the smooth wall, in the wall region the mean velocity is influenced by the wall, the fluid properties, and the vertical position; however, the surface roughness must now be included as a characteristic of the wall. Thus,

$$\overline{u} = \mathcal{F}(y, \rho, \mu, \tau_w, k_s), \tag{3.27}$$

and hence

$$\frac{\overline{u}}{u_\tau} = f\left(\frac{y u_\tau}{\nu}, \frac{k_s u_\tau}{\nu}\right) \tag{3.28}$$

which is called the law of the wall for rough surfaces.

As before, the turbulent shear dominates in the upper part of the wall region, and the mean velocity gradient is independent of the viscosity; moreover, it is also independent of the surface roughness, except inasmuch as the viscosity and the roughness influence the wall shear stress. Physically, the roughness behaves in a manner similar to the fluid viscosity because they both affect the turbulence in the wall region by the production of vorticity near the surface. Whereas the roughness increases the production of turbulence near the wall, the turbulence structure away from the wall is determined only by the local rates of production, dissipation, convection and diffusion. Through diffusion, the roughness gives rise to more turbulent energy in the boundary layer, and consequently larger turbulent eddies. However, these eddies behave no differently than they would had they been created by some other mechanism which increases the shear at the wall. In other words the characteristics of the turbulence is the same regardless of whether the production of turbulence is by virtue of vorticity generated by

roughness elements at the surface, or by viscosity-induced vorticity. Hence, the mean velocity gradient is independent of both the viscosity and roughness, so that, with the correct origin for y,

$$\frac{\partial \overline{u}}{\partial y} = \mathcal{F}(y, \rho, \tau_w), \tag{3.29}$$

and

$$\frac{y}{u_\tau}\frac{\partial \overline{u}}{\partial y} = \frac{1}{\kappa}. \tag{3.30}$$

Integrating this relation and combining it with the law of the wall for rough walls gives

$$u^+ = \frac{1}{\kappa}\ln y^+ + C \tag{3.31}$$

where C must be a function of the dimensionless roughness parameter $k_s^+ \equiv k_s u_\tau/\nu$. It is conventional to write this expression as

$$u^+ = \frac{1}{\kappa}\ln y^+ + B - \frac{\Delta u}{u_\tau}\left[k_s^+\right], \tag{3.32}$$

because the effect of the roughness is to decrease the mean velocity everywhere in the logarithmic region by the same amount $\Delta u/u_\tau$ which depends only on k_s^+.

The velocity shift function, $\Delta u/u_\tau$, exhibits three distinct régimes depending on the value of k_s^+. When $k_s^+ < 5$ the roughness is contained within the viscous sublayer. Small turbulent eddies generated by the roughness are rapidly dissipated by viscosity in the viscous sublayer and the wall is said to be effectively smooth. Thus, $\Delta u/u_\tau = 0$, and one obtains the smooth wall log law.

When the roughness is very large in comparison to the viscous sublayer, the roughness elements generate large wakes, and consequently, the wall shear stress is due entirely to form drag on the roughness elements. Thus, the skin friction is independent of Reynolds number and the mean velocity itself is independent of viscosity, and takes the form

$$u^+ = \frac{1}{\kappa}\ln\left(\frac{y}{k_s}\right) + D \tag{3.33}$$

in the logarithmic region. The constant of integration, D is universal and has been found empirically to have the value of approximately 8.5. To obtain this relation, the velocity shift function must be given by

$$\frac{\Delta u}{u_\tau}\left[k_s^+\right] = \frac{1}{\kappa}\ln k_s^+ - 3.0. \tag{3.34}$$

This fully rough régime occurs when $k_s^+ > 70$.

In between these two extremes is the intermediate roughness régime where both the roughness and the viscosity are important parameters in determining the mean velocity profile, and the exact form of the log law can only be obtained empirically.

It should be noted that for boundary layer flows on a flat surface, the skin friction decreases in the flow direction, so that a single flat plate with uniform roughness may exhibit a fully rough boundary layer flow upstream, followed by the intermediate régime and an effectively smooth wall downstream if the plate is sufficiently long.

Regardless of the surface roughness, the slope of the mean velocity profile is given by

$$\frac{y}{u_\tau}\frac{\partial \overline{u}}{\partial y} = \frac{1}{\kappa}. \tag{3.35}$$

This equation holds equally well for both smooth and rough walls; however, for rough walls the origin of y must be taken at a particular position, an unknown distance ϵ below the crests of the roughness.

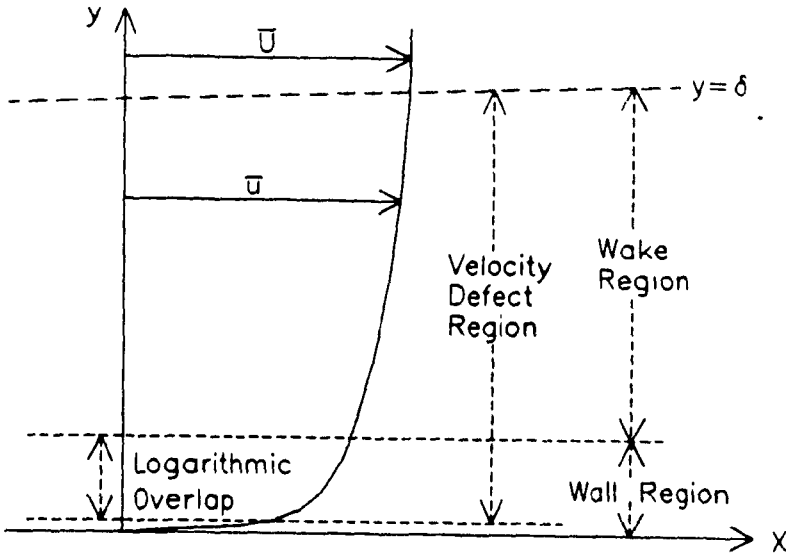

Figure 3.1: Typical Turbulent Boundary Layer Velocity Profile on a Smooth Flat Plate

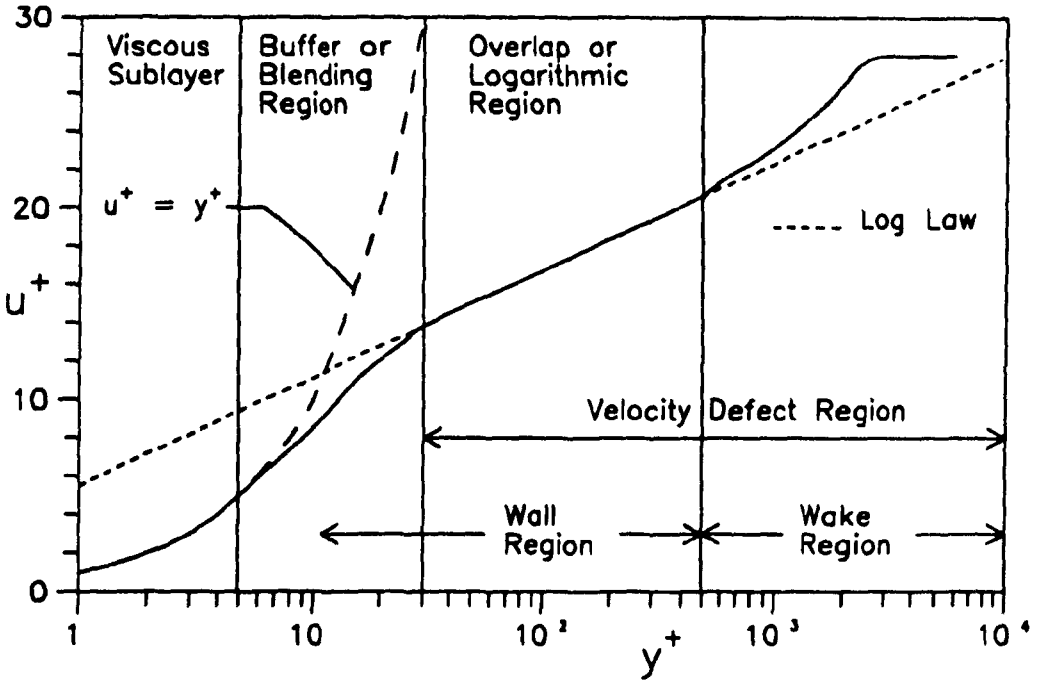

Figure 3.2: Smooth Wall Turbulent Boundary Layer Velocity Profile in Log Law Form Indicating the Various Regions

Chapter 4

SKIN FRICTION DETERMINATION

Since the purpose of this research is to examine a proposed instrument for determining the local skin friction on a flat plate for both smooth and rough surfaces, it is useful to discuss the existing methods of skin friction determination. The small size of the wall shear stress, compared to pressure and inertial forces in the boundary layer, gives rise to much difficulty in the accurate measurement of skin friction. As a result, a great diversity of methods have been developed over many years. A useful classification of the various measurement techniques has been given by Brown and Joubert [5] and is summarized in Figure 4.1. This chapter discusses briefly the most versatile of these measurement techniques, with emphasis on those applicable to rough wall skin friction measurement and those used in this research.

4.1 Direct Measurement

Direct measurement involves the use of a skin friction balance, an instrument which measures the wall shear force directly on a small piece of the wall by means of a "floating element". Such an instrument was used successfully as early as 1929 by Kempf [5], and later used in incompressible investigations in air by Schultz-Grunow, and Smith and Walker [49]. Still others have developed instruments for flat plate measurements at high Mach numbers [9].

The principle of operation of such an instrument is quite simple. The shear stress acting on the surface of the element gives rise to a force which can be

detected by the displacement of the element in an open-loop system, or by the balancing force required to restore the element in a closed-loop system. However, difficulties arise in practice due to other forces which may be acting on the floating element, such as inertial, pressure and vibrational forces. Furthermore, investigations have shown that the force on the element is very dependent upon its vertical position and the size of the gap separating the element from the surrounding surface. Quality control is therefore very crucial to the measurement of skin friction by this technique. Thus, while the instrument is useful in the controlled laboratory environment, the delicacy of the device makes it susceptible to damage and is therefore unsuitable for most practical applications outside the laboratory.

The advantage of the direct measurement is that the surface of the floating element need not be smooth; therefore, this technique can be used to measure skin friction in a variety of surface roughness conditions.

4.2 Dye Traces

The use of dye in oil for surface flow visualization is well established [5]. A drop of dye on the surface produces a trail whose length is proportional to the wall shear stress. Unfortunately, this method is not applicable to a rough surface, and even on a smooth surface it is not accurate enough for quantitative measurements. However, it does provided much qualitative information, particularly regarding the direction of the wall shear stress in complicated flows.

4.3 Momentum Techniques

Momentum techniques make use of the momentum integral equation,

$$\frac{d\theta}{dx} + (2+H)\frac{\theta}{\overline{U}}\frac{d\overline{U}}{dx} = \frac{c_f}{2}, \tag{4.1}$$

to determine the skin friction coefficient, c_f. For fully developed flow in pipes or channels this equation can be integrated over x to yield the overall skin friction coefficient. For external boundary layer flows, however, this equation must be applied to velocity traverse data at frequently spaced intervals in the x-direction.

Values of θ, $\overline{U}$ and H are obtained as functions of x by numerical integration of the profiles.

This method may be applied equally well to smooth and rough wall boundary layers, but is beset by many problems. First among them is the fact that this equation is strictly incorrect by the omission of certain turbulence terms. This may result in incorrect values of c_f by a few percent in the absence of an external pressure gradient, and by a considerably greater error in a non-zero pressure gradient. Another serious problem with this technique is the difficulty in determining precise values of the two quantities θ and H, and in particular, the difficulty of obtaining the derivative of the slowly changing momentum thickness. Finally, the method may be prone to large errors due to secondary flow effects and lack of two-dimensionality.

4.4 Similarity Techniques

Similarity techniques are a collection of many different methods, so named because they make use of the similarity properties of the turbulent boundary layer. The general heading of similarity techniques can be subdivided into methods of measurements based on heat transfer similarity, similarity of flow about obstacles, and similarity of velocity profiles.

4.4.1 Heat Transfer Similarity

Heat transfer similarity is based on the principle that the rate of heat transfer by forced convection from a small heated element of the surface depends only on the wall variables if the thermal boundary layer remains within the wall region of the velocity boundary layer. If the temperature difference between the fluid and the heated element is maintained small enough to avoid natural convection, then a calibrated instrument of this type can be used to determine the wall shear stress. The first such device was introduced by Ludwieg in 1949, while thin-film varieties were later developed by Bellhouse and Schultz [64], and by Brown [5].

This method is applicable to smooth surfaces only, as the presence of roughness will alter considerably the forced convection at the surface of the heated element.

4.4.2 Similarity of Flow about Obstacles

The velocity field about any small obstacle immersed entirely in the wall region of a smooth wall boundary layer depends only on the significant independent variables of the wall region. Therefore, any measurable pressure difference, Δp, will also depend on these wall variables. Then, from the dimensional analysis,

$$\frac{\Delta p l^2}{\rho \nu^2} = \mathcal{F}\left[\frac{\tau_w l^2}{\rho \nu^2}\right], \tag{4.2}$$

where l is a characteristic length scale of the obstacle. An empirical calibration to determine the functional relationship permits the determination of the wall shear stress from the measured pressure difference. If the shape of the obstacle is such that other geometrically similar obstacles can be produced, then the calibration of one device can be used for all similar devices.

Several instruments have been devised based on this principle. The most common are sublayer fences (Head and Rechenberg [18]), razor blades (Wyatt and East [67]), static holes of different diameters (Duffy and Norbury [65]), the Preston tube (Preston [41]), and the Stanton tube (Fage and Falkner [66]).

Probably the most commonly used of these techniques, because of its simplicity, is the Preston tube. Proposed by Preston [41] in 1954, the Preston tube consists of a single flat-ended circular pitot tube sitting directly on the smooth flat surface. The internal to external diameter ratio was fixed at 0.6, and therefore the outer diameter serves as the only geometrically significant length scale. The difference between the total pressure measured by the tube and the local static pressure measured at a surface static hole was calibrated against the wall shear stress, in the form of the above equation. Preston's original calibration was improved upon by Patel [30] in 1965, who also examined the limitations on the use of Preston tubes in strong pressure gradients. The use of a Preston tube combined with Patel's calibration, is considered to be one of the most reliable means of determining the skin friction on a smooth surface.

None of these similarity methods are suitable for rough wall skin friction determination, since in either the instrument sits on the flat surface or a well constructed static pressure hole is needed at the surface. The introduction of roughness elements on the surface would eliminate the possibility of surface static pressure taps, and a device in contact with the surface would certainly introduce uncertainty in its true vertical position.

4.4.3 Velocity Profile Similarity

The self-similarity of the smooth wall turbulent boundary layer mean velocity profile has given rise to several means of determining the coefficient of skin friction. A successful method proposed by Clauser [8] in 1954 is based upon re-writing the logarithmic velocity profile in the form of

$$\frac{\overline{u}}{\overline{U}}\sqrt{\frac{2}{c_f}} = \frac{1}{\kappa}\ln\left(\frac{y\overline{U}}{\nu}\sqrt{\frac{c_f}{2}}\right) + B. \tag{4.3}$$

Clauser showed that the skin friction coefficient could be obtained from this equation by a graphical procedure. A semi-log plot of $\overline{u}/\overline{U}$ versus $y\overline{U}/\nu$ for data points obtained in the logarithmic region yields a straight line whose slope and intercept are both related to c_f. In fact, data points which lie closer to the wall than the logarithmic region also uniquely define a curve corresponding to a specific value of the skin friction coefficient. The Clauser plot method is considered one of the most accurate means of determining the local skin friction coefficient on a smooth flat plate, but has the drawback that a detailed velocity traverse is required.

The affine nature of the smooth wall turbulent boundary layer also permits the derivation of empirical skin friction laws relating the skin friction coefficient to a small number boundary layer similarity criteria. Being based on experimental data, many such relations exist; only the most common will be presented here.

The simplest formulæ are called one-parameter relations because the skin friction is expressed in terms of a Reynolds number only. Von Kármán [59] made the first attempt to derive a one-parameter skin friction formula for a smooth flat plate by combining the velocity defect relation with the momentum integral equation, arriving at a relation in the form

$$c_f = \alpha + \beta\ln(c_f R_x) \tag{4.4}$$

where R_x is the Reynolds number based on the distance from the leading edge of the plate. Schoenherr [47] developed a similar equation for the overall plate skin friction coefficient. Subsequently, Prandtl [40] evaluated the skin friction over the most common range of R_x, and Schlichting fitted the results to a useful formula, in which the skin friction coefficient is given explicitly. These formulae

for the local and overall skin friction coefficients are referred to as the Prandtl-Schlichting relations [4]. The relation for the local skin friction is

$$c_f = 0.455(\log R_x)^{-2.58} \tag{4.5}$$

The Prandtl-Schlichting relations are valid over the Reynolds number range $10^7 \leq R_x \leq 10^9$ for a flat plate boundary layer which is turbulent from the leading edge.

Often, more practical situations require a local skin friction relation in terms of a Reynolds number based on a local length scale. The most commonly used Reynolds number of this type is based on the momentum thickness and given by $R_\theta \equiv \theta \overline{U}/\nu$. One such relation of this form, given by von Kármán [59], is

$$R_\theta = \left(4.2 - 25.8\sqrt{\frac{c_f}{2}}\right) \exp\left[\kappa\left(\sqrt{\frac{2}{c_f}} - 7.9\right)\right]. \tag{4.6}$$

Other often used one-parameter relations are the empirical Squire-Young [63] equation

$$\lambda = \sqrt{\frac{2}{c_f}} = 2.55\ \ln(4.075 R_\theta), \tag{4.7}$$

and the $1/7^{th}$ power law relation [46]

$$c_f = 0.0256\, R_\theta^{-1/4}. \tag{4.8}$$

The latter equation is derived assuming a $1/7^{th}$ power mean velocity profile for most of the boundary layer. These one-parameter relations are strictly applicable to boundary layers with zero longitudinal pressure gradient, but are also found to have reasonably good accuracy when the streamwise pressure is slowly changing.

For improved accuracy in non-zero pressure gradients, a two-parameter relation is used; the second parameter most often being the momentum shape factor H. The best known two-parameter relation is that of Ludwieg and Tillmann [20]:

$$c_f = 0.256\, R_\theta^{-0.268}\, 10^{-0.678H}, \tag{4.9}$$

which was found to be very accurate for self-preserving boundary layers in most pressure gradients except those near separation. Other two-parameter relations were developed by Thompson [51], based on the intermittency of the boundary layer, and by Coles [10], based on an integration of his law of the wake. The

latter relation, however, is considered much less reliable than that of Ludwieg and Tillman.

The one-parameter von Kármán relation given above can be modified to take into account the longitudinal pressure gradient. By the addition of the logarithmic law of the wall and velocity defect law expressions, one obtains

$$\lambda = \frac{1}{\kappa} \ln \left(\frac{R_\theta}{C_1 - C_2 \lambda^{-1}} \right) + (A + B), \tag{4.10}$$

where $\lambda \equiv \sqrt{2/c_f}$ and $A + B \approx 7.9$. The quantities C_1 and C_2 are shape factors which are determined from the mean velocity profile as described in Appendix A. In a zero pressure gradient boundary layer these two shape factors are constants having the values approximately 4.2 and 25.8 respectively and this equation becomes identical to Eq. 4.6. In non-zero pressure gradients, these shape factors are determined from the mean velocity profile.

The foregoing methods are not applicable to rough surfaces; however, Perry et al. [35] developed a modified Clauser plot method to handle boundary layers on rough surfaces. As explained in Chapter 3, with the appropriate choice of origin for y, the mean velocity profile in the fully turbulent wall region is also logarithmic when the wall is rough. Thus, the essence of Perry's method is a graphical technique to determine the origin offset, ϵ, which will produce the best straight line on a semi-log plot of $\overline{u}/\overline{U}$ versus $(y+\epsilon)\overline{U}/\nu$. The slope of the straight line yields the skin friction; however, unlike the Clauser smooth wall method, the intercept can not be used as second means to obtain the skin friction, because the intercept is a function of the roughness.

One other graphical rough wall skin friction method based on velocity profile similarity involves a plot of $\overline{U} - \overline{u}$ versus $\ln(y/\delta)$. Provided the correct origin for y has been used, such a plot will fit a straight line in the log law region whose slope is $-u_\tau/\kappa$, which can be used to determine the friction velocity. The determination of the skin friction by this method is less precise than by Perry's graphical procedure because of the difficulty in obtaining an accurate value of the boundary layer thickness.

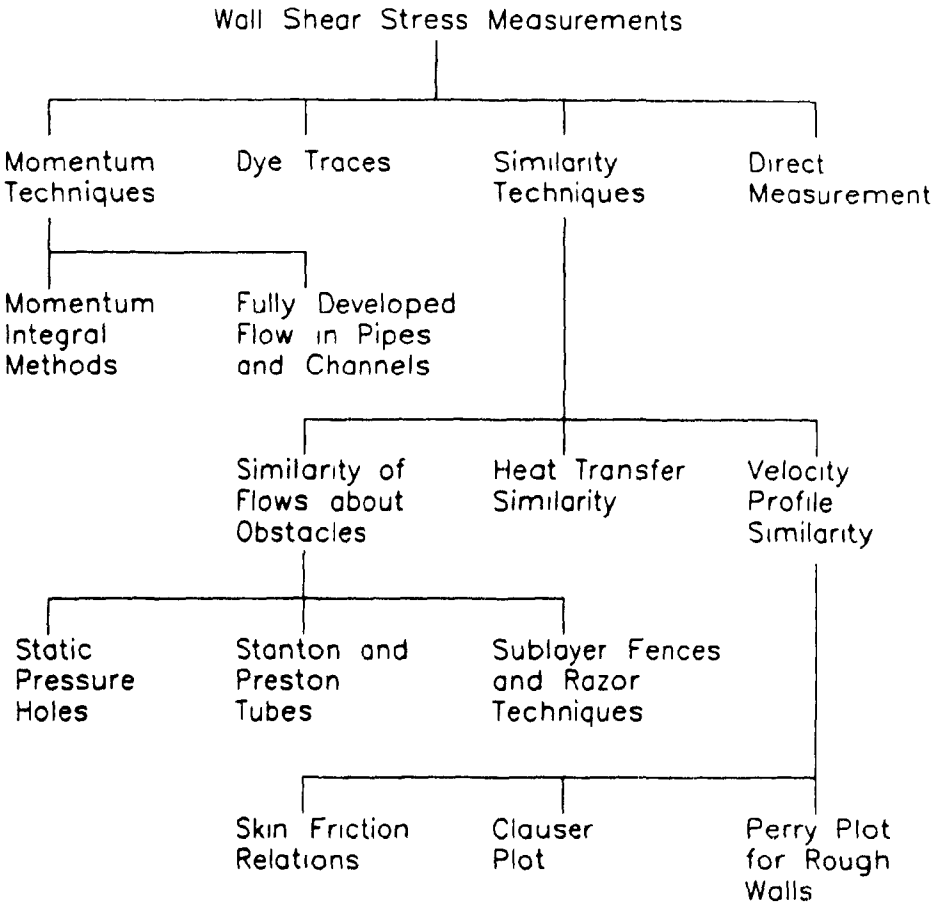

Figure 4.1: Techniques of Measuring Turbulent Skin Friction

Chapter 5

PROPOSED SKIN FRICTION INSTRUMENT

This chapter outlines the rationale and objective of this research, summarizes the solutions which were considered, and finally, introduces the proposed instrument and its principle of operation.

5.1 Rationale and Objective

A percentage of the total drag on streamline bodies, such as aircraft and ships, is due to skin friction. The roughness of the surface of the body is of great importance as it may cause the skin friction to increase significantly. At the high Reynolds numbers which occur on ships, the skin friction may be increased as much as forty percent by surface roughness [46]. Roughness due to weeds and barnacles adhering to the ship's hull has a particularly detrimental effect on surface resistance. Roughness is also important on airplanes whose surfaces are painted with camouflage paints, and on turbine and compressor blades. It is of great interest to know the extent to which the surface is contributing to the overall drag on the body, especially as the body ages and surface deterioration begins. For marine craft in particular, the carrier may decide at some point that it is economically beneficial to resurface the craft rather than incur the higher operating costs. To make this decision one requires knowledge of the surface conditions and the effect of the surface on the skin friction drag.

The purpose of this research is to design a simple device which will determine the local skin friction on a flat plate over varying surface roughness from smooth

to the fully rough régime. The device is to be designed for operation in zero or small pressure gradients, and should be rugged enough for use in marine applications.

Of the existing skin friction methods discussed in Chapter 4, only a similarity technique holds promise for a rugged device for measuring skin friction on a rough surface in a practical application. Momentum techniques are unreliable and require boundary layer velocity profiles, while direct measurement is delicate and best suited to laboratory conditions. Most existing similarity methods are not applicable to rough walls; the only exceptions being graphical procedures, such as that of Perry et al. However, since an analysis of velocity traverse data is required, a graphical method is not suitable means of determining the skin friction in the desired applications. It is preferable to have an instantaneous output from a fixed device requiring little computation, as is achieved, for example, using a Preston tube on a smooth wall.

5.2 Solution Approach

The objective of designing a simple device for the measurement of local skin friction led to dimensional considerations regarding an instrument requiring as few pressure measurements as possible. Thus, the approach to this problem consisted of theoretical investigations into the feasibility of a single pitot tube instrument, followed by a two tube instrument, and so on. The findings of these investigations are briefly presented in this section.

5.2.1 One Tube Instrument

The first approach was an adaptation of the Preston tube to suit the rough wall. For the Preston tube, the difference between the pitot and static pressures depend on the four variables ρ, μ, τ_w and d, which is precisely the number of variables required for one criterion of similarity, and hence, a simply calibrated formula relating this pressure difference to the wall shear stress. However, in attempting to apply the Preston tube to a rough wall boundary layer, at least two more independent variables arise in the dimensional analysis. The surface roughness itself must be characterized by at least one length scale, such as the equivalent sand roughness, k_s. A second length scale is required because the

statement that the Preston tube rests directly on the surface loses its meaning when the surface is rough. For the smooth wall, the Preston tube is in contact with a well defined surface, so that the only variable characterizing the geometry is the diameter of the tube itself. For a rough wall, however, the vertical position of the tube must now be included as a geometric variable. Hence, the difference between the pressure measured at a single pitot tube and the static pressure, will now be a function of three criteria of similarity, as follows:

$$\frac{\Delta p d^2}{\rho \nu^2} = \mathcal{F}\left[\frac{\tau_w d^2}{\rho \nu^2}, \frac{k_s}{d}, \frac{y}{d}\right]. \tag{5.1}$$

Since neither the roughness nor the vertical position of the instrument will be known in practice, a one tube instrument can not be used, in the manner of a Preston tube, to measure the skin friction on a rough wall.

5.2.2 Two Tube Instrument

The introduction of a second pitot tube in the wall region at a vertical distance s from the first introduces an extra length scale into the dimensional analysis. The pressure difference between the two tubes will now be a function of four criteria of similarity:

$$\frac{\Delta p d^2}{\rho \nu^2} = \mathcal{F}\left[\frac{\tau_w d^2}{\rho \nu^2}, \frac{k_s}{d}, \frac{y}{d}, \frac{s}{d}\right]. \tag{5.2}$$

However, since both the tube diameter and the vertical separation between the two tubes are known geometrical quantities, their ratio can be fixed, thereby removing one criterion of similarity. This is done in the same manner as fixing the ratio of the inner to outer diameters of a Preston tube. As with the one tube instrument, the pressure difference depends on three criteria of similarity which will be unknown in practice for a rough wall. Thus, a two tube instrument is insufficient to determine the wall shear stress by a simple calibration when neither the roughness nor the exact vertical position of the instrument is known.

However, if the two tube instrument is placed in the logarithmic region of the boundary layer, then use can be made of the fact that the gradient of the velocity is independent of both the viscosity and the roughness. This is expressed in the equation

$$\frac{y}{u_\tau}\frac{\partial \overline{u}}{\partial y} = \frac{1}{\kappa}, \tag{5.3}$$

which is true for both smooth and rough wall boundary layers, provided the appropriate origin is used in the rough wall case. Referring to Figure 5.1, the velocity gradient can be replaced by the gradient of the total pressure, which is then approximated by the total pressure difference between the two tubes to give

$$\frac{y_{12}}{u_\tau} \cdot \frac{\overline{P}_1 - \overline{P}_2}{\rho u_{12} s_{12}} = \frac{1}{\kappa}, \tag{5.4}$$

where u_{12} is the average of the velocities $\overline{u}_1$ and $\overline{u}_2$, and s_{12} is the tube separation. Solving for u_τ gives the expression

$$u_\tau = \frac{\kappa y_{12}}{\rho u_{12} s_{12}} (\overline{P}_1 - \overline{P}_2). \tag{5.5}$$

Now by incorporating a static tube the velocity u_{12} can be determined from the measured pressures. Nevertheless, on a surface of unknown roughness the value of y_{12} is undetermined, and therefore the two tube instrument falls short of providing the skin friction.

Further theoretical considerations into a two tube instrument is given in Appendix B for the interested reader; however, the conclusion is the same as that given here.

5.2.3 Three Tube Instrument

The problem besetting the two tube instrument described above is the unknown vertical position y_{12}. By introducing a third pitot tube in the logarithmic region, as shown in Figure 5.2, a second equation of the same form can be written in terms of the unknown vertical position y_{23}. Then by subtracting the two equations, these vertical positions can be eliminated. A final expression for the wall shear stress can be obtained based solely on the measured pressure differences.

A detailed derivation of the equations for the three tube instrument is given in Appendix C for the sake of completeness, while a brief summary of the theory is given in the following section on the principle of operation.

5.3 Three Tube Instrument Principle of Operation

The proposed instrument, shown in Figure 5.3, consists of three pitot tubes aligned vertically in the logarithmic region of the boundary layer, as well as a

single static tube. The three pitot tubes make two sets of total pressure difference measurements. A wall static hole can not be used for the static pressure since the local roughness will have a great influence on the flow near the hole.

A thorough development of the equations for this instrument is given in Appendix C, so only a brief summary will be given here. The fundamental principle underlying this research is the fact that the velocity gradient in the log law region is given by

$$\frac{y}{u_\tau}\frac{\partial \overline{u}}{\partial y} = \frac{1}{\kappa} \tag{5.6}$$

for both smooth and rough surfaces. The mean velocity gradient is replaced by the pressure gradient using

$$\rho\overline{u}\frac{\partial \overline{u}}{\partial y} = \frac{\partial \overline{P}}{\partial y}, \tag{5.7}$$

and this equation is applied to two sets of pressure difference measurements, as shown in Figure 5.2, to obtain

$$\frac{y_{12}}{u_\tau}\cdot\frac{\overline{P}_1 - \overline{P}_2}{\rho u_{12} s_{12}} = \frac{1}{\kappa}, \tag{5.8}$$

and

$$\frac{y_{23}}{u_\tau}\cdot\frac{\overline{P}_2 - \overline{P}_3}{\rho u_{23} s_{23}} = \frac{1}{\kappa}, \tag{5.9}$$

where

$$y_{ij} \equiv \frac{1}{2}(y_i + y_j), \tag{5.10}$$

$$u_{ij} \equiv \frac{1}{2}(\overline{u}_i + \overline{u}_j), \tag{5.11}$$

and

$$s_{ij} \equiv y_i - y_j. \tag{5.12}$$

The latter equation is subtracted from the former and the velocities are replaced by dynamic pressures, yielding

$$\frac{1}{u_\tau} = \frac{2}{s_{12}+s_{23}}\sqrt{\frac{2\rho}{\kappa^2}(\overline{P}_2 - \overline{p})}\left(\frac{s_{12}}{\Delta_{12}} - \frac{s_{23}}{\Delta_{23}} + \frac{1}{4}\frac{s_{12}+s_{23}}{\overline{P}_2 - \overline{p}}\right), \tag{5.13}$$

where the symbol Δ_{ij} is now used to indicate the time-averaged total pressure difference $\overline{P}_i - \overline{P}_j$. Defining the geometrical ratio $\varsigma = s_{23}/s_{12}$ gives

$$\frac{1}{u_\tau} = \frac{2}{1+\varsigma}\sqrt{\frac{2\rho}{\kappa^2}(\overline{P}_2 - \overline{p})}\left(\frac{1}{\Delta_{12}} - \frac{\varsigma}{\Delta_{23}} + \frac{1}{4}\frac{1+\varsigma}{\overline{P}_2 - \overline{p}}\right). \tag{5.14}$$

If the local free-stream velocity is known by other means, an expression for the skin friction coefficient is obtained as follows:

$$c_f = \frac{\kappa^2(1+\varsigma)^2}{8\overline{Q}\overline{q}_2}\left[\frac{1}{\Delta_{12}} - \frac{\varsigma}{\Delta_{23}} + \frac{1+\varsigma}{4\overline{q}_2}\right]^{-2}, \tag{5.15}$$

where $\overline{Q}$ and $\overline{q}_2$ are the free-stream dynamic pressure and the dynamic pressure $\overline{P}_2 - \overline{p}$, respectively. Thus, the skin friction can be obtained without reference to the roughness, the vertical position of the instrument, or the spacing between the three tubes. The only geometrically significant quantity is the ratio of the pitot tube separations, ς.

5.4 Three Tube Instrument Design Considerations

The most important design consideration for the three tube instrument is the separation between the tubes. On the one hand, the overall vertical size of the instrument is severely restricted due to the small size of the logarithmic region of a turbulent boundary layer. While on the other hand, the pressure differences Δ_{ij} are very small so that a large separation of the tubes would produce the best accuracy, but not so large as to make invalid the assumption that Δ_{ij} is small compared to $\overline{q}_2$.

The logarithmic region generally extends from $yu_\tau/\nu \approx 30$ to $y/\delta \approx 0.2$. In air, the physical lower limit is usually within one millimetre from the wall; however, in a marine application, it may be as large as one centimetre or more. The upper limit of $y/\delta = 0.2$ depends on other influences, such as the Reynolds number and the stream-wise pressure gradient; furthermore, since δ may vary considerably depending on the application, the physical upper limit on y is difficult to specify with certainty. In the present experiment, the limit is on the order of 10 millimetres; in possible marine application, it may be tens of centimetres. In the latter case, an instrument a few centimetres in size should be more than sufficient for accurate measurement of the pressure differences.

Another important design consideration is the size of the pitot tubes themselves. Ideally, they should be small relative to the tube separation to minimize flow interference and obtain a very localized pressure. However, if the tubes

are very small, problems may arise concerning viscous effects on the measured pressures or with the response time of the instrument.

Finally, consideration must be given to the length of the instrument, and the size and position of the static tube such that the interference effects cancel at the location of the static hole, and the true static pressure can be measured.

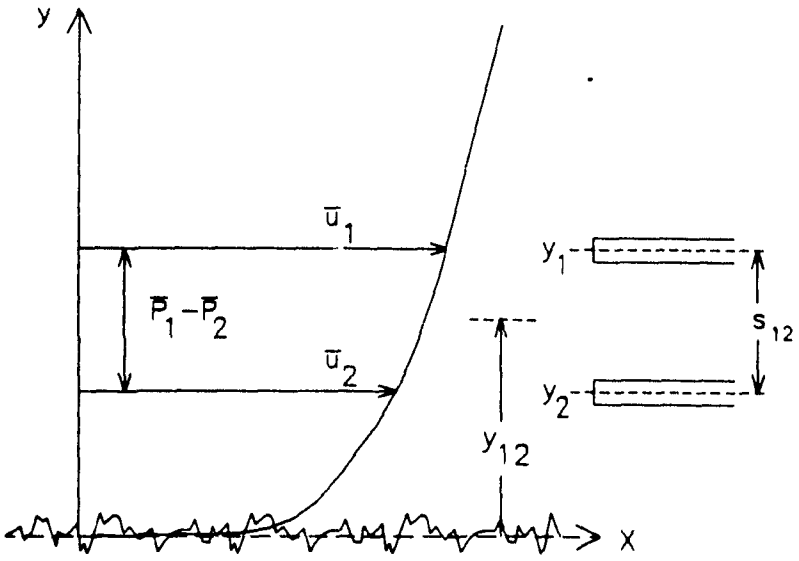

Figure 5.1: Variables Associated with a Two Tube Instrument

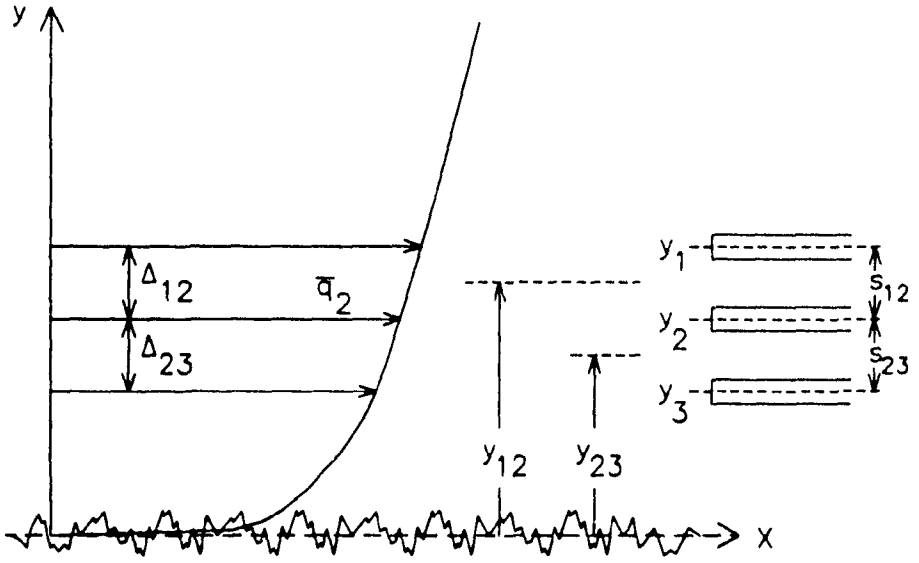

Figure 5.2: Variables Associated with the Three Tube Instrument

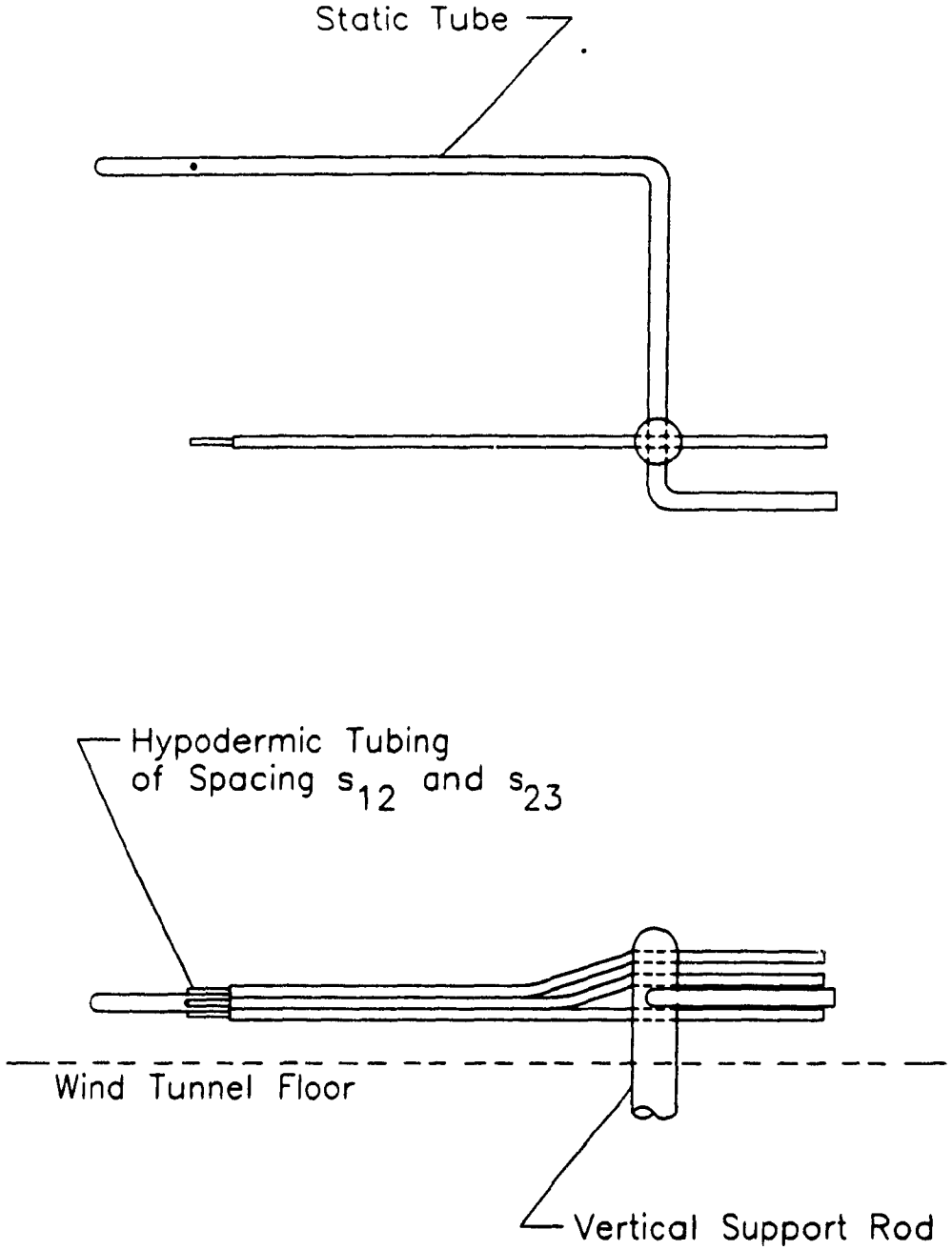

Figure 5.3: Diagram of the Proposed Three Tube Instrument

Chapter 6

EXPERIMENT

The aim of the experimental investigation is to test the three tube instrument introduced in Chapter 5 and shown in Figure 5.3. The instrument is investigated on a flat plate with both smooth and rough finishes, and the skin friction coefficient is calculated using Eq. 5.15. This chapter provides the experimental details of this research, including a description of the apparatus and the procedure undertaken in this experimental investigation.

6.1 Apparatus

6.1.1 Wind Tunnel

The wind tunnel, shown in Figure 6.1, is an open return type with a closed working section 914 mm wide by 610 mm high in cross-section, and approximately 2.04 m in length. The intake is two-dimensional with parallel vertical walls, and upper and lower walls converging at an angle of 90 degrees. The converging walls merge into the working section through a curved section whose shape is based on the free streamline solution for flow emerging from two converging plates. This prevents separation and establishes a rather uniform flow in the working section. The intake is fitted with a 14 mesh, 0.56 mm diameter curved gauze followed by a 6.4 mm by 25.4 mm deep curved honeycomb to straighten the flow and reduce turbulence.

Behind the working section is a rectangular diffuser followed by a transition section from rectangular to circular cross-section. At the end of this section is a five-bladed Buffalo Forge 54s Type B Vane axial fan driven by a 40 hp d.c. motor

to speeds up to 1150 rpm. A Ward-Leonard control system, consisting of a 550 V three phase a.c. motor driving a d.c. generator, supplies power to the d.c. fan motor. The fan speed is controlled by varying the current in the field windings of the generator. This system provides a smooth speed control in the working section from zero to nearly 50 m/s. The outlet of the fan is connected to a large filter box, for the purpose of reducing noise, filtering the air, and reducing the swirl in the returning air flow.

Floor of the Working Section

The boundary layer measurements in this study were performed on the floor of the working section. Two new floors were installed specifically for this research, both of which were 28.6 mm thick Douglas Fir plywood. The first floor was used in the preliminary tests and all succeeding smooth wall tests, and was prepared with an extremely smooth finish. The second floor was used exclusively with the sandpaper roughness, and was therefore left unfinished.

The smooth finish of the first floor was obtained as follows. The upper surface of the floor was initially painted and varnished to fill in tiny holes, prevent warping, and prolong the life of the wood. The floor static pressure taps were put in place as shown in Figure 6.3. These static pressure holes consisted of 2.4 mm O.D. brass tubing with a 1.6 mm hole, whose ends were machined flat and square, which were pressed into place and aligned vertically with the surface to an accuracy of less than 0.025 mm. The surface was then sanded smooth with successively finer sandpaper grades, to grain size #600. Afterwards, the surface was waxed and polished to produce an extremely smooth finish. Later in the experiment, two new static pressure taps were placed in the floor as well as a 20.4 cm diameter aluminum plate, also shown in Figure 6.3, for supporting the skin friction balance, Preston tubes, traversing apparatus and three tube instrument. The floor was re-sanded, waxed and polished in the areas near these changes. The aluminum plate was installed in the floor on the wind tunnel centerline at the $x = 1.60$ m station, and aligned with the surface to a tolerance of less than 0.05 mm in height, and 0.01 mm in gap size. The second set of static pressure taps were made of a cylindrical brass insert of 6.4 mm O.D., with a 0.5 mm hole. The upper surface was machined flat, while preserving the squareness of the hole edges. The two taps were placed 15.3 cm on either side of the wind

tunnel centerline at $x = 1.60$ m, and aligned vertically with the floor to 0.01 mm tolerance. The static pressure readings of the two floor taps were found to agree to less than 0.2 percent of the free-stream dynamic pressure over all wind tunnel speeds, and both agreed with a static tube to less than 0.4 percent. These small discrepancies may be as much due to natural lateral variations in the static pressure within the wind tunnel, as errors due to the manufacturing of the pressure taps themselves; therefore, it was concluded that no improvement could be made to obtain the static pressure with greater accuracy.

An identical aluminum plate was inserted into the second floor to support the balance, traversing apparatus, and three tube instrument for the rough wall measurements. No floor static pressure taps were used with this floor, however, since the presence of the roughness would make such measurements impossible. Instead, the static pressure was measured solely using the static tube of the three tube instrument, and was believed to be the true static pressure to within 1.0 percent of the free-stream dynamic pressure.

Free-Stream Turbulence

The r.m.s. turbulence in the free-stream of the working section is approximately 0.4 percent of the free-stream velocity and does not vary appreciably with tunnel Reynolds number [60].

Static Pressure Gradient

The boundary layer thickness on the smooth floor at the center of the test section was observed to be approximately 33 mm at velocities greater than 20 m/s. Due to the longitudinal growth of the boundary layers on all four walls of the working section, a small favourable pressure gradient exists in the longitudinal direction. In the initial calibration of the wind tunnel in 1961 [60], the pressure gradient was found to be

$$\frac{1}{\frac{1}{2}\rho\overline{U}^2}\frac{d\overline{p}}{dx} = -0.028\,\mathrm{m}^{-1}$$

at $x = 1.33$ m and approximately constant in the longitudinal direction. The static pressure was measured in the preliminary investigation using floor static pressure taps. The static pressure drop in the wind tunnel, non-dimensionalized with respect to the free-stream dynamic pressure, is shown in Figure 6.2. It is

evident that the effect of the diffuser, which starts at $x = 2.04$ m, is felt upstream by the reduction of the static pressure. In compromising between a small static pressure gradient and a large boundary layer thickness, the $x = 1.60$ m location was chosen as the station where the three tube instrument was investigated. The average pressure gradient at this location is found to be approximately

$$\frac{1}{\frac{1}{2}\rho\overline{U}^2}\frac{d\overline{p}}{dx} = -0.023\,\mathrm{m}^{-1}$$

for the smooth wall. The static pressure gradient was not measured with the sandpaper roughness, but was estimated theoretically from the measured change in the boundary layer displacement thickness, δ^*. At most, it was found to be

$$\frac{1}{\frac{1}{2}\rho\overline{U}^2}\frac{d\overline{p}}{dx} = -0.028\,\mathrm{m}^{-1}.$$

Two-Dimensionality of the Flow

The variation in the free-stream velocity across the working section but outside the wall boundary layers is about 0.15 percent [60]. Thus, the variation in the free-stream dynamic pressure is about 0.3 percent of the mean, which is smaller than the one percent uncertainty in the free-stream dynamic pressure measurements; therefore, the lack of two-dimensionality in the free-stream flow is well within the measurement uncertainty.

The two-dimensionality of the flow within the floor boundary layer was not investigated. However, the static pressure was measured on the smooth floor using static taps on both sides of the centerline as shown in Figure 6.3. Measurements of the static pressure using the type #1 taps were not very accurate due to the large size of the hole; nevertheless, agreement between taps on either side of floor was observed to about 0.5 percent of the free-stream dynamic pressure over the entire range of wind tunnel speed. For the more accurate type #2 static taps, agreement was found to less than 0.2 percent of free-stream velocity.

Total and static pressure contours for the working section of the wind tunnel are given by Wygnanski and Newman [60], and indicate that the pressure distributions are very uniform at the floor centerline within 2 cm from the wall and 5 cm on either side of the centerline. Since the three tube measurements are all confined to within 2 cm from the floor, the two-dimensionality was not a problem in the use of the three tube instrument.

Measurement of the Dynamic Pressure

The free-stream dynamic pressure was measured using a pitot-static probe hanging approximately 10 cm below the ceiling of the wind tunnel directly above the $x = 1.6$ m station. This distance from the ceiling was found to be sufficient to obtain free-stream measurements, since the boundary layer thickness at this location was of the order of 3 to 5 cm.

6.1.2 Roughness

In a preliminary investigation to study the boundary layer on a rough surface, the roughness was created by fastening a wire screen to the smooth floor of the wind tunnel. In the investigation of the three tube apparatus, the roughness was created using sandpaper glued to the unfinished floor.

Wire Screen

In the first part of the experiment a brass 8 mesh, 0.71 mm diameter wire screen was used and fastened to the smooth floor with staples. This screen was chosen with the specific diameter to mesh ratio of 0.221 to geometrically match the wire screen roughnesses used by Hama [17].

Sandpaper

To eliminate the problems of fastening and aligning the wire screen on the skin friction balance head, sandpaper roughness was chosen for the roughness investigation with the three tube instrument. The sandpaper was found to be easily applied to the skin friction balance and, because of the irregularity of the roughness, no special roughness alignment was needed between the floating head and its surroundings. A single sheet of sandpaper, open-coat garnet sand of grit size #40, was laid on the floor and fastened using double sided tape and contact cement. Cut-out holes were made to accommodate the skin friction balance and three tube apparatus support rod. The contact cement was used near these cut-outs to prevent the paper from peeling off during the running of the wind tunnel, while the tape was used in all other places for ease of removal of the sandpaper.

The sandpaper was examined through a microscope to determine the typical grain size. The grains were very irregular in shape and orientation but rather

uniform in size. This is expected since the process by which the grains are obtained filters out grains which are much larger or smaller. The typical grain dimensions varied from about 0.42 mm to 0.50 mm; the characteristic roughness dimension was taken to be the average, $k = 0.46$ mm.

The three tube instrument was also investigated on a second size of sandpaper, which was open-coat silicon carbide of grit size #24. The typical grain size was approximately $k = 0.81$ mm as measured under a microscope. This paper was fastened to the floor after the #40 sandpaper was carefully removed. Since the bond on this sandpaper had considerably more stiffness than that on the previous paper, it was glued to the floor using carpenters glue instead of the double sided tape.

6.1.3 Boundary Layer Rake

In the preliminary investigation, the boundary layer velocity profiles were taken using a fixed boundary layer rake, shown in Figure 6.4, instead of a traversing probe. The rake consisted of a total of 14 pitot tubes of 1.6 mm O.D. aligned vertically at different positions above the floor. The three pitot tubes closest to the wall were spaced about 1 mm apart and flattened for improved vertical accuracy; the lowest of the three rested directly in contact with the wall. Further from the wall were eleven circular stainless steel tubes whose spacing varied from about 2 mm near the bottom to roughly 7 mm at the top of the rake; the spacing was accurately measured using a Precision Tool and Instrument cathetometer. The circular ends were countersunk to reduce the sensitivity with respect to angle of attack, and the pitot tubes projected 38 mm in front of the streamlined vertical support to reduce blockage effects. Two stainless steel static tubes were located 38 mm on either side of the vertical array and at two different vertical positions, approximately 18 mm and 38 mm from the floor. The static tubes were oval-ended with small static holes in alignment with the stagnation tubes. The rake was held firmly to the floor by a horizontal rod, which was rigidly attached to a vertical pole between the floor and the ceiling about 30 cm downstream of the rake.

6.1.4 Three Tube Instrument

Description

The three tube instrument introduced in Chapter 5 is shown in its exact dimensions in Figure 6.5. The critical dimensions of the small hypodermic tubing are shown in an enlargement in Figure 6.6. The instrument consists of three stainless steel hypodermic pitot tubes of outer diameter 0.82 ± 0.01 mm, aligned vertically within the logarithmic region of the turbulent boundary layer. The vertical spacings between the tubes were made as large as possible for the best accuracy in measuring the pressure differences Δ_{12} and Δ_{23}; however, the spacing was limited by the small size of the logarithmic region of the boundary layer on the floor of the wind tunnel, which was typically 6 mm to 10 mm depending on the Reynolds number and surface roughness. To allow for some variation in the vertical position of the instrument, the overall vertical spacing of the three tubes was confined to less than 3.5 mm. The exact spacing was measured using a Nikon model V-16 profile projector, giving:

$$s_{12} = 1.572 \pm 0.010 \text{ mm}$$
$$s_{23} = 1.616 \pm 0.010 \text{ mm}$$

The hypodermic pitot tubes were flat-ended with an inner to outer diameter ratio of 0.5, and were epoxied into three circular brass tubes of external diameter 1.59 mm, soldered together to form one solid instrument. The hypodermic tubes project a distance of 6.1 mm upstream of the brass tubing. The entire apparatus is mounted into a 6.4 mm O.D. steel rod which projects through the floor of the wind tunnel and allows for the vertical positioning of the three tube instrument. The vertical post also provided support for a 2.4 mm diameter brass static tube, which was positioned 38 mm to one side of the three tube apparatus. The front end of the static tube was an ovoid shape, while its length, diameter and the position of the static holes were determined from blockage effects using potential-flow theory. Tygon tubing was connected to the downstream ends of the tubes to carry the pressures to the pressure transducers, described later.

Construction

The construction of the three tube instrument was performed as follows. The three brass tubes were first machined round and smooth to diameters of 1.59 mm. They were then soldered together side to side and the solder was machined and sanded smooth. The three end holes were spaced 1.6 mm apart and drilled to a diameter of approximately 0.8 mm. This instrument was then tested in the wind tunnel in a uniform flow and it was discovered that the pressure at the outer two holes was considerably less than that at the central hole, indicating that the flow was stagnating at only one central point on the body. This speculation was confirmed in smoke tunnel tests on an 8:1 scale model which clearly showed only one stagnation streamline. The small stainless steel hypodermic tubes were manufactured to overcome this problem. Smoke tunnel tests were performed on the 8:1 scale model to determine the length of hypodermic tubing required to ensure flow stagnation on each of the three tubes, and to minimize displacement effects due to the curvature of the stagnation streamlines. The results of these tests indicated that about 6 mm of hypodermic tubing (on the real instrument) was sufficient to produce equal pressures for all three tubes with the apparatus placed in a uniform flow. Hence, the small hypodermic tubes were made and epoxied into the holes in the brass tubes. The ends of the hypodermic tubes were honed flat and drilled to produce a diameter ratio of 0.5.

The apparatus was examined for accuracy under a microscope, and all measurements were made using a Nikon model V-16 profile projector.

6.1.5 Preston Tubes

As a double check on the smooth wall skin friction coefficient, three different size Preston tubes were used. All three tubes were made of brass, were 64 mm in length and had the conventional internal to external diameter ratio of 0.6. The external diameters were 1.57 mm, 2.39 mm, and 3.18 mm respectively. The tubes were mounted through the opening in the floor used by the three tube apparatus, as shown in Figure 6.7.

The Preston tubes were constructed as follows. Brass tubing of the nominal outer diameter was chosen and a brass insert was soldering into one end. The end was then machined circular and flat, and the diameter accurately measured.

The internal hole was then machined to the correct diameter to give an internal to external diameter ratio of 0.6. Finally, the flat end was honed smooth using size #600 emery paper. The tubes were examined in a microscope to ensure their geometrical integrity.

While using the Preston tubes, the static pressure was obtained as an average of the pressures at the two floor static pressure taps on either side of the aluminum floor plate.

6.1.6 Traversing Apparatus

Detailed velocity traverses were performed on both the smooth and rough wall boundary layers at a few velocities to verify the existence of the logarithmic mean velocity profile and to obtain very accurate values of the momentum thickness, θ. The traversing equipment, shown in Figure 6.8, consisted of a single 1.27 mm diameter stainless steel pitot tube, directed into the flow from a vertical support passing through the wind tunnel floor. The circular end of the pitot tube was countersunk for reduced directional sensitivity. The vertical motion of the tube was controlled below the floor using a modified Mitutoyo digital vernier caliper, whose positional accuracy was ± 0.01 mm.

As with the Preston tube measurements, the static pressure was measured for the smooth wall traverses at the floor static pressure taps. For the rough wall traverses, the static pressure was measured by the pitot-static tube combination mounted below the ceiling which was used for the free-stream velocity measurements.

6.1.7 Pressure Transducers and Other Instrumentation

Five different pressure transducers were used in these experiments. For the boundary layer rake pressures and for the floor static pressure taps, multitube manometers were used, which allowed the pressure distributions to be visualized as well as measured. The manometers were methanol-filled and left open to atmospheric pressure at one end. For best accuracy, the manometers were used at angles of 10 to 20 degrees to the horizontal.

The free-stream dynamic pressure was measured using a methanol-filled, Model 655 Lambrecht manometer whose ends were attached directly to the stag-

nation and static tubes, thus avoiding the errors due to using the atmosphere as a reference pressure. The Lambrecht manometer had a sensitivity of about ±4.0 Pa on the 1:2 scale used for these measurements.

The pressure measurements associated with the three tube apparatus, Preston tubes, and velocity traverses were first made using Lambrecht manometers, but it was found that improved accuracy could be achieved using a Type 590 Barocel capacitive pressure sensor from Datametrics Inc. This transducer contains a flexible diaphragm within a capacitive cell. A pressure difference applied across the diaphragm causes it to flex, thereby changing the capacitance of the cell. The cell capacitance is accurately determined in an a.c. capacitance bridge and the output, a d.c. voltage from -10 V to +10 V, was calibrated with respect to the applied pressure difference. The calibration curve, shown in Figure 6.9, was found to be extremely linear over the entire range of the instrument; the calibration was found to be 241.645 Pa/V (±0.1 %) and independent of zero offset of the Barocel up to ±100 mV. The linearity is especially good in the pressure range from 0 to 20 mm of water where most of the measurements were taken. The 590 Barocel transducer had a full scale output of approximately 2.5 kPa and a stated accuracy of ±0.025 Pa; however, the accuracy of the pressure measurements was taken to be ±0.5 Pa due to errors associated with the time response of the tubing and zero drift of the Barocel. To remove the fluctuations in the output signal due to the turbulence, the signal was filtered through a low pass filter with an adjustable cut-off frequency. The cut-off frequency typically used was on the order of 1 Hz. Small fluctuations at lower frequencies were observed and averaged by eye to an accuracy of about ±1 Pa at best.

The Lambrecht manometers and the Barocel were both calibrated using the most sensitive pressure transducer available in the laboratory, an Askania water manometer accurate to ±10μm of water, or about ±0.1 Pa.

Finally, a Betz water manometer from T.E.M. Engineering was used as a guide for setting the wind tunnel speed, but was not relied upon for the velocity measurements at the test station since this manometer was calibrated for the free-stream velocity at the $x = 1.33$ m position.

The pressure transducers were connected to the apparatus using 1.6 mm and 2.4 mm I.D. clear tygon tubing as shown schematically in Figure 6.10. For rapidly changing the connections to the Barocel, a channel selector was built,

consisting of rubber tubing and pinchcocks, a combination giving a good seal and low volume displacement when closed.

For the density and viscosity of air, as well as the density of methanol, the ambient pressure and temperature were measured using a mercury barometer and thermometer.

6.1.8 Skin Friction Balance

For the purpose of measuring the wall shear stress in the rough wall boundary layers, a Selem Industries SM-251 skin friction balance, shown in Figure 6.11, was used. The balance was designed by Dr. John Dickinson of l'Université Laval, Québec City, Québec.

The balance directly measures the skin friction on a small element flush with the surface [14]. The principle of operation of the balance is as follows. A circular head of 32 mm nominal diameter is mounted flush with the surface of the balance on four 0.025 mm thick flexures such that the head is restrained to move in one direction only, parallel with the flow direction. The resistance to motion is essentially zero in this free direction, while the rigidity of the system is large in the orthogonal directions. The exact position of the head is detected by a change in the inductance of a linear voltage differential transducer (LVDT). An a.c. inductance bridge detects this change in inductance, and the output is channelled through a feedback loop to a motor which applies a sufficient force on the head to hold it stationary. Hence, the balance is operated in a null mode using closed-loop feedback. The output of the balance is a voltage proportional to the motor current required to hold the head in place, and the gain was specifically set to give 1 ± 0.005 mV per milligram of force on the head. In this null mode of operation, the balance measures the total force acting on the head in the direction of the unrestrained motion. Hence, the balance not only detects the surface drag, but also inclination, acceleration, pressure gradient forces, and possibly form drag when not properly aligned with the surrounding surface.

The electronics for the skin friction balance were equipped with a low pass filter for the removal of extraneous vibrational accelerations. Small scale turbulent motion is essentially averaged out over the surface of the balance head and therefore does not contribute much to the fluctuations in the balance output. Slower fluctuations, on the order of 1 Hz and less, were found to occur, but were

averaged by many readings. The effects of inclination and pressure gradient on the balance are treated in Appendix D.

Interchangeable Balance Heads

The balance was designed for this experiment to be used with interchangeable heads to examine different surface roughnesses. All heads were plexiglass and manufactured identically to the specifications shown in Figure 6.11. For the smooth surface measurements the head was centered in the opening of the balance and aligned vertically with the surrounding surface to a tolerance of about 0.013 mm. This strict limit, applied to eliminate form drag or separation on the head, was obtained by adjusting the head vertically until the output of the balance was seen to plateau, ensuring that neither stagnation nor backflow occurs on the head.

For the rough surface measurements a piece of the sandpaper was glued to the upper surface of the balance head using contact cement, and cut to the approximate diameter of the head with a razor blade. The head was then turned on a lathe to remove 0.10 mm from the diameter, thus ensuring that the sandpaper conform to the circular head to an accuracy of about 0.05 mm on the diameter. Since the sandpaper was irregular in roughness, it was not necessary to align the roughness on the head with that on the surrounding floor. With roughness elements on the head and surroundings, the sensitivity of the balance output to the vertical position of the head is reduced, and the head could be aligned vertically under a microscope to an accuracy of 0.025 mm.

The gap between the circular head and the surrounding upper surface of the balance was 0.076 mm in the smooth case and 0.130 mm for each of the two sandpaper roughnesses. This small gap size was needed to avoid gap flows which could alter the performance of the balance.

6.2 Procedure

The experimental procedure is divided into two parts: a preliminary investigation to obtain the boundary layer profiles, estimate the suitability of the measuring devices, and determine a suitable roughness size; and a thorough investigation of the three tube instrument. An uncertainty analysis was performed to determine,

for each measured quantity, the total measurement error and its effect on the uncertainties in the calculated results.

6.2.1 Boundary Layer Preliminary Investigation

The preliminary investigation consisted of approximately one hundred velocity profiles taken with the boundary layer rake of Figure 6.4. Twenty-nine of these profiles were obtained on the smooth floor of the wind tunnel, at four different x-wise stations, and several free-stream velocities. The stations were located between 0.61 m and 1.78 m from the leading edge of the test section floor. Since there was no well-defined beginning to the turbulent boundary layer, the leading edge was taken as a suitable reference position. However, this was a matter of convenience, as θ rather than x was, by necessity, the important boundary layer length scale of the analysis. The free-stream velocities ranged from about 10 m/s to 45 m/s. Some sixty velocity profiles were taken, at similar x-wise positions and free-stream velocities, for the boundary layer development on the wire screen of roughness scale $k = 1.4$ mm.

A very detailed error analysis was performed to determine the major sources of error, and to investigate ways of reducing the uncertainty. Furthermore, many of the velocity profiles were duplicated to check for repeatability. Both the smooth and rough wall rake profiles were analyzed to determine the skin friction coefficient using several of the techniques described in Chapter 4.

6.2.2 Investigation of the Three Tube Instrument

In the second part of the experiment, the three tube instrument was investigated at the fixed station 1.6 m from the beginning of the working section.

In theory, the three tube instrument should work in any pressure gradient, except in the extreme case where the pressure gradient causes the breakdown of the logarithmic velocity distribution. All experiments were performed in a mildly favourable pressure gradient, which exists due to the growth of the wall boundary layers. The longitudinal static pressure, shown in Figure 6.2, was measured using the multitube manometer. In terms of the pressure gradient parameter $\Delta \equiv (\nu/\rho u_\tau^3)(dp/dx)$, the pressure gradient at the station was found to vary from $\Delta = -0.0001$ to $\Delta = -0.0005$ over the range of u_τ obtained from

the preliminary investigation above. According to Patel [30] the log law is unaffected by a pressure gradient provided $-0.002 \leq \Delta \leq 0.00575$; hence, it was determined that the pressure gradient in the present experiment has no effect on the logarithmic distribution of the mean velocity. Furthermore, no attempt was made to systematically control the pressure gradient to determine the limits of application of the instrument in very strong favourable or adverse pressure gradients.

The three tube instrument was tested in boundary layers produced on both smooth and rough walls. The measured values of s_{12} and s_{23} were corrected in each experimental run to account for displacement of the stagnation streamlines due to the effect of a shear velocity profile on a pitot tube. The corrections were made to the value of ς for use in Eq. 5.15. Displacement effects due the to the proximity of the wall and interference of the neighbouring two pitot tubes were considered but found unimportant. These corrections, as well as corrections to the pressure measurements, are described in detail in Appendix E.

Smooth Wall Tests

Experiments were first performed on the smooth wall. Since the x position was fixed, the Reynolds number was varied by changing the wind tunnel speed from approximately 20 m/s to 45 m/s. At each speed, the four quantities, $\overline{Q}$, $\overline{q}_2$, Δ_{12}, and Δ_{23} were measured. Corrections for viscous effects were made as described in Appendix E; the effects of turbulence and wall proximity on the pressure measurements were also considered, but because these corrections are difficult to apply, they were incorporated instead into the uncertainty of the readings. The vertical position of the three tube apparatus was varied by a small amount to test the instrument for independence with respect to the vertical position, as expected from the theory. However, since the instrument was designed to occupy most of the logarithmic region, the total vertical variation was only about 2 mm. The results were compared with the skin friction determined from the rake profiles of the preliminary investigation, and, as a double check, it was decided to compare the results with both Preston tube measurements, and the Clauser plot. Three different size Preston tubes were built and tested at the same location over the same range of Reynolds number. Detailed velocity traverses were also performed at two different Reynolds numbers using the traversing apparatus shown in Figure

6.8. The skin friction coefficient was determined from the traverses by the Clauser plot [7]; and a plot of u^+ versus $\ln y^+$ verified the logarithmic region of the boundary layer.

Sandpaper Roughness Tests

The roughness tests were performed in much the same manner as the smooth wall tests, except that the SM-251 skin friction balance was used to compare the skin friction coefficients. The balance was first tested on the smooth wall where the skin friction was already known. The second floor was obtained for the roughness investigation, and as before, the experiments were performed at the $x = 1.60$ m station. The two different size sandpaper roughnesses were investigated consecutively beginning with the size #40, followed by the more rough size #24. The procedure was exactly the same for each roughness investigation. The sandpaper was mounted on the floor of the wind tunnel and the head of the skin friction balance. The skin friction was determined directly from the skin friction balance over the entire range of wind tunnel speeds. Detailed velocity traverses of the boundary layer, consisting of typically 60 to 80 data points, were then taken at a few free-stream velocities to determine the momentum thickness θ, used in the determination of the Reynolds number, R_θ. The traverses were also analyzed using Perry's method, from which both the skin friction and the equivalent sand roughness, k_s, were determined. Finally, the three tube instrument was tested on the rough surface in the same manner as described for the smooth wall tests, and the results were compared to those obtained with the skin friction balance.

The non-dimensional roughness $k_s^+ = k_s u_\tau / \nu$ was also calculated from the skin friction balance measurements to determine the roughness régime: effectively smooth, intermediate, or fully rough.

Measurement of Vertical Position

Measurement of the vertical position from the floor of the wind tunnel was performed for both the three tube instrument and the detailed velocity traverses. The vertical position of the three tube instrument was defined as the distance from the center of the middle pitot tube to the top of the roughness or the flat surface of the floor for the smooth wall investigation. These measurements were

performed with a steel rule graduated in 0.5 mm divisions. The accuracy was at best about ± 0.5 mm, particularly on the rough surfaces where the "top" of the roughness was difficult to determine accurately. This accuracy is sufficient to know the approximate height of the instrument and to verify the applicability of the instrument at different vertical positions within the logarithmic region. However, some of the following results give y^+ values for the three tube instrument as a function of Reynolds number. For these plots, a great deal of confidence should not be placed in the values of y^+, especially for the measurements on the rough walls. Nevertheless, these results have been included because they are useful to obtain approximate values of y^+ for the instrument.

The vertical positions given in the detailed velocity traverses were measured very accurately using the traversing apparatus. The scale was graduated in 0.01 mm divisions, and the origin was accurately determined as follows. While taking the velocity measurements, the pitot tube was lowered until it touched the wall and then the stem of the tube was lowered further. Under the internal stress in the pitot tube, the front end would bend upwards into a region of higher velocity as the stem was being lowered. Thus, the traverse would indicate a minimum in the velocity profile which occurred when the tube was resting exactly on the surface. This was then taken to be the vertical position $y = 0.64$ mm, corresponding to the radius of the pitot tube. On the rough surfaces, the vertical positions were further corrected to take into account the origin offset due to the roughness. This correction was found by Perry's method as described above.

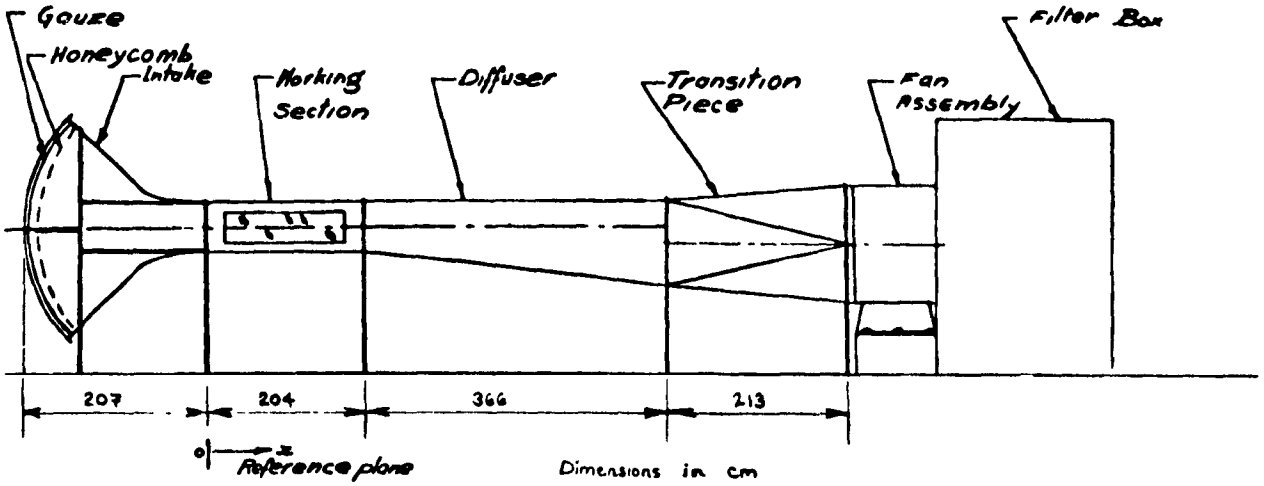

Figure 6.1: Diagram of the Wind Tunnel

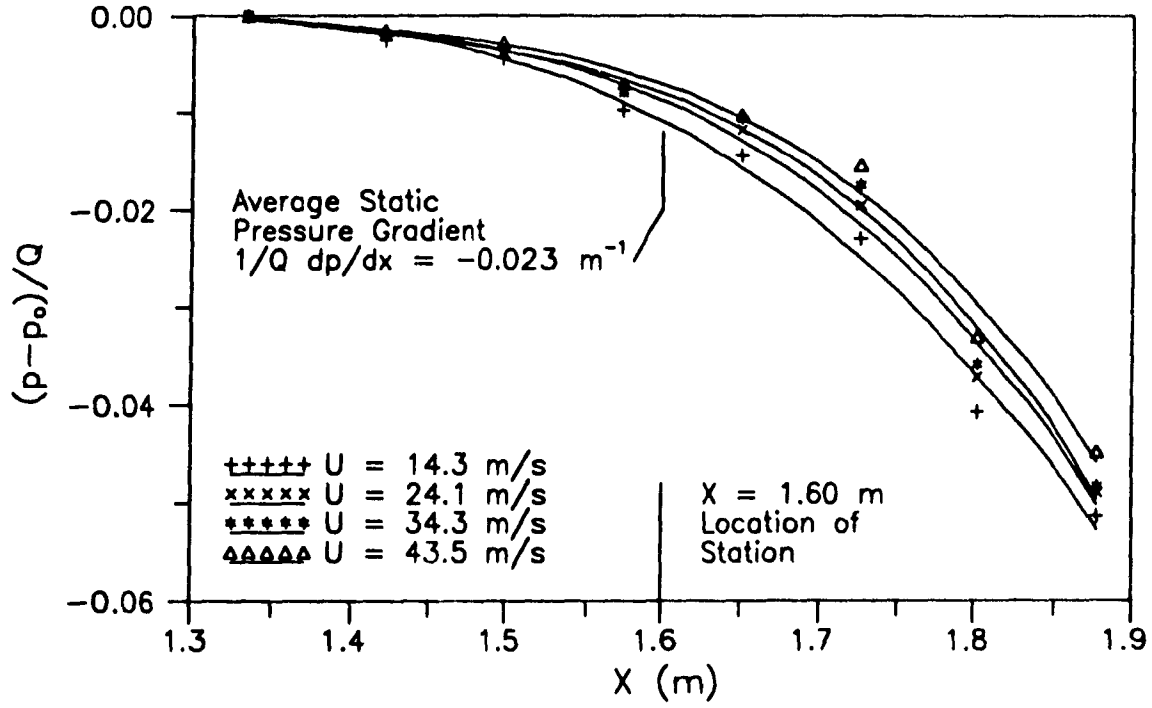

Figure 6.2: Wind Tunnel Static Pressure Near the Rear of the Test Section

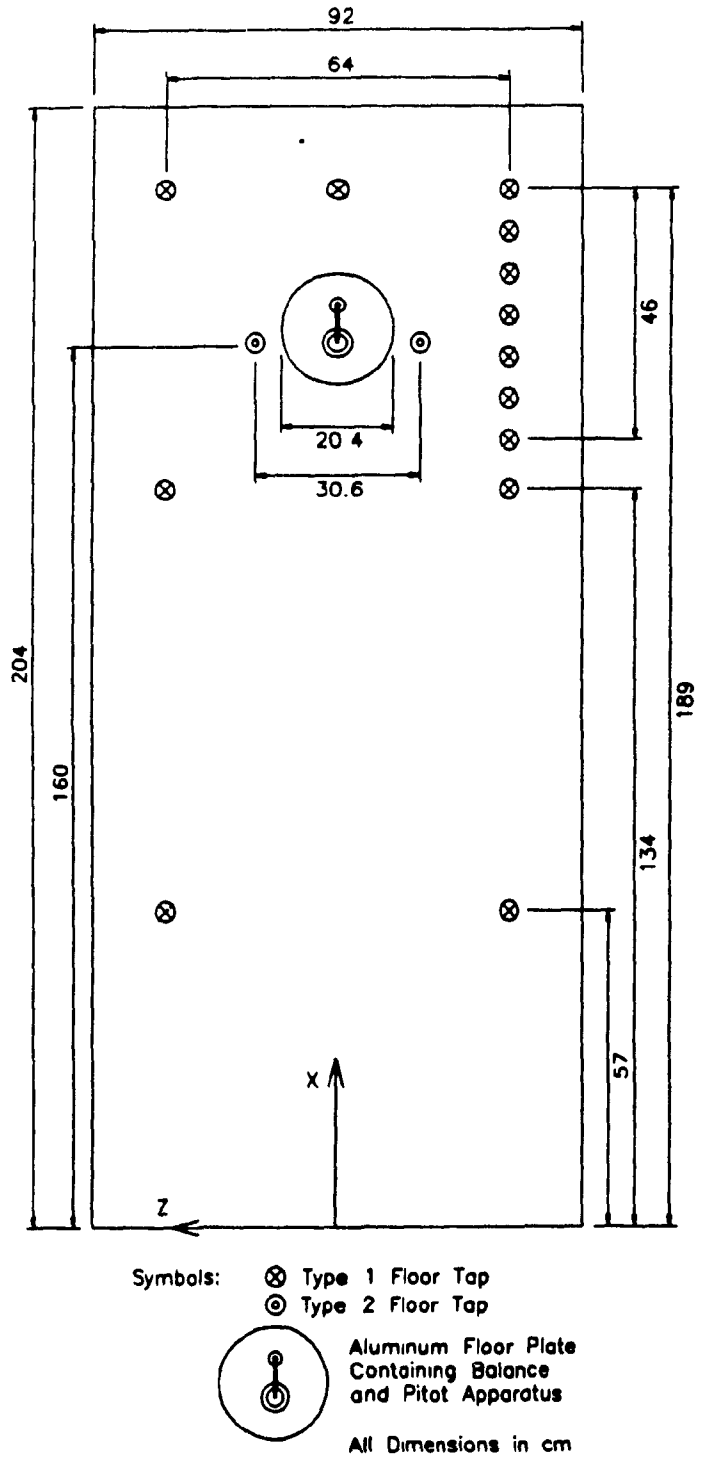

Figure 6.3: General Layout of the Wind Tunnel Floor

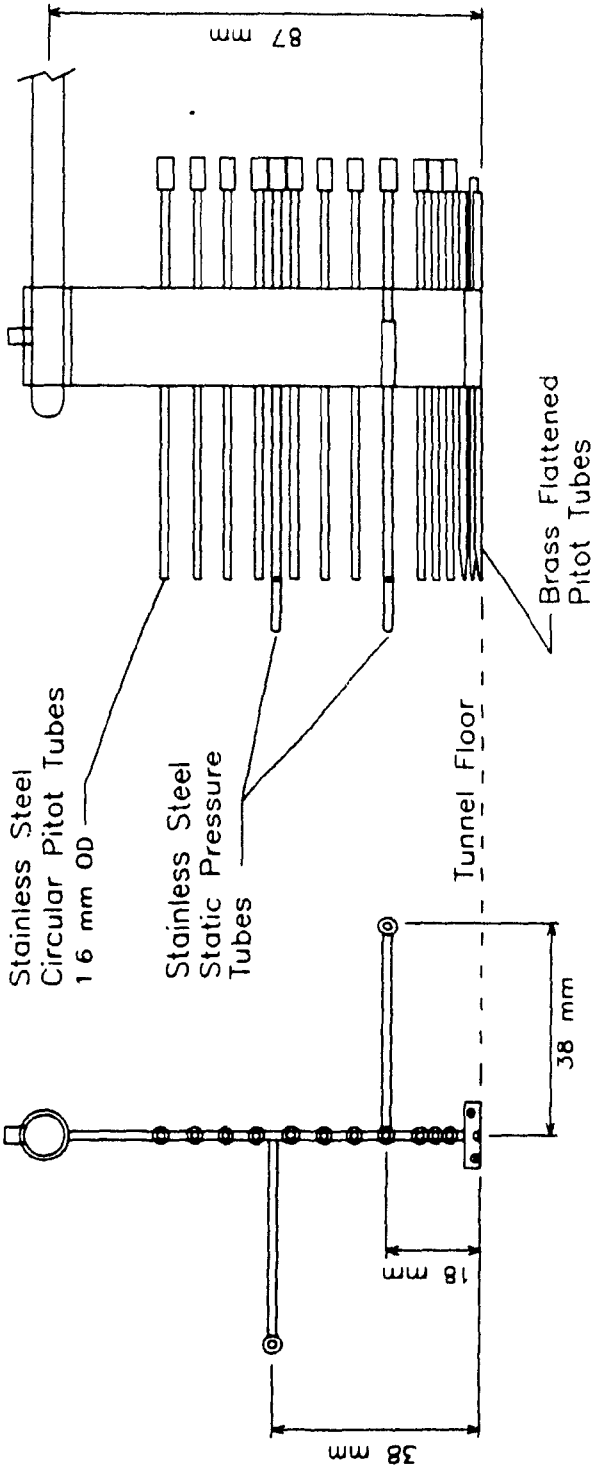

Figure 6.4: Boundary Layer Rake

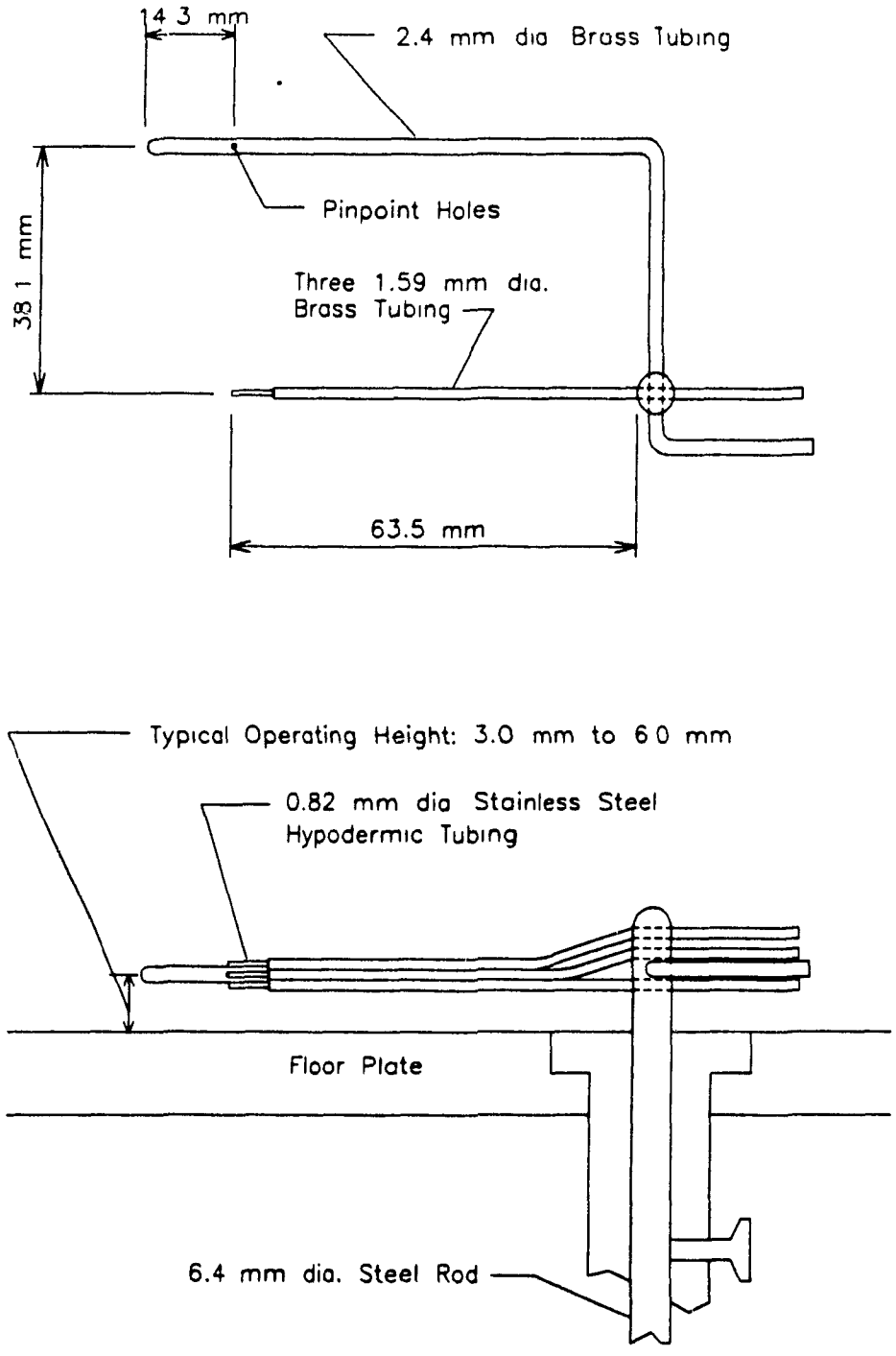

Figure 6.5: Three Tube Instrument Exact Specifications

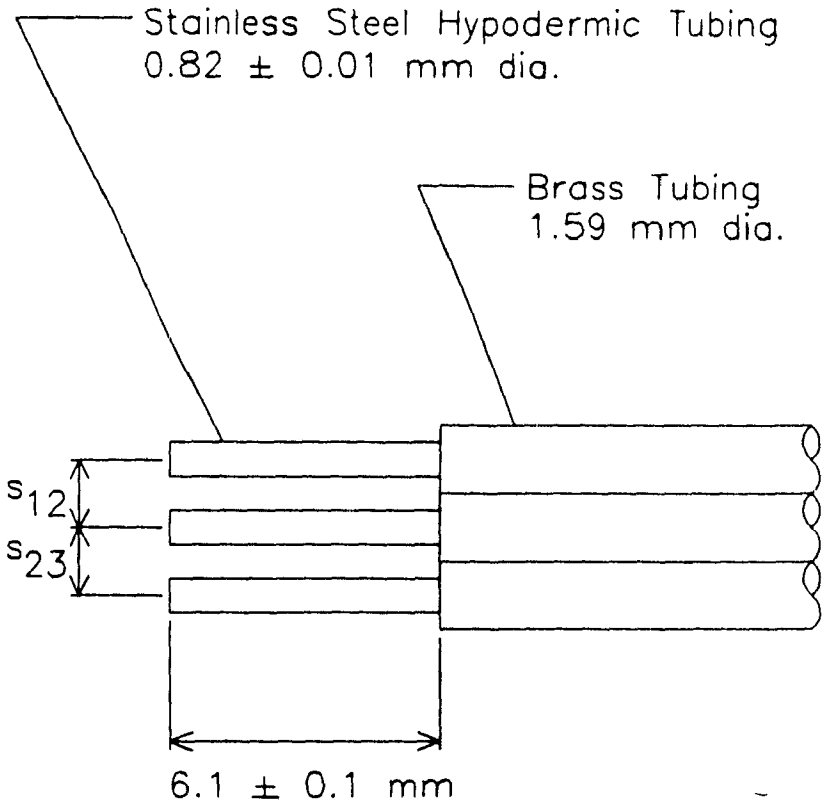

$s_{12} = 1.57 \pm 0.01$ mm

$s_{23} = 1.62 \pm 0.01$ mm

Figure 6.6: Three Tube Instrument Critical Dimensions

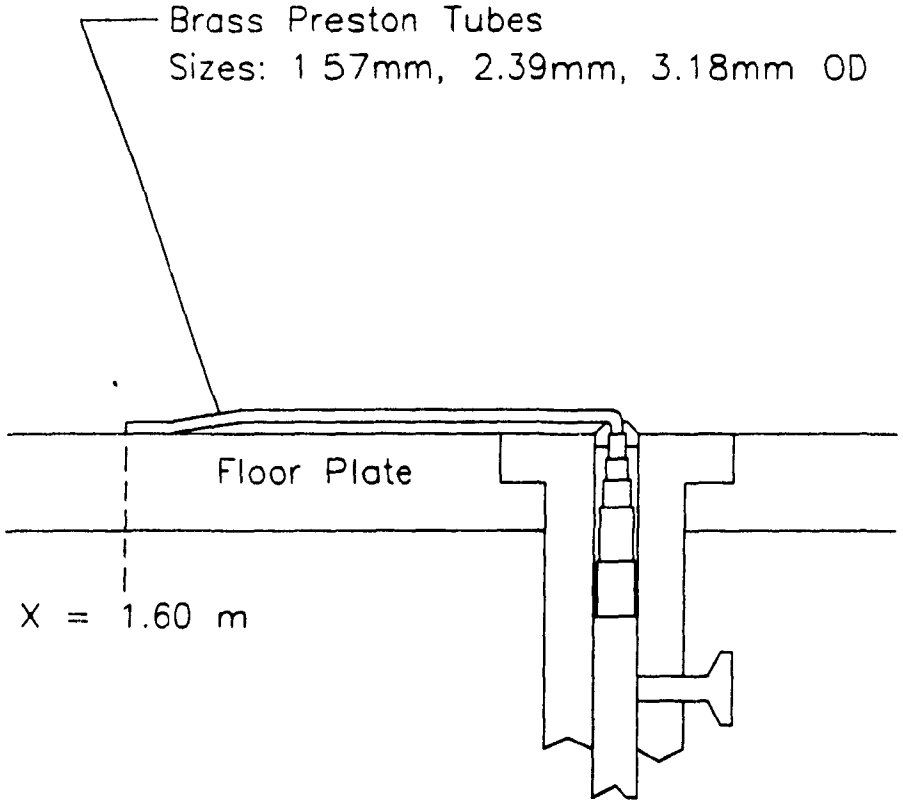

Figure 6.7: Preston Tubes

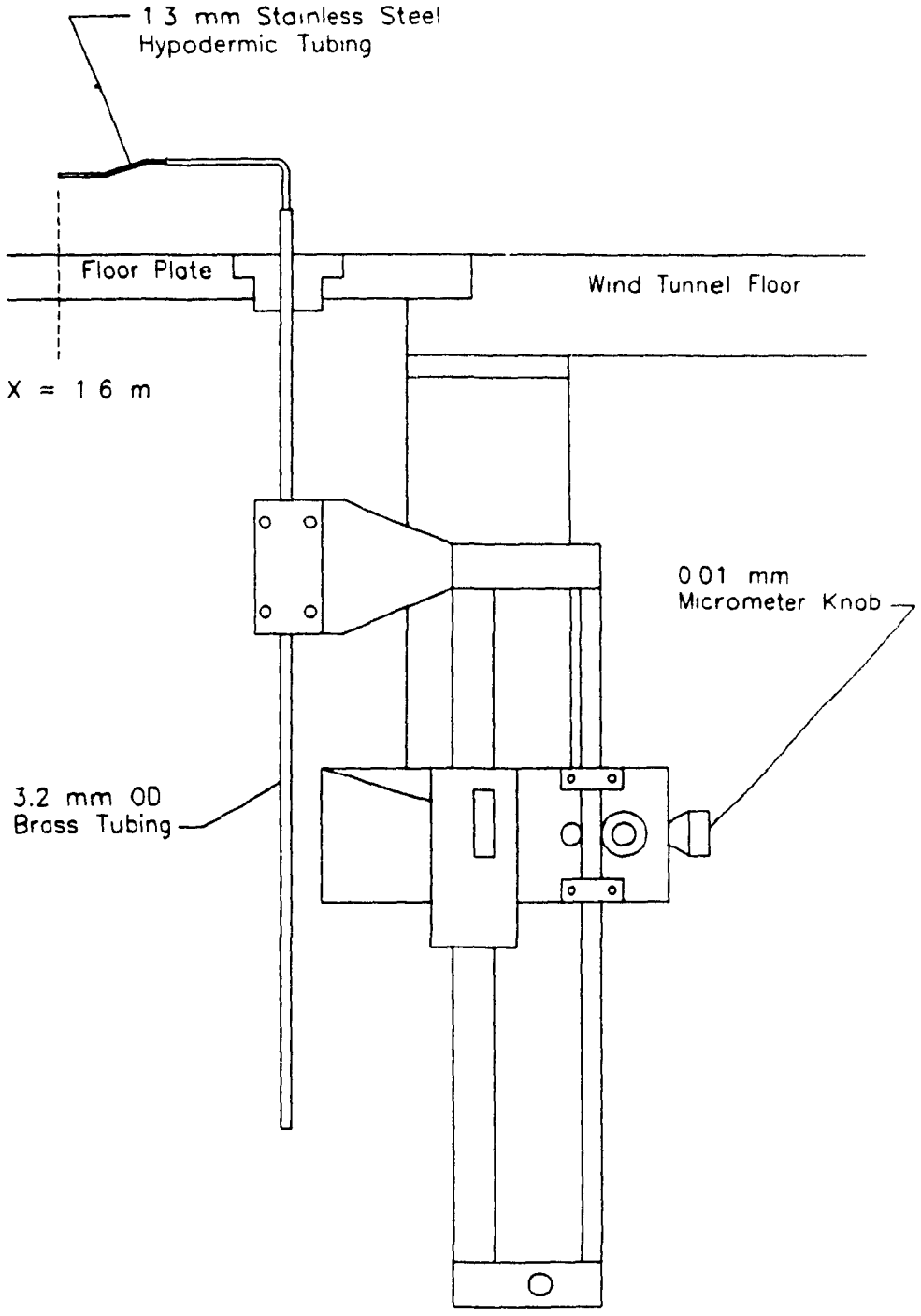

Figure 6.8: Boundary Layer Velocity Traverse Apparatus

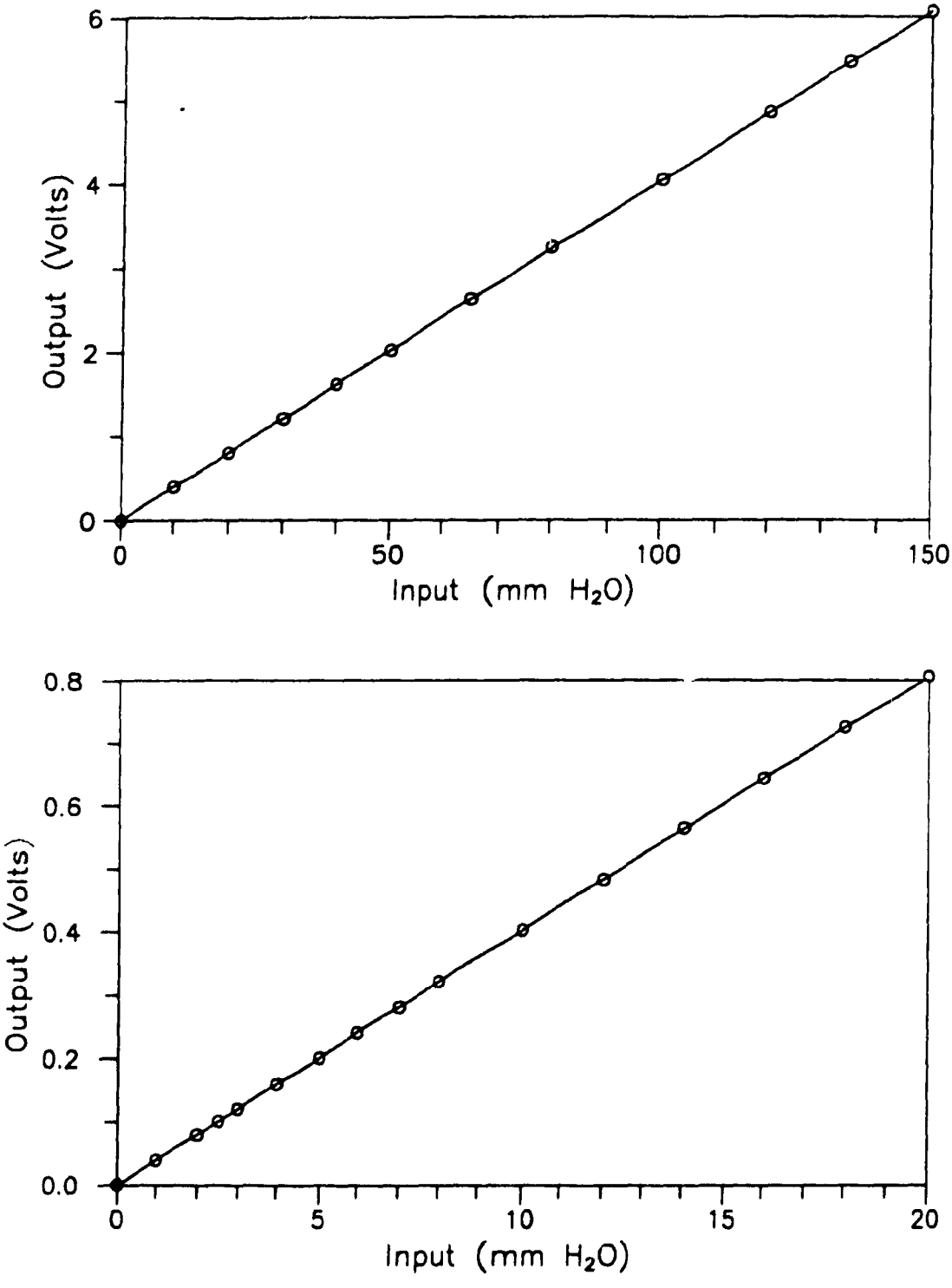

Figure 6.9: Barocel Calibration Curve

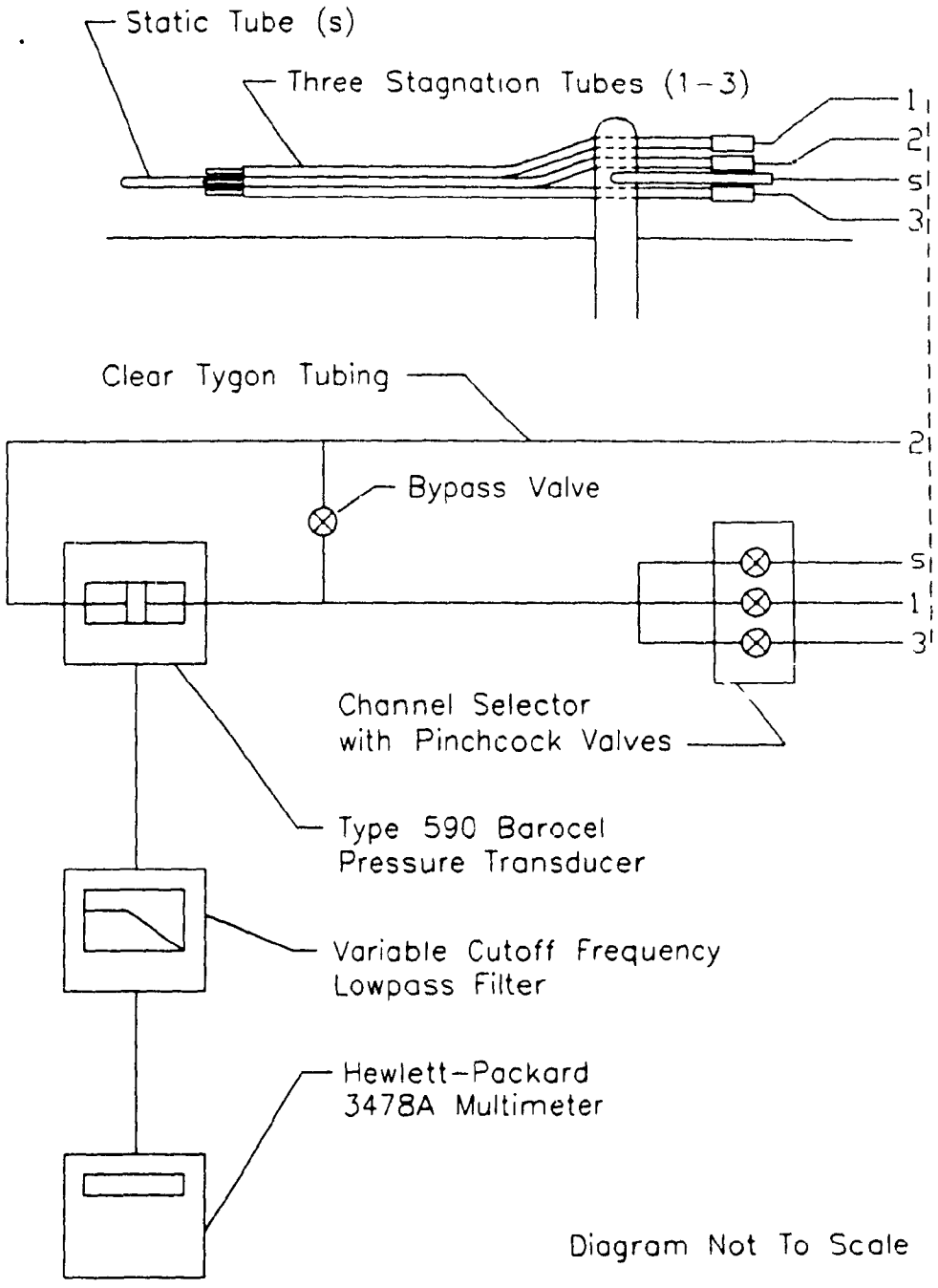

Figure 6.10: Schematic Diagram of the Instrumentation for the Three Tube Measurements

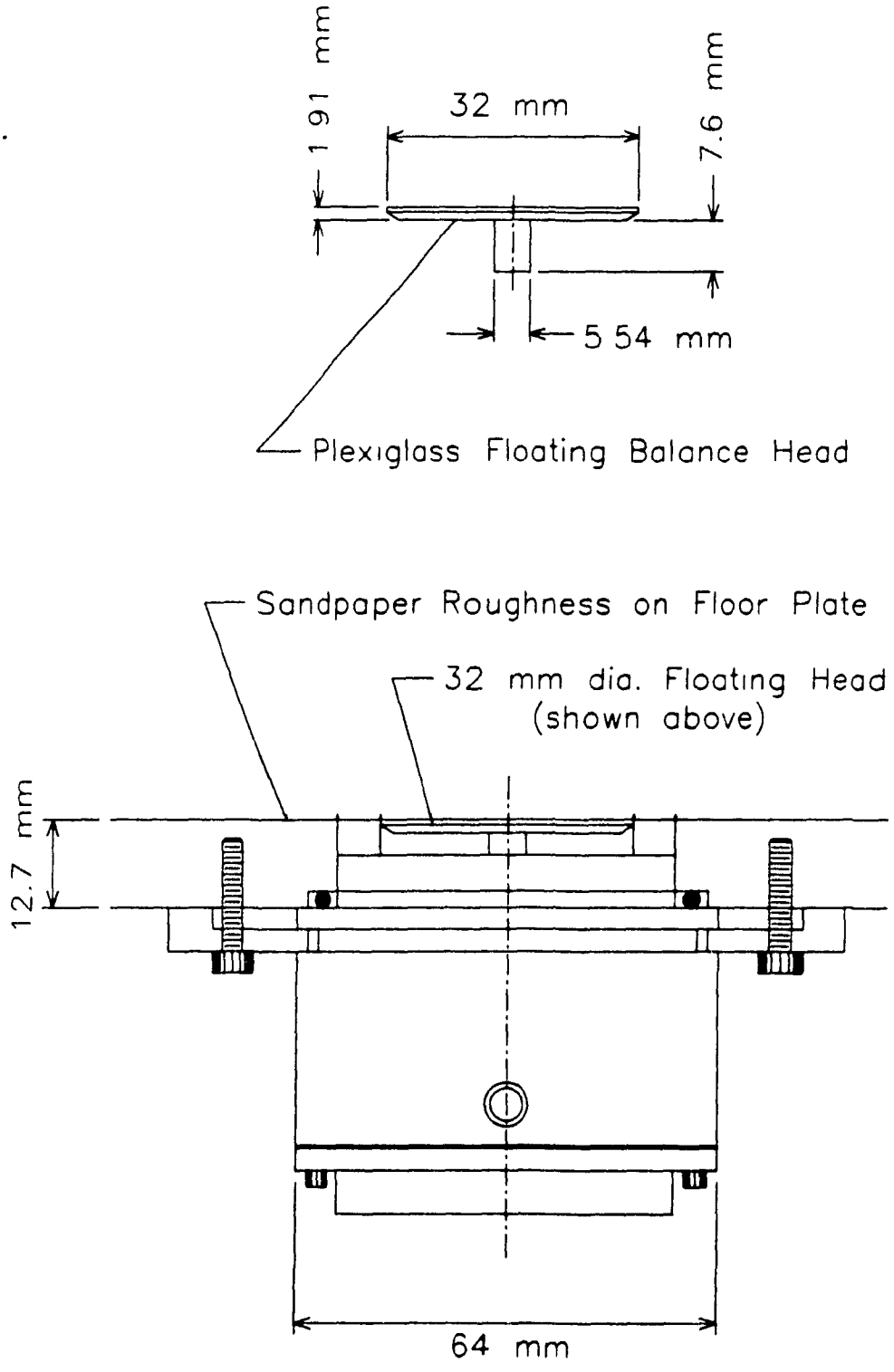

Figure 6.11: Skin Friction Balance

Chapter 7

RESULTS

This chapter presents the results of the experimental investigation. It is divided into three parts which give, respectively, the results of the uncertainty analysis, the preliminary boundary layer investigation, and the three tube investigation. The latter section is further divided into three subsections, examining separately the results of the three tube instrument operating on the three different surfaces which were used in the experiments.

7.1 Uncertainty Analysis

A detailed uncertainty analysis was performed for all measurements in accordance with common practice (Moffat [23]). The Nth-order single-sample uncertainty was determined for each measurement from the random and fixed error components. The random error component of each measurement was taken to be twice the standard deviation of a sample of thirty consecutive readings, providing a level of confidence of 95 percent. The fixed error component was estimated for each instrument based on reading error, small non-linearities in calibration, and other influences, such as the turbulence effect on pressure measurements discussed in Appendix E. The reading error was typically taken as one-half the smallest readable division of the instrument. The total uncertainty in each measured quantity was determined as the root-sum-square of the random and fixed components; the measurement are then considered accurate to within the stated uncertainty 19 times out of 20.

In performing calculations, such as the determination of the skin friction coefficient, uncertainties were combined in a root-sum-square fashion to preserve

the statistical reliability of the calculated result. Hence, final results were also considered accurate to within the calculated uncertainty to a level of confidence of 95 percent.

In the results which follow, the error bars are not shown for each point to avoid a cluttered appearance on the graphs. However, in most cases, a typical error bar, corresponding to data in the middle of the Reynolds number range, is shown to roughly demonstrate the magnitude of the uncertainties in the final values. For the most part, the uncertainties were larger at smaller Reynolds number, and vice versa, due to the influence of the fixed error component. The uncertainty in the Reynolds number itself is not shown because it is quite small, usually less than one percent. Also, error bars are not given for data plotted on a logarithmic axis or when the uncertainties were smaller than the symbols used to plot the data.

7.2 Boundary Layer Preliminary Investigation

Mean velocity profiles were obtained using the boundary layer rake on both the smooth surface and the wire screen roughness. One typical profile for each surface is shown in non-dimensional form in Figure 7.1. Also shown on this graph for comparison are two velocity traverses taken at the $x = 1.6$ m station: one on the smooth surface and one on the sandpaper roughness in the fully rough régime. It is evident from this figure that the surface roughness has a significant influence on the velocity profile shape.

7.2.1 Smooth Wall

The twenty-nine smooth wall profiles were analyzed to determine the skin friction coefficient using the modified von Kármán equation, Eq. 4.10, and equations A.6 and A.7 which define the quantities C_1 and C_2 in terms of δ, δ^*, θ, and λ. The velocity profiles were fit to a power law of the form $\overline{u} = ay^n$, and the boundary layer thickness was taken as the solution to this equation at $\overline{u} = \overline{U}$. The displacement and momentum thickness were calculated analytically from the assumed profile. Thus, Eqs. 4.10, A.6 and A.7 formed a set of three non-linear algebraic equations with the three unknowns C_1, C_2 and λ. The solution set was found by iteration, and c_f determined using $c_f = 2/\lambda^2$. The Reynolds number,

R_θ, was determined from θ and the measured value of $\overline{U}$. The results, shown in Figure 7.2, give c_f as a function of R_θ. Each data point corresponds to one of the twenty-nine velocity profiles taken at different longitudinal positions and free-stream velocities. Despite the crude power law approximation to the velocity profile, this analysis produced results with very little scatter. Skin friction data from every x station collapses onto a single curve, as expected.

Having obtained the skin friction values, the velocity profiles were non-dimensionalized by the wall friction velocity, yielding profiles of u^+ versus y^+. Six typical profiles are plotted in semi-log form in Figure 7.3. The other 23 profiles are similar, but are not shown for clarity and readability. The logarithmic region is evident and fits extremely well to Eq. 3.23 with the values $\kappa = 0.41$ and $B = 5.5$, as shown by the solid line. The wake also appears as expected; however, the viscous sublayer is not apparent. In fact, the lowest data point in each profile is in error, since it should appear either on the logarithmic law or slightly below. This error is probably due to the omission of the turbulence correction from the total pressure measurement. As described in Appendix E, the omission of this correction will produce values of the dynamic pressure which are too large close to the wall. Hence the determined u^+ values will be greater than the true values. Also contributing to this discrepancy is the error in the true vertical position of the pitot tubes, which would be large very close to the wall. Nevertheless, this near-wall data point is of negligible importance, since its effect on integrated boundary layer parameters, such as δ^* and θ, is negligible.

The drawback to the foregoing analysis procedure was the assumption that the smooth wall velocity profile, shown in Figure 7.1, could be accurately described by a power law. To overcome this, numerical integration was applied to each measured velocity profile to determine important boundary layer quantities such as the displacement and momentum thickness, δ^* and θ, and the shape factor, H. Skin friction coefficients were then calculated based on R_θ using two well known one-parameter skin friction laws: the $1/7^{th}$ power [46] and the Squire-Young [63] relations. The former gives the skin friction that one would expect if the profiles have the form $\overline{u}/\overline{U} = (y/\delta)^{1/7}$; therefore, it was believed to be less realistic than the previous power law approximation which allowed the exponent to be determined by a best fit of the data points. The Squire-Young relation is based on empirical results for smooth boundary layers in the absence of a pres-

sure gradient. The results are shown in Figure 7.4, along with those of Figure 7.2, obtained using the modified von Kármán relation. Despite the very different relations used to determine the skin friction and the application of one-parameter relations to a boundary layer with a small pressure gradient, the results are in very good agreement. The dashed line passing between the points is the best fit of the three sets of data. One should note that the Reynolds numbers for the von Kármán data are different from those of the other two skin friction relations because of the different manner in which the momentum thickness was calculated.

To account for the actual small favourable pressure gradient, two different two-parameter relations were used to relate c_f to R_θ and the shape factor $H \equiv \delta^*/\theta$. The Ludwieg-Tillmann [20] and Thompson [51] relations were applied to the integrated boundary layer data, and the results are shown in Figure 7.5. Ironically, the results have more scatter than those of the one-parameter relations, due to the large uncertainties in the calculated values of H, as shown in Figure 7.6. In fact, better agreement in the c_f results could be obtained if the value of H is assumed to be constant at 1.35, but this is, in essence, no different than the use of a one-parameter relation. Hence, the pressure gradient is much too insignificant to justify the use of two-parameter relations when this only introduces a greater amount of scatter in the calculated skin friction. The dashed line shown in Figure 7.5 is the same as that of Figure 7.4 and will hereafter be treated as the average of the skin friction relations.

Finally, two velocity profiles were chosen at random and hand plotted on a Clauser plot. The results obtained were skin friction coefficients of 0.00298 and 0.00265 at R_θ values of approximately 5200 and 7600 respectively. These points are also shown in Figure 7.5 and are in excellent agreement with the skin friction relations.

7.2.2 Wire Screen Roughness

For the seventy rough wall velocity profiles taken using the boundary layer rake on the wire screen roughness, several methods were used to determine the skin friction; however, none met with great success. First, Perry's graphical method [35] was attempted. A small amount, ϵ, was added to the y values of the data, and this amount was varied to give the best logarithmic fit of the data in the

logarithmic region of the boundary layer. However, due to the spacing between the pitot tubes on the rake, only about four or five pitot tubes were found to lie in the logarithmic region. This provided an insufficient number of data points to obtain an accurate value of ϵ and hence c_f; thus, Perry's method applied to the rake data was unsuccessful.

A second graphical method, involving a plot of $\overline{U} - \overline{u}$ versus $\ln(y/\delta)$, was also tried; however, this was also unsuccessful due to too few data points in the logarithmic region. Furthermore, this analysis was hampered by the difficulty of precisely determining the boundary layer thickness from the rake data. The results of this graphical method and Perry's method contain enormous scatter, but indicate generally that the skin friction coefficients are somewhere between 2.5 to 4 times those for the smooth wall.

Finally, the momentum integral equation, Eq. 4.1, was also applied to determine the skin friction coefficient on the rough wall. The results, shown in Figure 7.7, were found to be in rough agreement with those of the previous two methods, but with somewhat less scatter. The scatter in the values of c_f is about ± 15 percent and is primarily due to the large scatter in the values of H, and to lack of a sufficient number of boundary layer profiles at closely spaced intervals in x for accurate determination of the derivatives $d\theta/dx$ and $d\overline{U}/dx$. This method is not considered very reliable, since the smooth wall rake profiles were also analyzed in this manner and discrepancies as large as 70 percent were observed. This is more likely an indication of poor accuracy in determining the integral quantities from the rake profiles than a lack of two-dimensionality of the flow.

Nevertheless, a few general comments may be made concerning Figure 7.7. First, the Reynolds number range has been increased by a factor of approximately two from the smooth wall measurements. Since the same range of velocities and streamwise positions were used, this increase in Reynolds number is due entirely to the increase in θ, or in other words, the thickening of the boundary layer. This increase in boundary layer size is important for a number of reasons, including a larger logarithmic region of the boundary layer in which the three tube instrument can be used, and an increase in the longitudinal pressure gradient which was considered for the skin friction balance measurements (see Appendix D).

Secondly, the skin friction coefficients appear to be roughly independent of

Reynolds number. This would lead one to conclude that the boundary layer was in the fully rough régime. This speculation was checked by determining the Nikuradse equivalent sand roughness from the rake profiles. For most profiles the values of k_s^+ greatly exceeded seventy, verifying the fully rough régime.

7.3 Investigation of the Three Tube Instrument

The investigation of the proposed three tube instrument consisted of both smooth and rough wall measurements as described previously. For both surface conditions, the skin friction was calculated according to Eq. 5.15 and compared with those obtained by other means.

7.3.1 Smooth Wall

Three Tube Instrument

The skin friction coefficients determined using the three tube instrument are shown as a function of Reynolds number in Figure 7.8. Results of four different vertical positions of the instrument are shown. These correspond to the center tube position, y_2, between 3.3 mm and 5.0 mm from the wall. Significant scatter of the data is apparent, but there is very good agreement with the skin friction laws, given by the dashed curve, for Reynolds numbers greater than about 8000. For most of the data points the agreement is within the experimental uncertainty and independent of the vertical position of the instrument. The scatter of about ± 10 percent is a consequence of the experimental difficulty in accurately measuring the pressure differences Δ_{12} and Δ_{23}. These pressures were typically 10 Pa to 50 Pa, and due to the turbulent fluctuations, the measurement accuracy was about ± 1 Pa at best. Hence, these pressures could not be measured with great accuracy. Furthermore, the skin friction coefficient is dependent on the difference in the reciprocals of these two pressures, and since they have nearly the same magnitude, c_f becomes quite sensitive to the exact determination of Δ_{12} and Δ_{23}. In view of this, the agreement at the higher Reynolds number is exceptionally good. At lower speeds, however, the pressure differences become much smaller and the determination of c_f increasingly difficult.

At the lower Reynolds numbers, some discrepancies exists between the data

points and the skin friction laws, and the deviations appear to increase with proximity to the wall. This leads one to believe that the deviations are more than simply a loss of accuracy in the pressure measurements at the lower velocities. One might expect that as the free-stream velocity is decreased, the shear velocity also decreases, and eventually the lower of the three tubes may drop to a y^+ value below the range of the logarithmic region, and therefore Eq. 5.15 would no longer apply. As shown in Figure 7.9, the y^+ values of the lowest pitot tube behave anomalously at the lower Reynolds number for the two positions of the apparatus closest to the wall. However, the y^+ values never fall below the expected lower limit of 30; therefore, the pitot tubes always remain within the theoretical logarithmic region over this range of Reynolds number. This then is probably the wrong explanation.

Another possible explanation is that the omission of the turbulence corrections, discussed in Appendix E, may introduce a significant error. Since the turbulence is greatest near $y^+ \approx 30$, the omission of the turbulence correction would produce the greatest error for the pitot tube closest to the wall with the instrument in the lowest position. To investigate this possibility the three tube measurements were re-analyzed, treating each pitot tube individually in an attempt to discover which of the three tubes was causing the anomalous skin friction values below $R_\theta \approx 8000$. From the measured values of $\overline{q}_2$, Δ_{12} and Δ_{23}, the velocity at each pitot tube was determined. With the appropriate y value, each $(y, \overline{u})$ pair corresponds to a single point on a Clauser plot with a particular skin friction coefficient. Thus, c_f was determined for each individual pitot tube in the instrument, and plotted as a function of Reynolds number. Some of the results are shown in Figure 7.10. For all cases, including those not shown, the results are in very good agreement with the one-parameter skin friction laws. However, a small discontinuity near $R_\theta \approx 8000$ is evident in the results corresponding to the lowest pitot tube. Although the discontinuity is small when the measurements are analyzed using the Clauser plot, the effect may be considerably larger when the data is analyzed using Eq. 5.15. Therefore, the discrepancies in Figure 7.8 appear to be the result of the near-wall pitot tube; however, it is difficult to state the true cause of the deviations.

Preston Tubes

Three different sizes of Preston tubes were also used as a check on the skin friction and the law of the wall. The results are shown in Figure 7.11, in which Patel's calibration [30] was used to determine c_f. The agreement is extremely good, especially at the higher Reynolds number. The apparent disagreement between the smallest Preston tube and the other two below $R_\theta \approx 7800$ is due to Patel's piece-wise calibration, in which there is a discontinuous jump at this particular Reynolds number for the smallest tube. The same discontinuity occurs for the intermediate and largest Preston tubes at Reynolds numbers of approximately 4800 and 4000 respectively, as shown in Figure 7.11.

Velocity Traverses and Clauser Plot

Two very detailed velocity traverses of the smooth wall boundary layer were taken with the traversing apparatus of Figure 6.8. These profiles were analyzed by the Clauser plot method, and then non-dimensionalized with the friction velocity. The traverses, plotted in log law form, are shown in Figure 7.12. The logarithmic region falls exactly on Eq. 3.23 shown by the solid line, and the skin friction coefficients are in excellent agreement with those of the previous methods. As in Figure 7.3, the errors close to the wall are apparent in the lowest few data points.

Skin Friction Balance

Finally, to finish the smooth wall investigation, the skin friction balance was used to measure the wall shear stress directly. This method is not based on a similarity technique, and thereby affords a fundamentally distinct determination of the skin friction. The results are shown in Figure 7.13, in which the two orientations indicated refer to a zero or 180 degree rotation of the balance about its centerline. The balance can operate equally well in either orientation; therefore, both orientations were used for the purpose of verification. The results are in excellent agreement with the skin friction laws, indicated by the dashed line, and Preston tubes. However, at the largest Reynolds number, the two orientations disagree by about five percent. A probable explanation for this small discrepancy is a very small inclination of the balance head relative to the floor

of the wind tunnel. Such an inclination would result in a small difference in the shear stresses for the two orientations, and this difference would be expected to increase with Reynolds number. This possibility was investigated further, and it was discovered that an inclination of only 0.05 mm across the diameter of the head produced skin friction coefficients which differed by as much as fifteen percent in the two orientations.

7.3.2 Sandpaper #40 Roughness

The first rough wall to be tested with the three tube instrument was produced using sandpaper of grit size #40, with a measured average roughness size of k = 0.46 mm.

Skin Friction Balance

Since no rough skin friction laws exist, the skin friction balance was used as the reference to which the three tube instrument is compared. The results of the skin friction balance are shown plotted as c_f versus R_θ in Figure 7.14. As before, the two orientations refer to a zero or 180 degree rotation of the balance relative to the flow direction. The results for both orientations are in excellent agreement, and the scatter, which is about ± 2 percent, is less than that for the smooth wall measurements. This is not unexpected, since the shear stress is about fifty percent higher, making the measurements somewhat more accurate, and because the presence of the roughness make the balance output less sensitive to the alignment error discussed in the previous section. The dashed line shown in Figure 7.14 is simply a best fit of the data points, and has no other significance. The general trend of the skin friction is opposite to that of the smooth wall data, in that it is increasing with Reynolds number. According to resistance diagrams for sand-roughened plates [46], this indicates immediately that the wall is in the intermediate roughness régime between effectively smooth and fully rough. This was verified upon the determination of $k_s^+ = k_s u_\tau / \nu$, which is also shown in Figure 7.14 as a function of Reynolds number. For visual clarity, only every third data point was plotted in this graph. The equivalent sand roughness, k_s, was found to be 0.41 mm from the velocity traverses, described below. The k_s^+ values ranged from approximately seven at the lowest speed to nearly 60 at the

maximum speed, covering most of the transitional roughness régime. These k_s^+ values are in excellent agreement with the trend of the measured skin friction coefficients. At low Reynolds number the skin friction is expected to increase with decreasing Reynolds number because the wall is becoming effectively smooth. This increase in the c_f at the lowest Reynolds numbers is apparent, and would be more evident if values of k_s^+ below five could have been obtained. However, accurate measurements could not be made at such low wind tunnel speeds. At the high Reynolds numbers the flow is approaching the fully rough régime, as indicated by the k_s^+ values. By extrapolating these values to $k_s^+ = 70$, one would expect the skin friction curve to become flat around a Reynolds number of perhaps 21000.

Velocity Traverses and Perry Plot

The Reynolds numbers given in Figure 7.14 were determined with the aid of velocity traverses. Velocity traverses consisting of approximately seventy data points were taken at four different wind tunnel speeds using the apparatus shown in Figure 6.8. The mean velocity profiles were numerically integrated to determine the momentum thickness as a function of the wind tunnel speed. The correct origin of y for the traverse data was not required in this integration since the value of θ is nearly insensitive to the choice of origin. Having obtained the momentum thickness, the Reynolds number, R_θ, was determined as given above. As expected, the Reynolds numbers are generally larger for the rough wall boundary layer than for those of the smooth due to the increase in the momentum thickness.

The skin friction coefficient was also determined by Perry's method using the detailed velocity traverse data. In contrast to the rake profiles, there were a sufficient number of traverse points to apply this method successfully. For each traverse, the origin offset, ϵ, was varied until a logarithmic region was obtained on a plot of u^+ versus y^+. Results for three of the profiles are shown in Figure 7.15, along with the two smooth wall traverses for comparison. The logarithmic regions (dashed lines) are evident and, as expected, are parallel to the smooth wall logarithmic region (solid line). The values of u^+ are reduced below the smooth wall values by an amount which depends on the roughness parameter $k_s u_\tau/\nu$, and in this manner, the value of k_s was determined for this roughness.

The wake regions are also clearly shown, and as with the smooth wall profiles, the loss of accuracy near the wall is evident in the lowest few traverse points. Finally, the skin friction coefficients determined by Perry's method, shown in the figure, agree with those of the skin friction balance.

Three Tube Instrument

The three tube instrument was set at four different vertical positions ranging from approximately 2.8 mm to 5.1 mm, as measured from the top of the roughness to the center pitot tube. The skin friction coefficients were calculated using Eq. 5.15 over a range of Reynolds number from about 7000 to approximately 17000. As in the smooth wall case, corrections were made for the effect of viscosity on the pressure measurements, and the effect of the non-uniform velocity profile on the value of ζ. The results are shown in Figure 7.16 as c_f versus R_θ. The vertical scale has been changed considerably from that of Figure 7.14 to account for a much increased amount of scatter in the data. The data is in general agreement with that of the skin friction balance, indicated by the dashed line, and independent of the vertical position of the instrument. The agreement is within the experimental uncertainty; however, the scatter is typically ± 10 percent. As in the smooth wall results, this scatter is due primarily to the difficulty in obtaining accurate measurements of the small pressure differences Δ_{12} and Δ_{23}.

The three data points with the lowest Reynolds number have calculated skin friction values much lower than would be expected by pure random error. It was thought that these three points might be in error as a result of the pitot tube instrument being below the logarithmic region of the boundary layer. The values of y^+ for the lowest pitot tubes were calculated and are shown in Figure 7.17. The three points in question correspond to the lowest values of y^+, of approximately 35, 50 and 70 respectively. As indicated by the velocity traverses of Figure 7.15 the lowest pitot tube is probably below the logarithmic region for these three cases. Hence, for these points, Eq. 5.15 does not apply.

Finally, since the skin friction data of Figure 7.16 appear to be randomly distributed about the results of the skin friction balance, a numerical technique was applied to the data to reduce the scatter and extract the trend of the data. This technique, called Gaussian smoothing, removes the scatter from the data by averaging data at different Reynolds numbers, but weighting the data by a

Gaussian distribution. At a given Reynolds number, the skin friction coefficient is determined from the weighted average of all the other data points, with the greatest weight given to the nearest points, according to a Gaussian distribution. This technique has its origins in signal noise reduction, in which a continuous signal is cross-correlated with a Gaussian function to reduce the noise, and in time series analysis where data smoothing over time is performed to extract the trend from a set of data. The Gaussian smoothing operation provides a variable parameter, the standard deviation of the Gaussian function, which can be adjusted to give the desired degree of smoothing. A trial and error procedure was used to determine the best compromise between too much smoothing and not enough elimination of the scatter, and the value chosen was 150 (corresponding to the Reynolds number scale). The Gaussian smoothed skin friction coefficients for the sandpaper #40 results are shown in Figure 7.18. At the lower Reynolds numbers, where the data is more dispersed, the smoothing procedure has little effect on the data; however, the smoothing is very substantial at the higher Reynolds numbers and the trend falls very close to the results obtained with the skin friction balance. These results indicate that with improved measurement accuracy the scatter in Figure 7.16 could be reduced, giving better agreement between the three tube instrument and the skin friction balance.

7.3.3 Sandpaper #24 Roughness

The second sandpaper was chosen with a grit size of #24 and measured average roughness dimension of $k = 0.81$ mm to obtain, if possible, non-dimensional roughness values in the fully rough régime at the highest wind tunnel speeds.

Skin Friction Balance

Figure 7.19 shows the skin friction coefficients calculated from the skin friction balance measurements. Excellent agreement exists between the results corresponding to the two orientations of the balance. As before, the dashed line in this figure is merely a best fit line to the balance data points. Over most of the Reynolds number range the flow is in the intermediate régime, and only above a Reynolds number of about 16000 is flow in the fully rough régime. This is confirmed in the small plot of k_s^+ versus Reynolds number in the corner of Fig-

ure 7.19. The equivalent sand roughness was found to be $k_s = 0.54$ mm from the velocity traverses described below. This value is considerably lower than the typical grain size for this sandpaper; however, the bond on this paper was much thicker than on the previous paper, and therefore the sand protrudes out from the bond by a much smaller amount relative to the size of the grains. Hence, this sandpaper is aerodynamically less rough than one would expect from the measurement of the grain size alone. Nevertheless, the calculated values for k_s^+ range from approximately 15 to 85; the upper limit confirms the fully rough régime at the highest Reynolds numbers.

To investigate the accuracy of the skin friction balance, measurements were repeated with the balance head both above and below the surrounding surface. Using a microscope, the head was re-positioned vertically by approximately one-half the gap size, or about 0.08 mm. The resulting values of c_f are given in Figure 7.20 along with those corresponding to the head in the centered position. This centered position was also judged under a microscope and was considered to be in alignment with the surroundings to an accuracy of 0.025 mm. This figure shows that a vertical displacement of the balance head by this considerable amount changes the value of c_f by only a few percent. Since the centering of the head could be performed well within these limits, the balance measurements were considered to be very reliable.

As an added check on the balance results in the fully rough régime, the skin friction was calculated using Schlichting's fully rough relation [46]:

$$c_f = \left(2.87 + 1.58 \log_{10} \frac{x}{k_s}\right).$$

Since the true x-origin was uncertain, only an estimate of c_f was obtained using the value of $x = 1.6$ m. In light of the uncertainty in x, the estimated skin friction coefficient, having a value of 0.00532, was found to agree well with Figure 7.19.

Velocity Traverses and Perry Plot

Velocity traverses were taken at five different Reynolds numbers, two of which were in the fully rough régime. These traverses were also analyzed using Perry's graphical procedure to obtain the skin friction coefficients and the equivalent sand roughness. Three of these traverses are shown in log law form in Figure 7.21, along with the two smooth wall traverses for comparison. The logarithmic

regions are clearly evident (dashed lines), and the skin friction coefficients are in very good agreement with the skin friction balance results.

Three Tube Instrument

The results for the three tube instrument are shown in Figure 7.22. Five different vertical positions were examined, varying from 3.3 mm to 6.6 mm as measured from the center pitot tube to the top of the roughness elements. The skin friction coefficients were calculated using Eq. 5.15 over a range of Reynolds number from about 8000 to approximately 18000. The results are in generally good agreement with those of the skin friction balance; however, as before, the scatter is typically ± 10 percent due to the measurements of the small pressure differences Δ_{12} and Δ_{23}. Gaussian smoothing was also applied to this data to remove the random scatter and the results, shown in Figure 7.23, once again reveal that very good agreement between the three tube instrument and the skin friction balance could be obtained with improved instrumentation.

Finally, the y^+ values corresponding to the lowest pitot tube are shown in Figure 7.24, providing evidence that the instrument was located in the logarithmic region of the boundary layer.

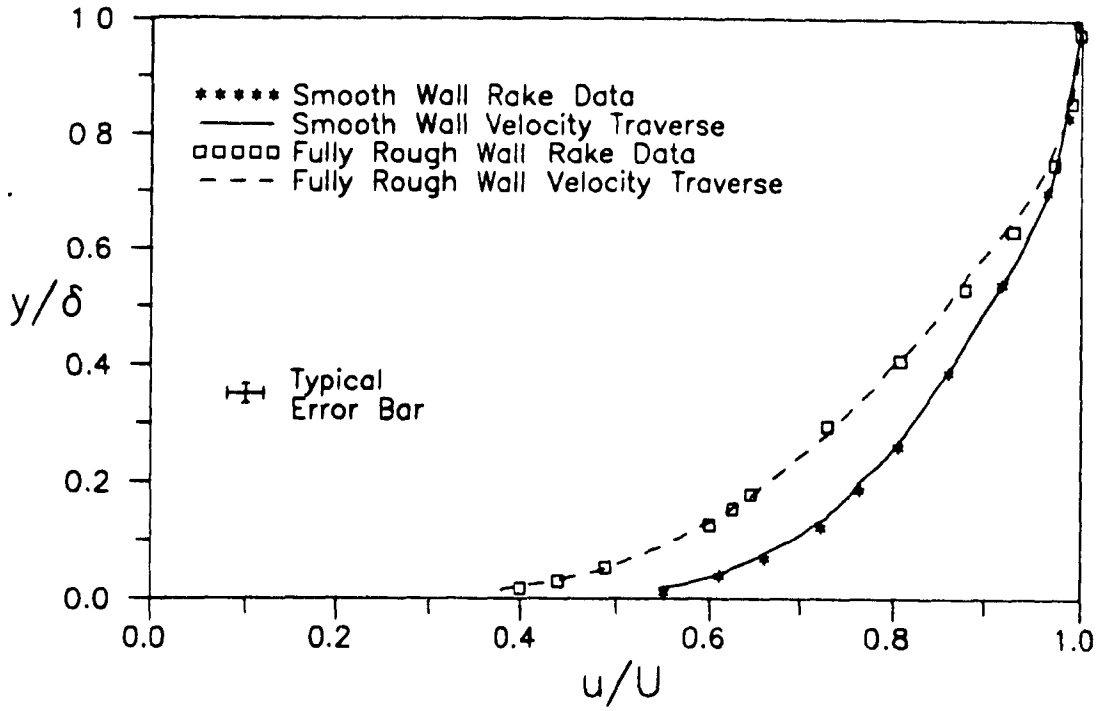

Figure 7.1: Typical Boundary Layer Velocity Profiles

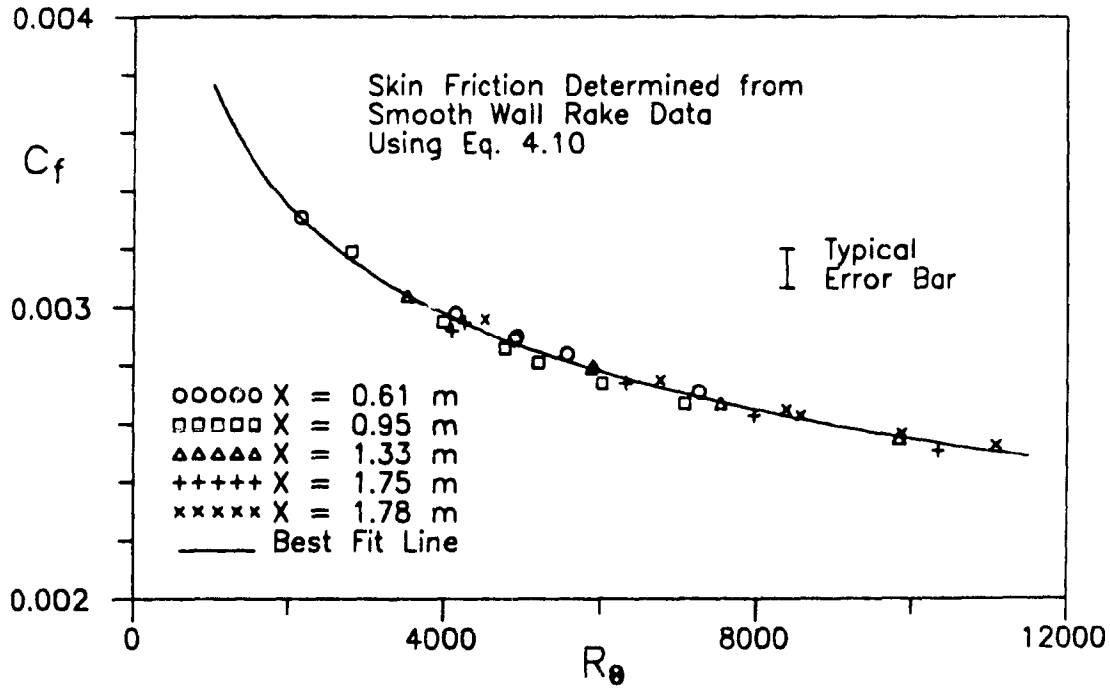

Figure 7.2: Smooth Wall Skin Friction from the Von Kármán Relation

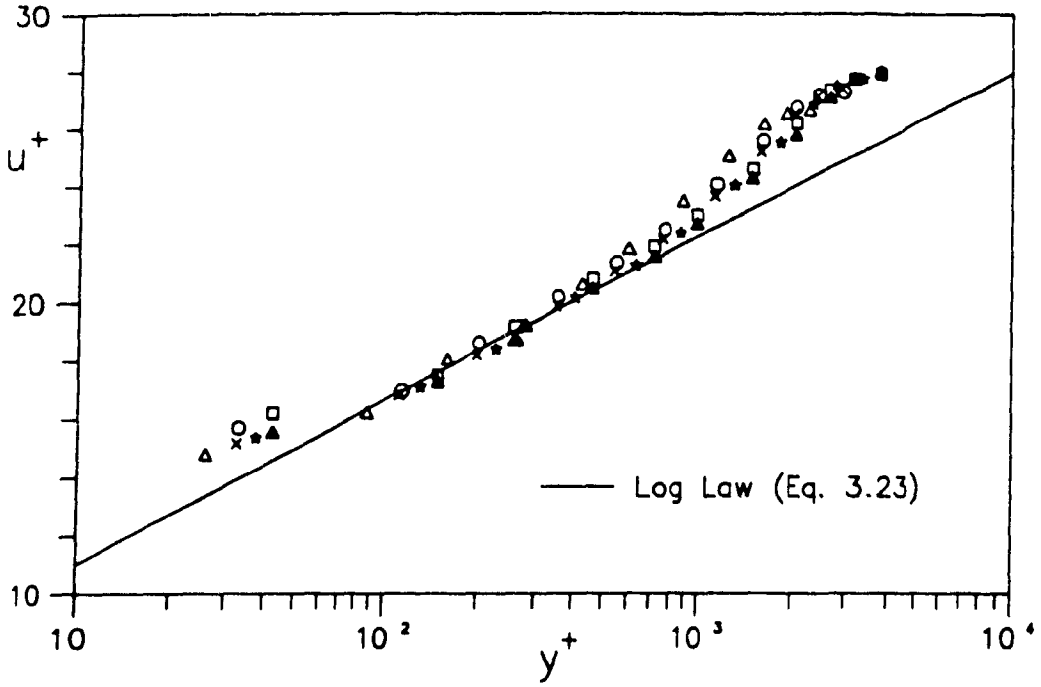

Figure 7.3: Sample Rake Data Smooth Wall Velocity Profiles in Logarithmic Form

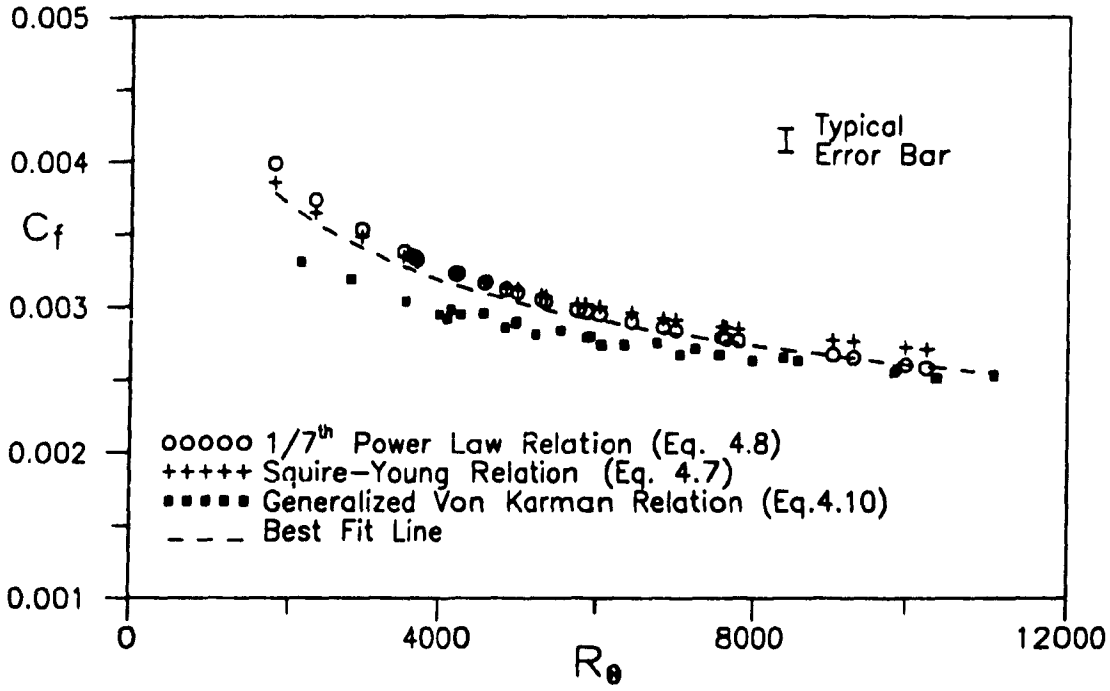

Figure 7.4: One-Parameter Skin Friction Relations for Smooth Wall Rake Data

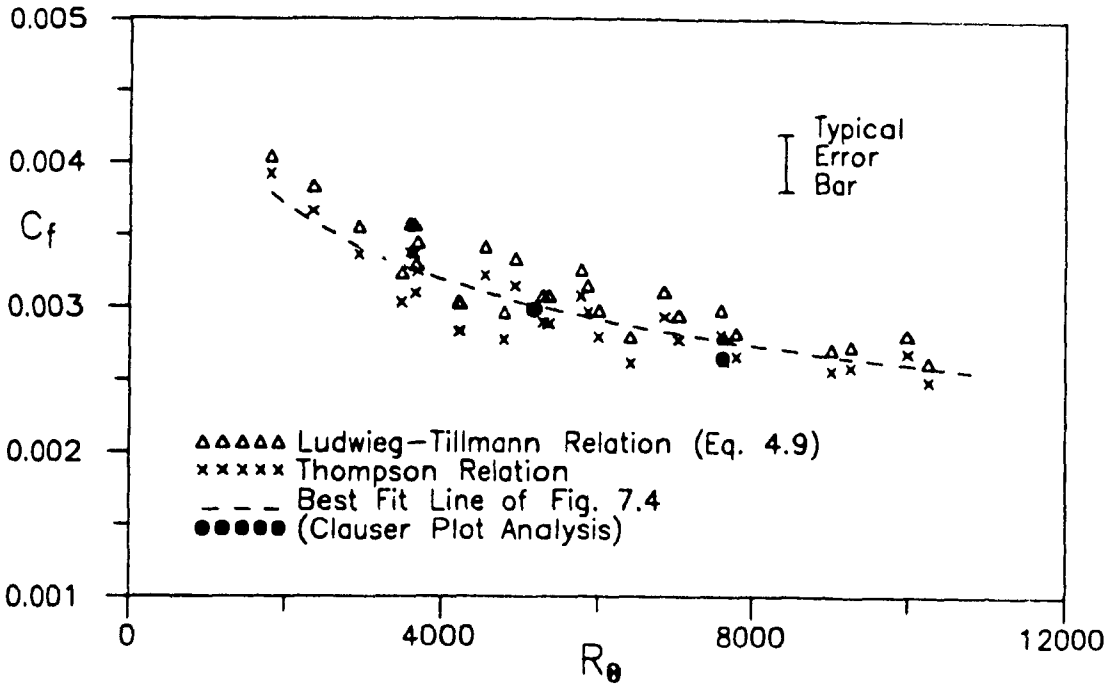

Figure 7.5: Two-Parameter Skin Friction Relations for Smooth Wall Rake Data

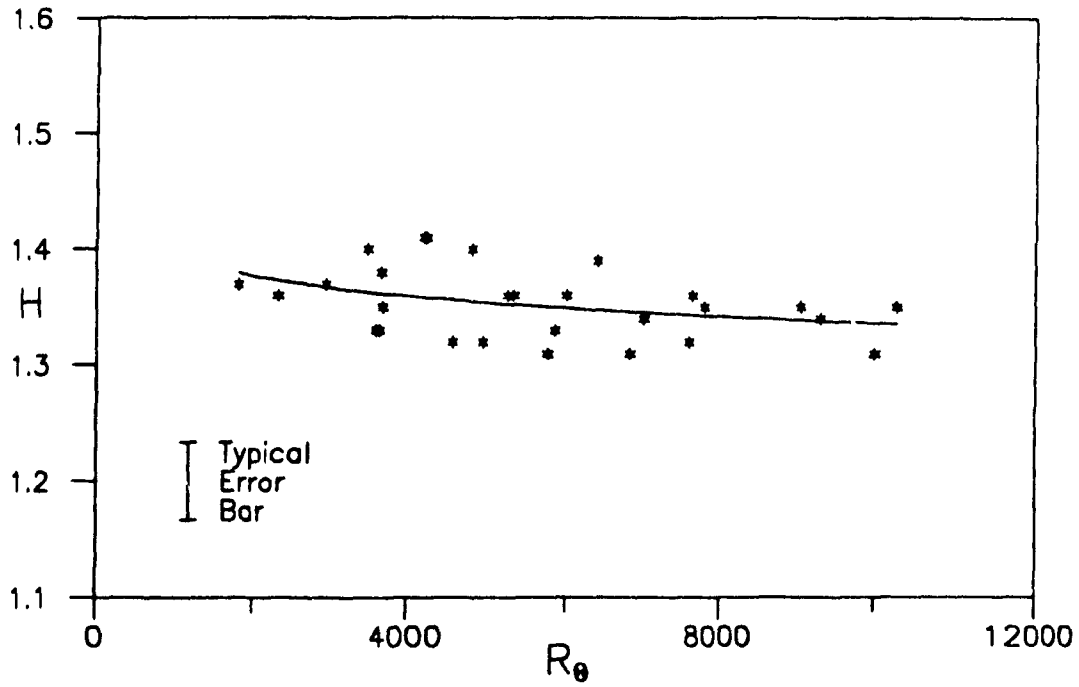

Figure 7.6: Shape Factor from Smooth Wall Rake Data

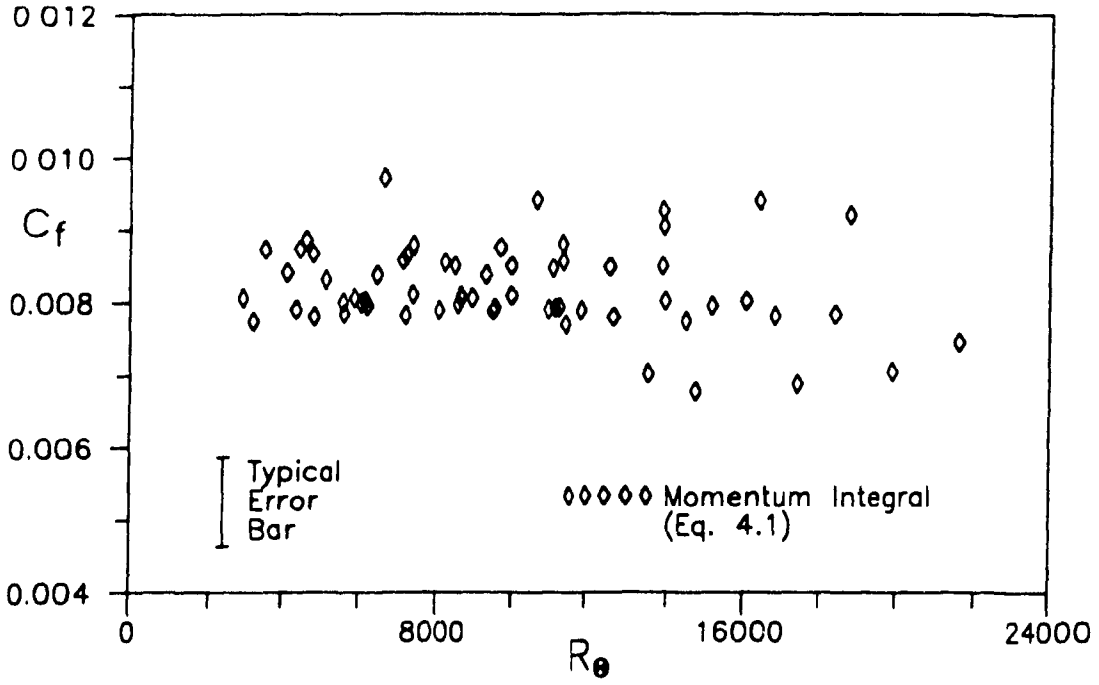

Figure 7.7: Skin Friction from Rake Data on Wire Screen Roughness using the Momentum Integral Equation

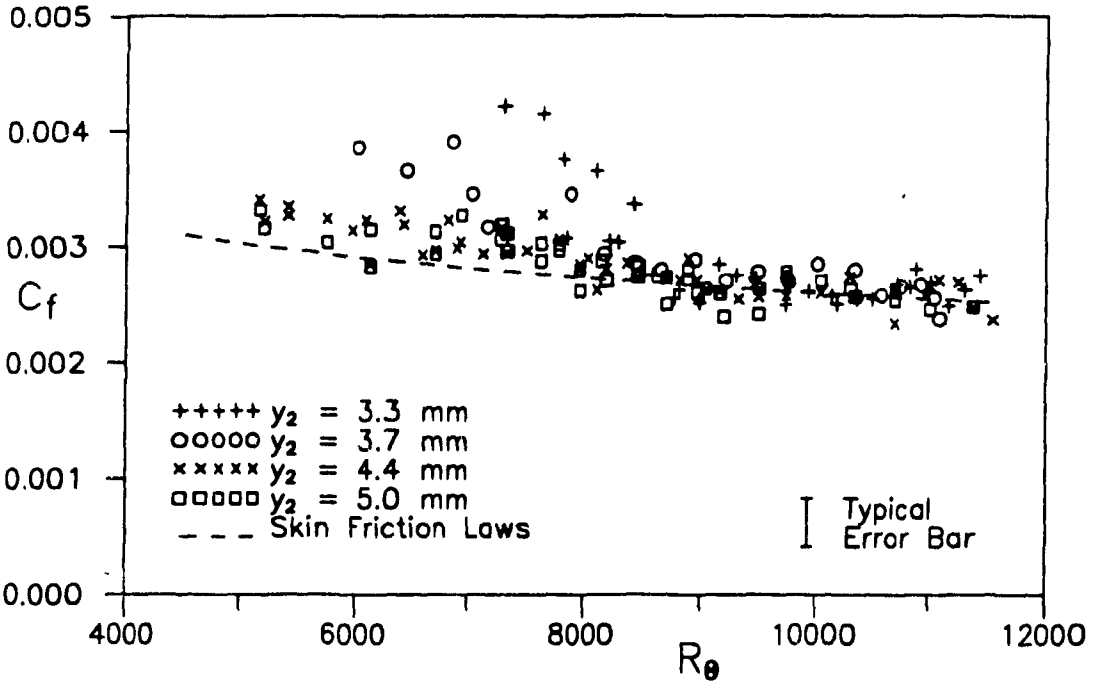

Figure 7.8: Smooth Wall Skin Friction Determined using Three Tube Instrument

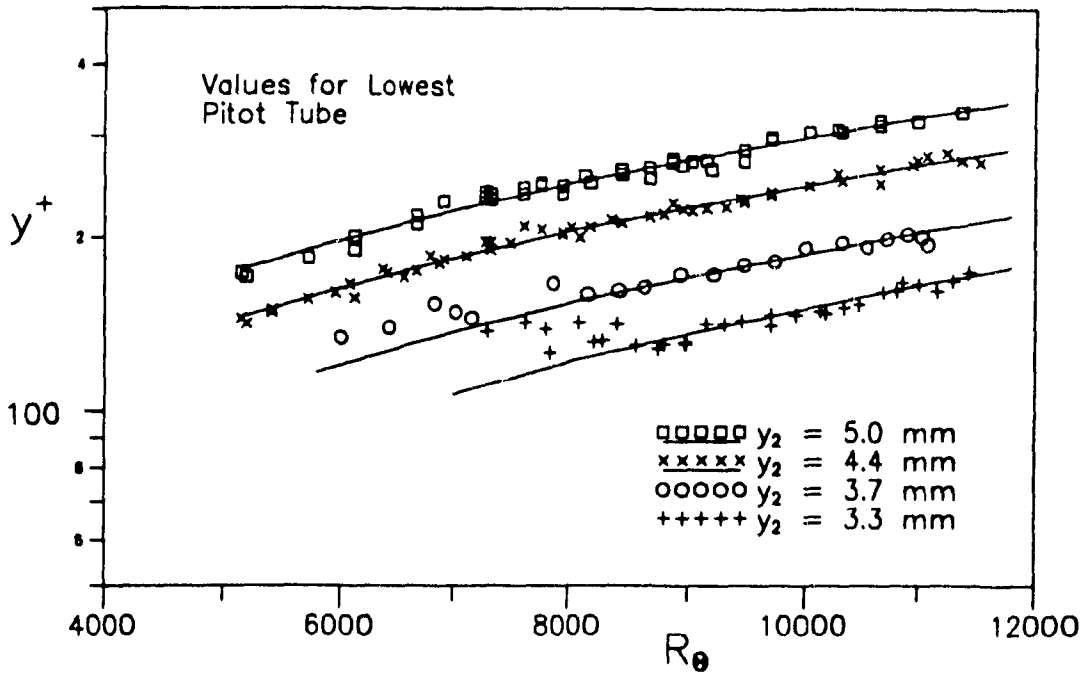

Figure 7.9: Smooth Wall y^+ Values for the Lowest Pitot Tube

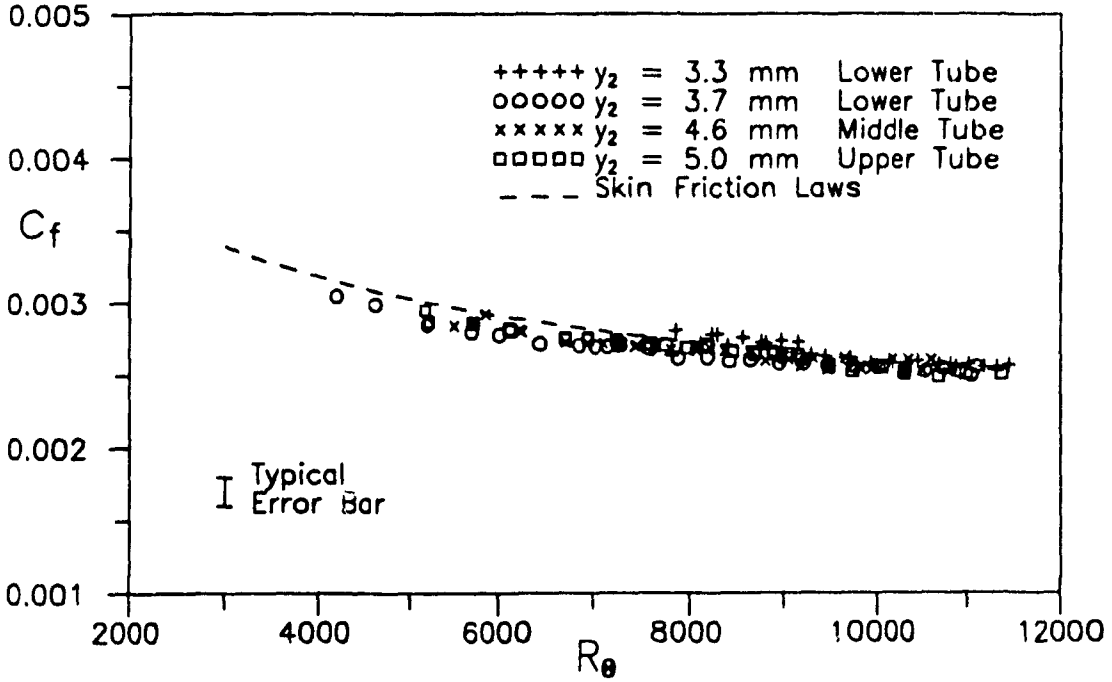

Figure 7.10: Sample Skin Friction from Clauser Plot Analysis

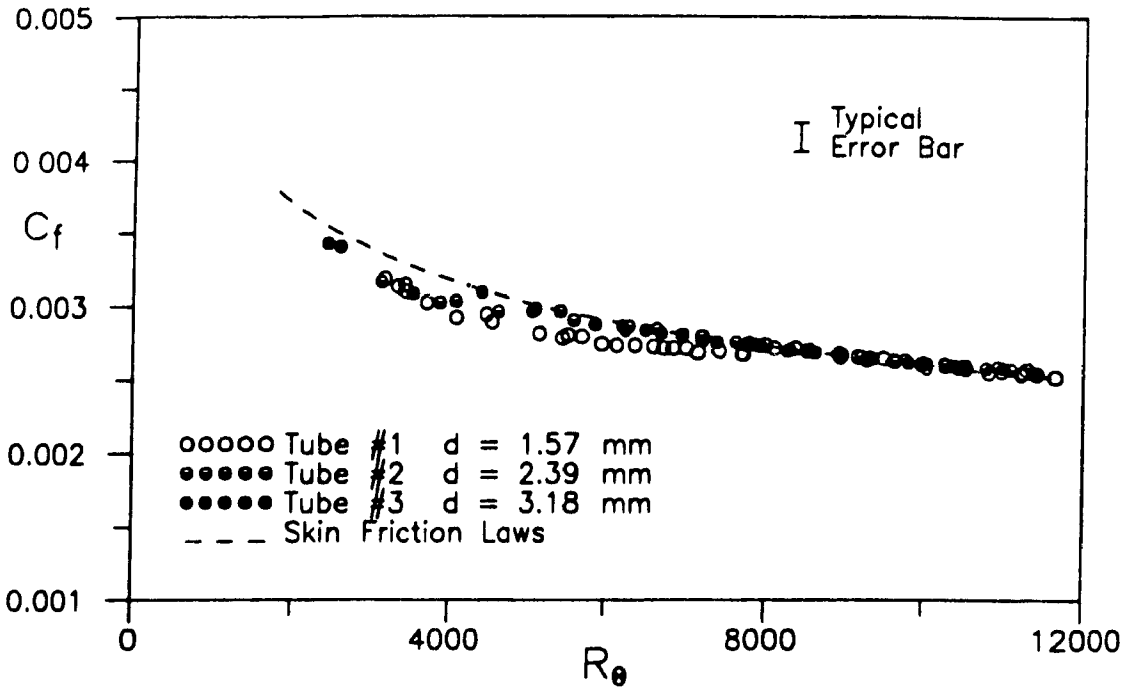

Figure 7.11: Smooth Wall Skin Friction Determined using Preston Tubes

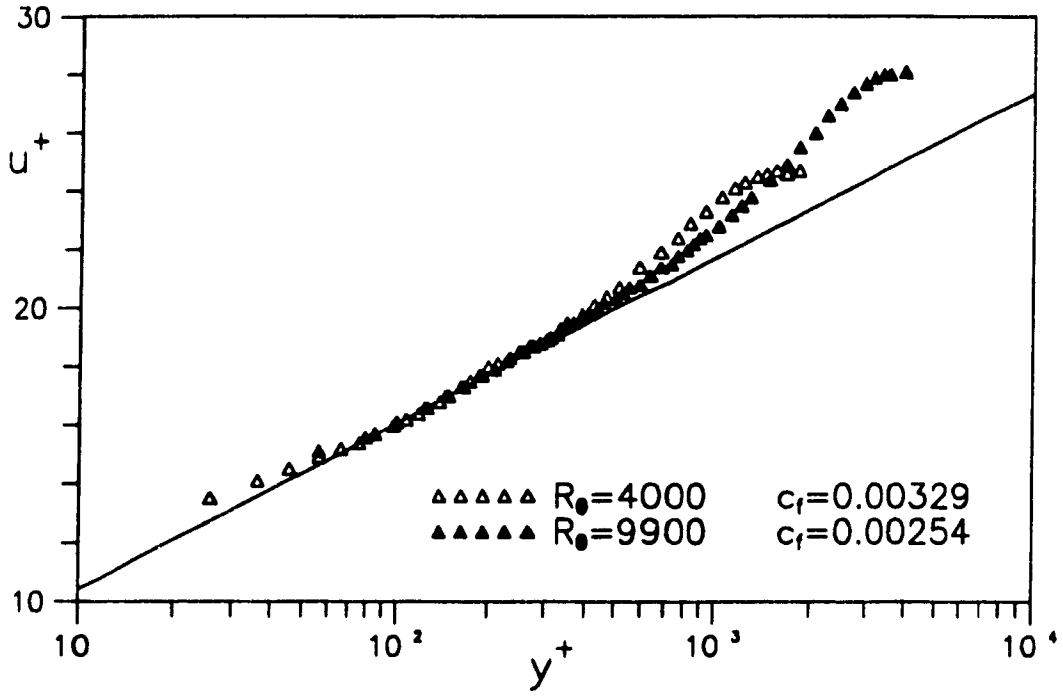

Figure 7.12: Smooth Wall Velocity Traverses in Logarithmic Form

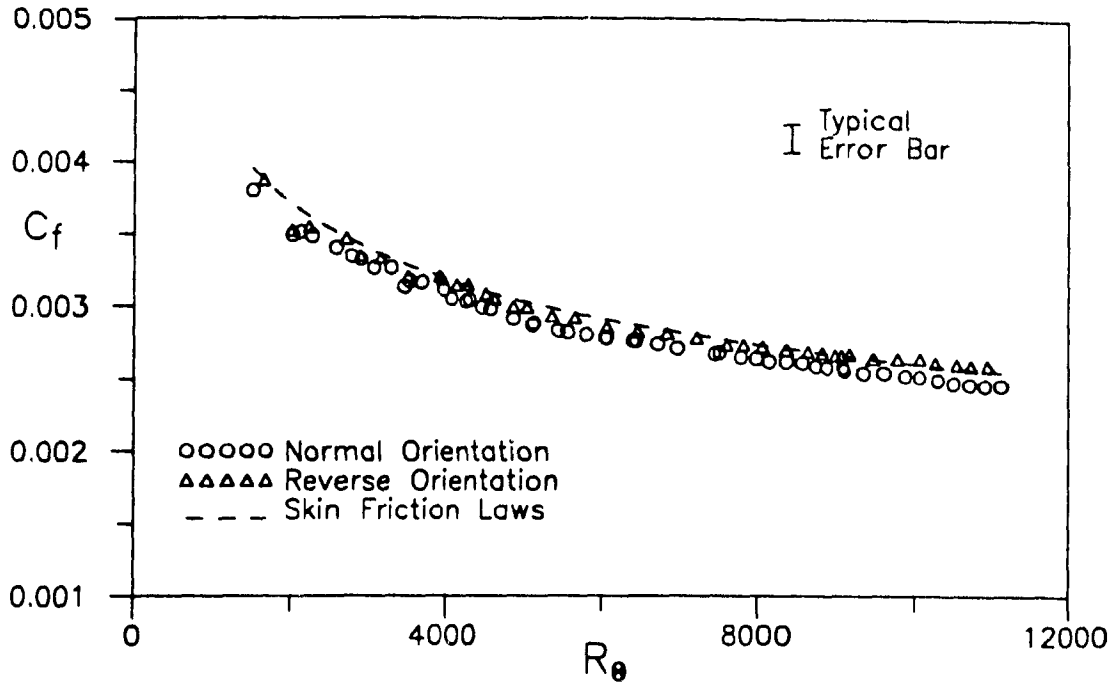

Figure 7.13: Smooth Wall Skin Friction Balance Results

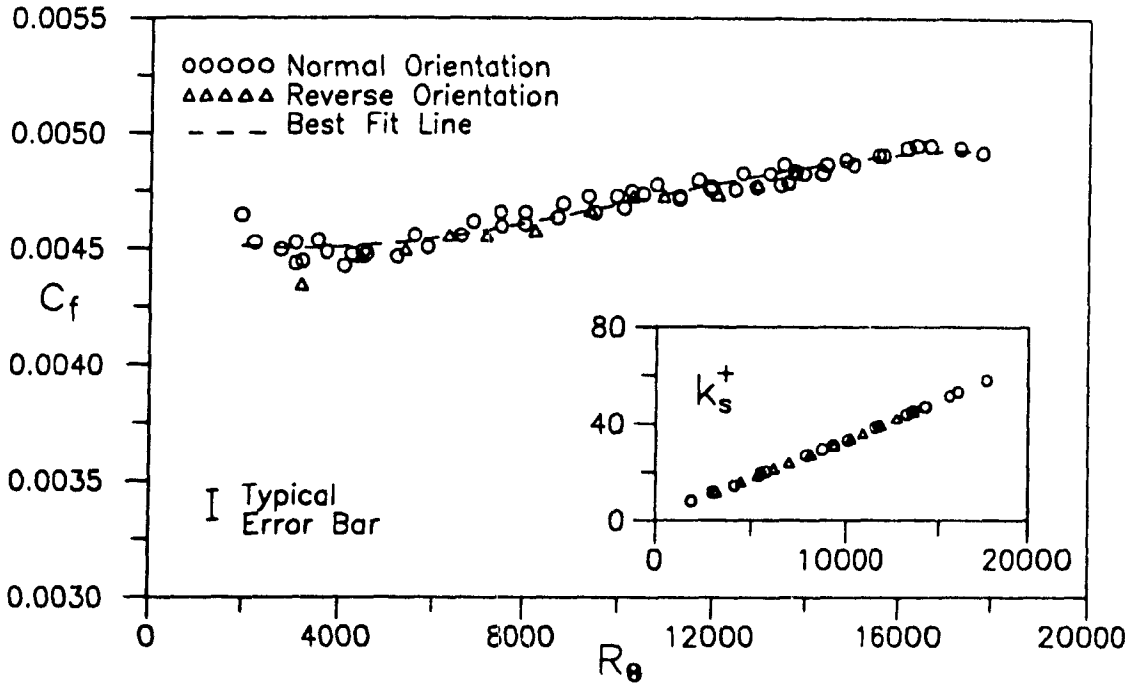

Figure 7.14: Sandpaper #40 Skin Friction Balance Results

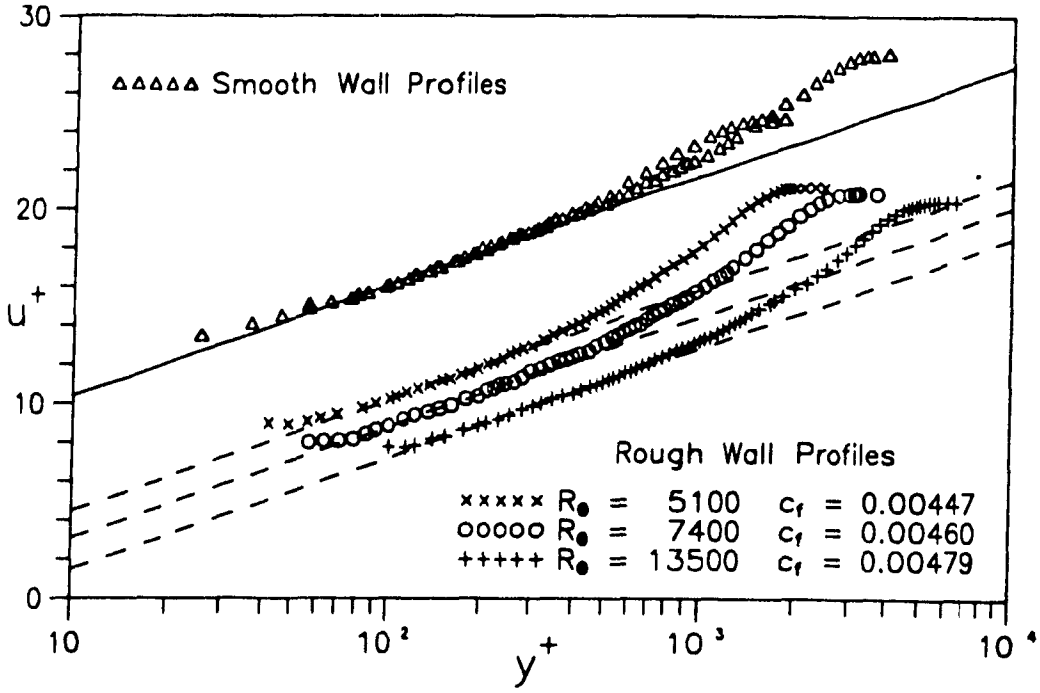

Figure 7.15: Sandpaper #40 Velocity Traverses in Logarithmic Form

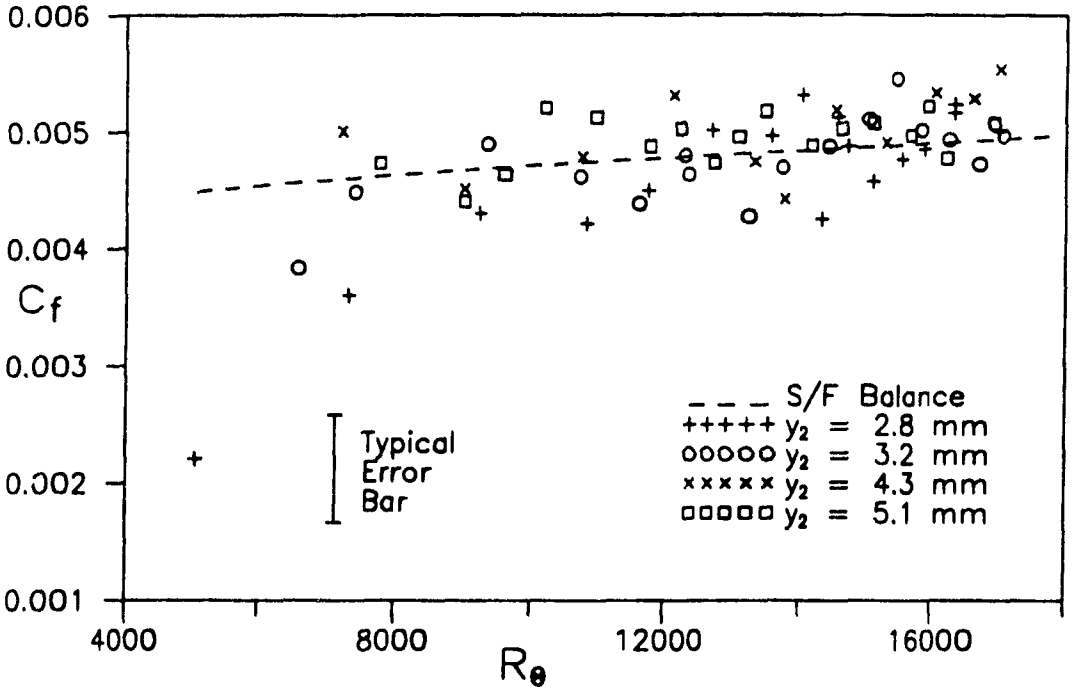

Figure 7.16: Sandpaper #40 Skin Friction Determined using Three Tube Instrument

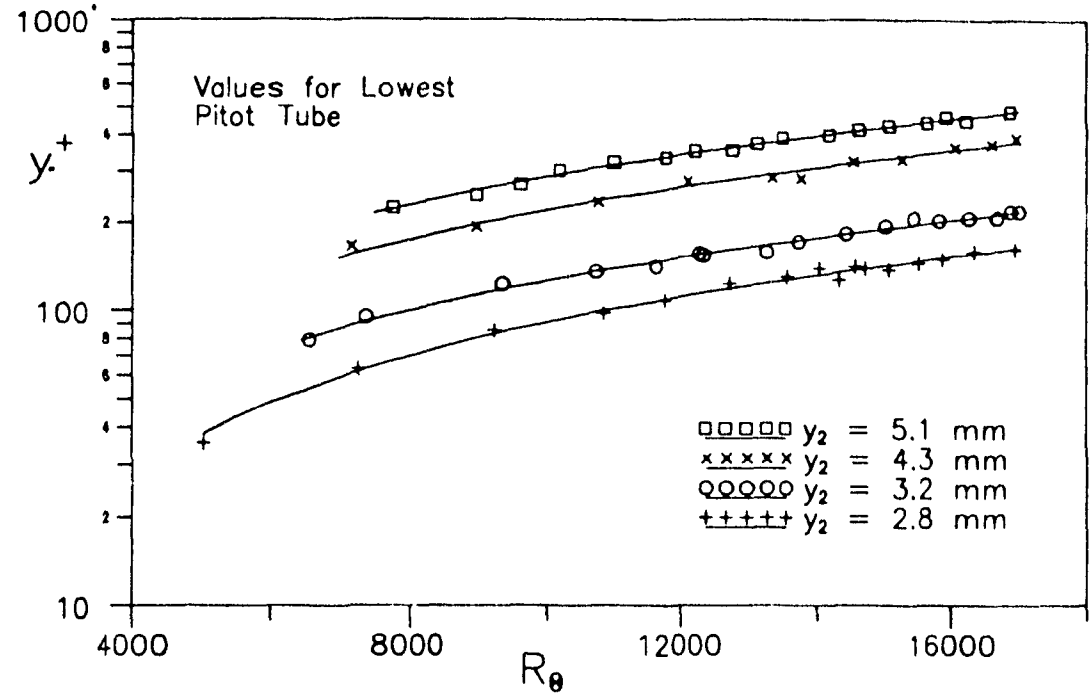

Figure 7.17: Sandpaper #40 y^+ Values for the Lowest Pitot Tube

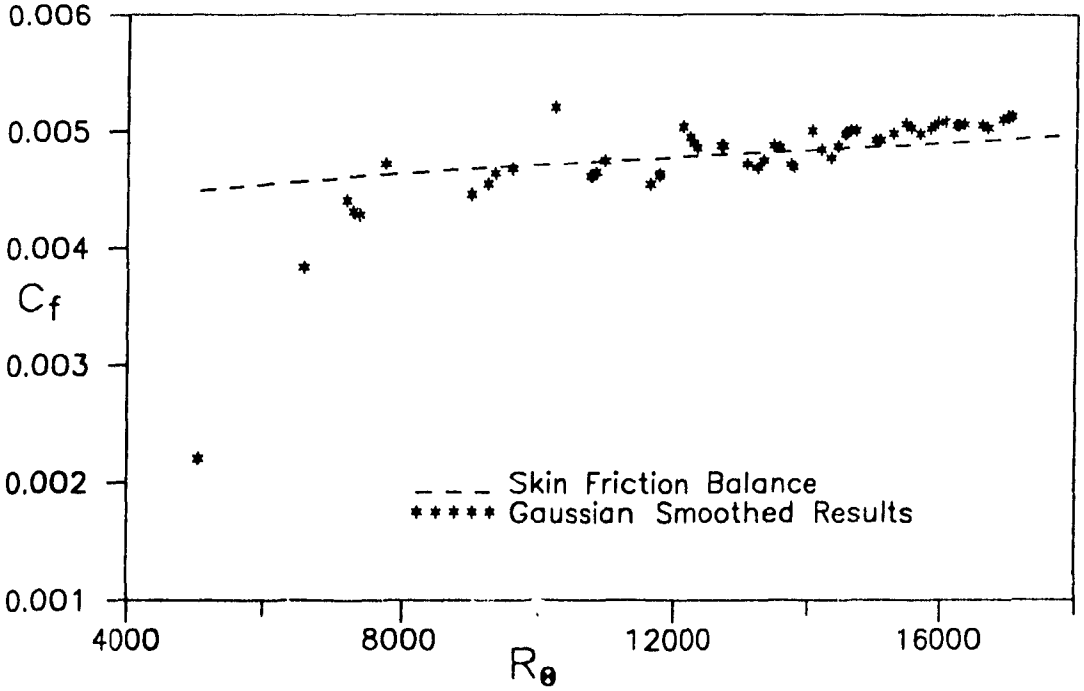

Figure 7.18: Sandpaper #40 Gaussian Smoothed Skin Friction Data

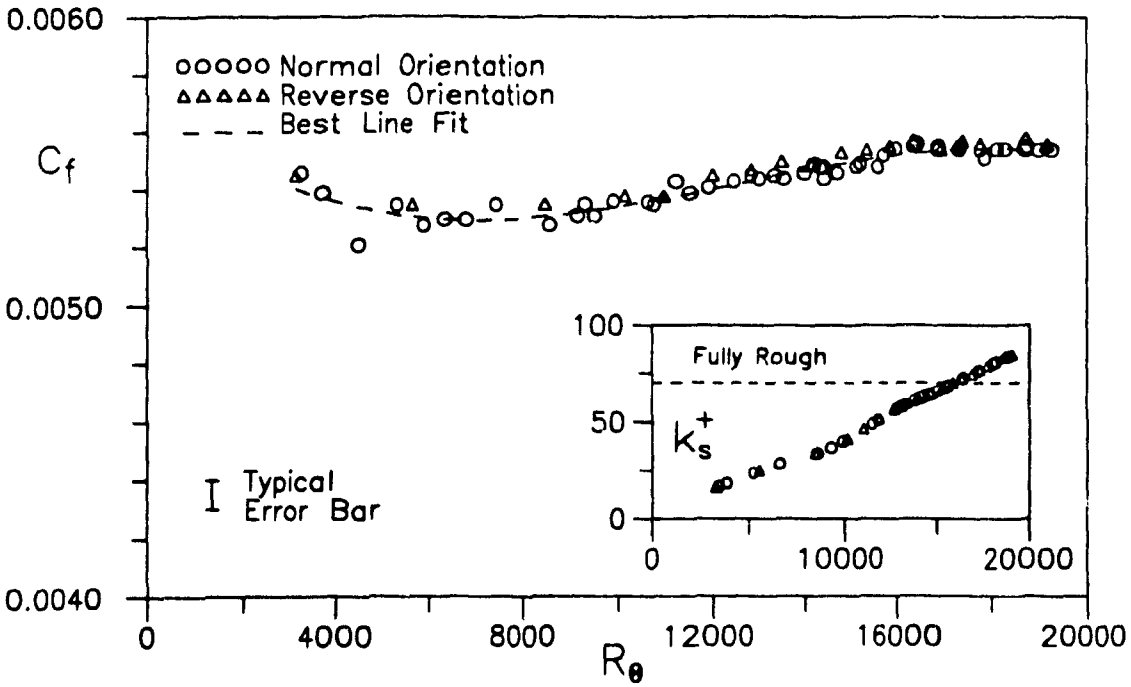

Figure 7.19: Sandpaper #24 Skin Friction Balance Results

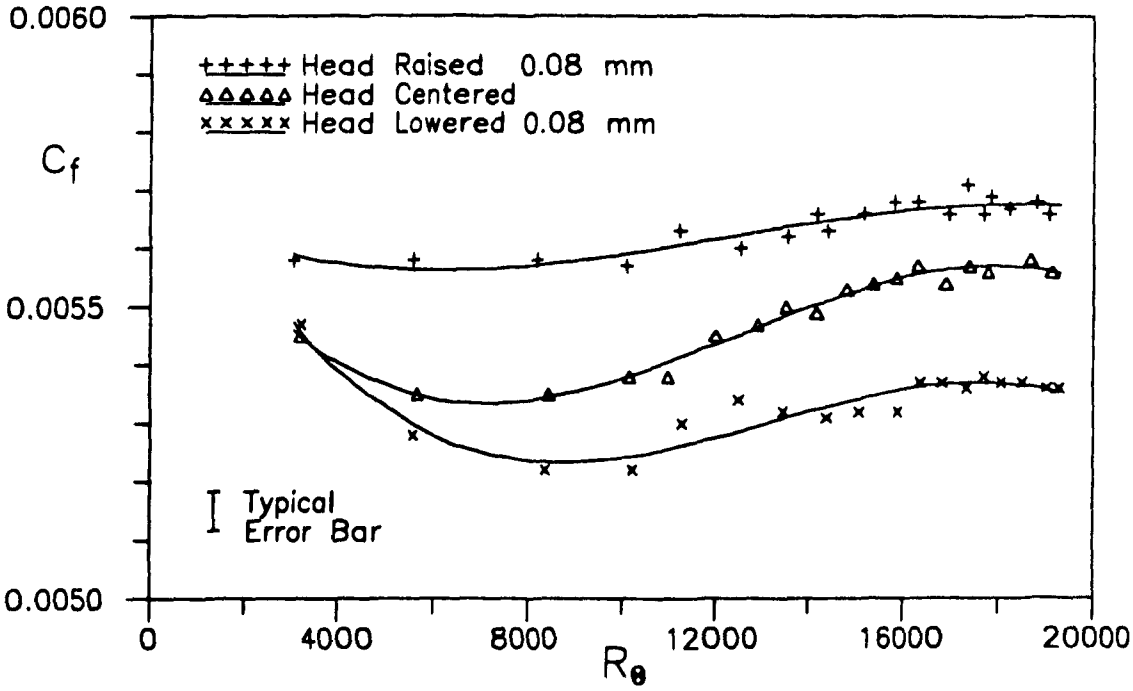

Figure 7.20: Sandpaper #24 Sensitivity of Balance to Vertical Position of Head

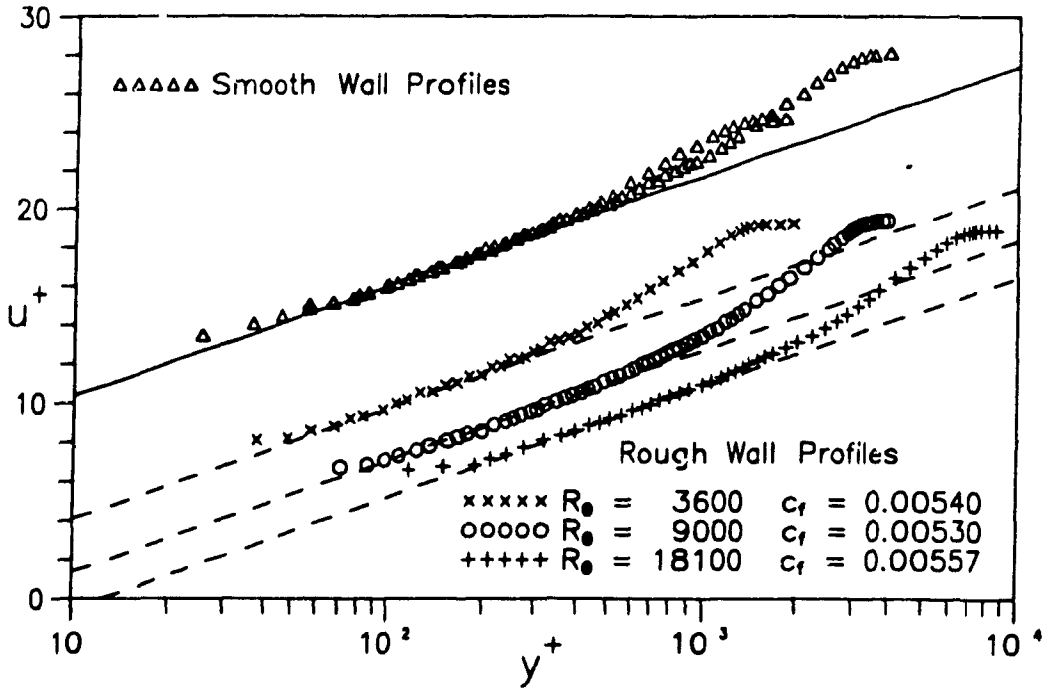

Figure 7.21: Sandpaper #24 Velocity Traverses in Logarithmic Form

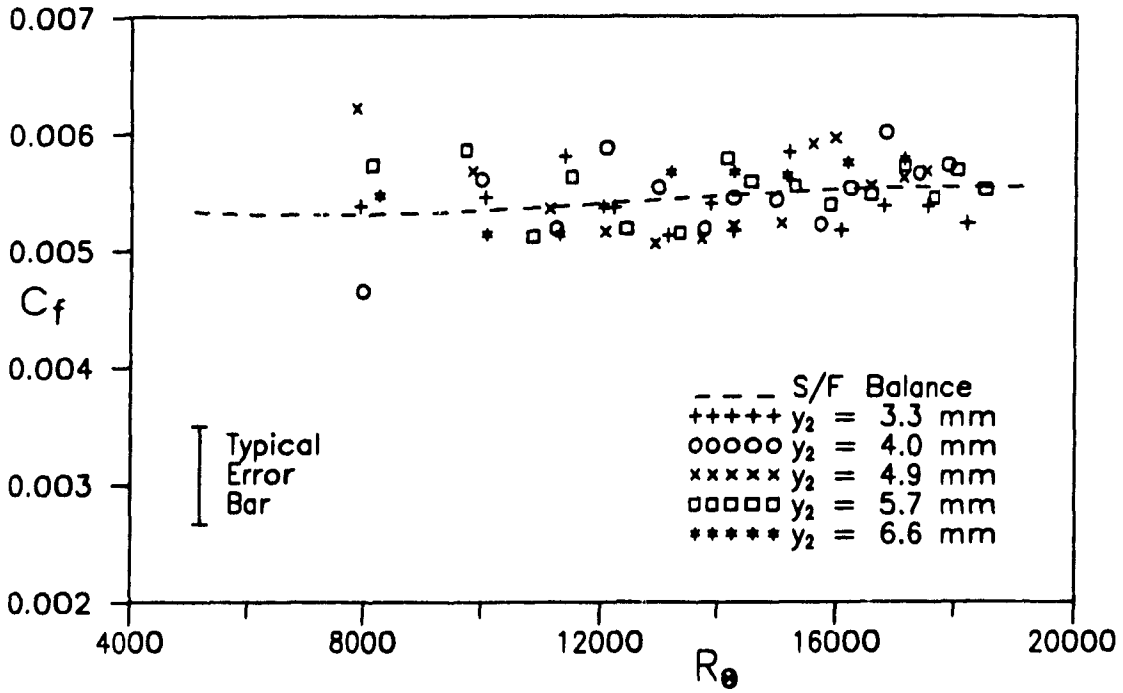

Figure 7.22: Sandpaper #24 Skin Friction Determined using Three Tube Instrument

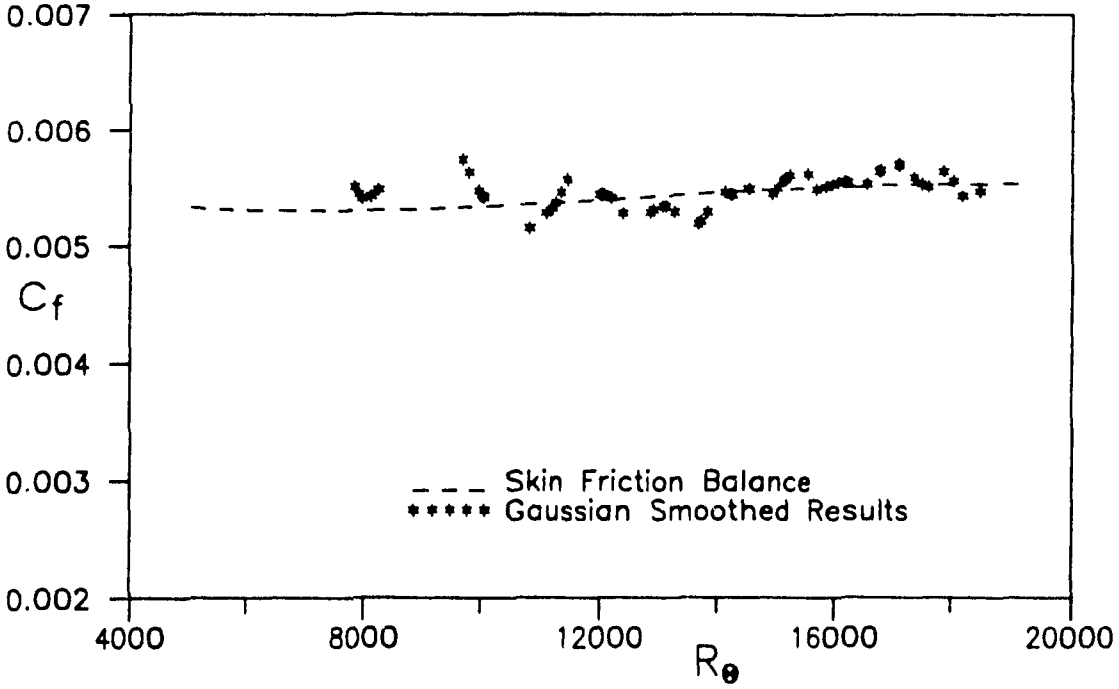

Figure 7.23: Sandpaper #24 Gaussian Smoothed Skin Friction Data

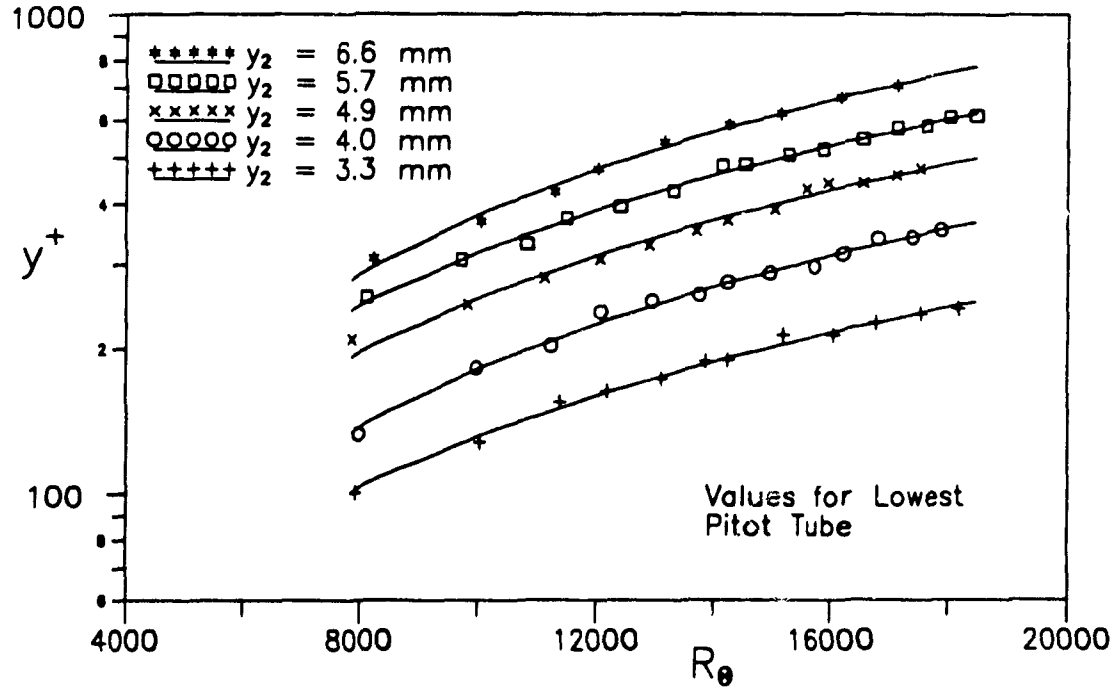

Figure 7.24: Sandpaper #24 y^+ Values for the Lowest Pitot Tube

Chapter 8

CONCLUSIONS AND RECOMMENDATIONS

8.1 Conclusions

- From the theoretical considerations, a one or two tube instrument is insufficient to obtain the skin friction on a surface of unknown roughness with the use of pressure measurements. A three tube instrument is shown to be sufficient provided a logarithmic region of the turbulent boundary layer exists. The skin friction coefficient can be evaluated by means of an analytical expression from pressure data obtained by the three tube instrument.

- Experimentally, the proposed three tube instrument gives good agreement with well known skin friction laws, Preston tubes, and skin friction balance when applied to a smooth surface. The agreement is typically within ± 10 percent; however, at Reynolds numbers, R_θ, below about 8000 a larger discrepancy exists due to the greater difficultly in obtaining accurate measurements of the small pressure differences.

- The results of the three tube instrument also agree with a skin friction balance when applied to two sandpaper roughnesses for a range of the nondimensional roughness parameter k_s^+ from approximately 10 to 85. As with the smooth wall, the agreement is within about ± 10 percent and within the experimental uncertainty. The results are also independent of the vertical position of the instrument provided the instrument is in the logarithmic region of the mean velocity profile.

- A great deal of scatter was observed in the results and this was attributed to the difficulty in accurately measuring the small pressure differences Δ_{12} and Δ_{23}. The accuracy was limited by not only the turbulent fluctuations of these pressures, but also the sequential manner in which the pressures were measured. However, in determining the general trend of the skin friction coefficient by Gaussian smoothing, agreement with the skin friction balance to within ± 5 percent was obtained. This indicates that with improved measurement techniques the three tube instrument is expected to produce more reliable and accurate results.

8.2 Recommendations for Future Work

A great deal more work is needed to further investigate this new instrument and technique for obtaining the skin friction on a rough wall. The following is a short list of suggested research which can be carried out in the immediate future:

- The measurement technique should be improved by incorporating three sensitive pressure transducers for making simultaneous measurement of the three important pressure quantities $\bar{q}_2$, Δ_{12} and Δ_{23}, and a data acquisition system employed for determining mean pressures from the turbulent fluctuations.

- The three tube instrument can be used on surfaces with other roughness geometries, such as transverse bars and wire screens, and on surfaces designed to reduce the skin friction, such as riblets.

- Finally, if greater accuracy can not be achieved using this pressure instrument, then a robust three thermistor instrument may be considered. Such a device could measure the velocity gradient using three vertically aligned horizontal thermistors in the logarithmic region of the turbulent boundary layer.

References

[1] Batchelor, G.K., *The Theory of Homogenous Turbulence*, University Press, Cambridge (1956)

[2] Blanchard, A., *Analyse expérimentale et théoretique de la structure de la turbulence d'une couche limite sur paroi rugueuse*, Univ. of Poitiers (1977)

[3] Bradshaw, P., *An Introduction to Turbulence and its Measurement*, Pergamon Press, Oxford (1971)

[4] Bradshaw, P., et al., *Turbulence (Topics in Applied Physics; v. 12)*, Springer-Verlag, Berlin (1976)

[5] Brown, K.C., Joubert, P.N., The Measurement of Skin Friction in Turbulent Boundary Layers with Adverse Pressure Gradients, *J. Fluid Mech.* **35** p.737 (1969)

[6] Cebeci, T., Smith, A.M.O., *Analysis of Turbulent Boundary Layers*, Academic Press, New York (1974)

[7] Clauser, F.H., Turbulent Boundary Layers in Adverse Pressure Gradients, *J. Aero. Sci.* **21** p.91 (1954)

[8] Clauser, F.H., The Turbulent Boundary Layer, *Advances in Appl. Mech.* **4** p.1 (1956)

[9] Coles, D., The Law of the Wall in Turbulent Shear Flow, *GALCIT* (1954)

[10] Coles, D., The Law of the Wake in the Turbulent Boundary Layer, *J. Fluid Mech.* **1** p.191 (1956)

[11] Coles, D., *Rand Corp.* R-403-PR (1962)

[12] Coles, D., Hirst, E.A., *Proc. Comp. Tur. Bound. Layers,* Stanford (1968)

[13] Davies, P.O., The Behaviour of a Pitot Tube in Transverse Shear, *J. Fluid Mech.* **3** p.441 (1958)

[14] Dickinson, J., et al., Some Experimental Observations of the Law of the Wall Behind Large Eddy Breakup Devices Using Servo-Controlled Skin Friction Balances, *Proc. AIAA-84-0346* (1990)

[15] Gaudet, L., Integral Boundary Layer Parameter Relationships and a Skin Friction Law Derived from a Velocity Profile Family for Two Dimensional Incompressible Flow, *Roy. Aero. Est. Memo* **2080** (1986)

[16] Grabow, R.M., White, C.O., Surface Roughness Effects on Nose Tip Ablation Characteristics, *AIAA Journal* p.605 (1975)

[17] Hama, F.R., Boundary-Layer Characteristics for Smooth and Rough Surfaces, *Trans. Soc. Nav. Arch. Mar. Engrs.* **62** p.333 (1954)

[18] Head, M.R., Rechenberg, I., The Preston Tube as a Means of Measuring Skin Friction, *J. Fluid Mech.* **14** p.1 (1962)

[19] Liu, C.K., et al., *Report MD-15,* Mech. Eng., Stanford (1966)

[20] Ludwieg, H., Tillmann, W., Investigations of the Wall-Shearing Stress in Turbulent Boundary Layers, *NACA TM* **1285** (1950)

[21] MacMillan, F.A., Viscous Effects on Pitot Tubes at Low Speeds, *J. Aero. Sci.* **58** p.837 (1954)

[22] MacMillan, F.A., Experiments on Pitot Tubes in Shear Flow, *Aero. Res. Coun. R & M* **3028** (1956)

[23] Moffat, R.J., Describing the Uncertainties in Experimental Results, *Exp. Thermal and Fluid Sci.* **1** p.3 (1988)

[24] Moody, L.F., Friction Factors for Pipe Flow, *Trans. ASME* **66** (1944)

[25] Moore, W.F., *An Experimental Investigation of the Boundary Layer Development Along a Rough Surface,* Ph.D. Dissertation, U. of Iowa (1951)

[26] Morris, H.M., Flow in Rough Conduits, *Trans. ASME* **120** (1955)

[27] Nikuradse, J., Strömungsgesetzen rauhen Rohren, *Forsch. Arb. Ing. Wes.* **161** (1933)

[28] Ower, E., Pankhurst, R.C., *The Measurement of Air Flow, 5th ed.*, Pergamon Press, Oxford (1977)

[29] Paradis, M.A., Pressure and Velocity Measurements in Subsonic Flow, *Génie Méchanique, Université Laval* (1973)

[30] Patel, V.C., Calibration of the Preston Tube and Limitations on its use in Pressure Gradients, *J. Fluid Mech.* **23** p.185 (1965)

[31] Patel, V.C., Head, M.R., *J. Fluid Mech.* **34** p.371 (1968)

[32] Perry, A.E., Joubert, P.N., Rough-Wall Boundary Layers in Adverse Pressure Gradients, *J. Fluid Mech.* **17** p.193 (1963)

[33] Perry, A.E., Bell, J.B., Joubert, P.N., Velocity and Temperature Profiles in Adverse Pressure Gradient Turbulent Boundary Layers, *J. Fluid Mech.* **25** p.299 (1966)

[34] Perry, A.E., Turbulent Boundary Layers in Decreasing Adverse Pressure Gradients, *J. Fluid Mech.* **26** p.481 (1966)

[35] Perry, A.E, Schofield, W.H., Joubert, P.N., Rough Wall Turbulent Boundary Layers, *J. Fluid Mech.* **37** p.383 (1969)

[36] Pope, A., Rae, W.H., *Low Speed Wind Tunnel Testing.* Wiley, New York (1984)

[37] Prandtl, L., *Über Flüssigkeitsbewegung bei sehr kleiner Reibung,* Proc. III Intern. Math. Congress, Heidelberg (1904)

[38] Prandtl, L., Über den Reibungswiderstand strömender Luft, *Erg. AVA* Göttingen, III series (1927)

[39] Prandtl, L., *Ergebnisse der AVA Gottingen 4,* Oldenbourg, München (1932)

[40] Prandtl, L., Schlichting, H., *Das Widerstand Gesetz rauher Platten,* Werft-Reederei-Hafen (1934)

[41] Preston, J.H., The Determination of Turbulent Skin Friction by Means of Pitot Tubes, *J. Royal Aero. Soc.* **58** p.109 (1954)

[42] Rotta, J.C., On the Theory of the Turbulent Boundary Layer, *NACA TM* **1344** (1950)

[43] Rotta, J.C., *J. Aero. Sci.* **22** p.215 (1955)

[44] Rotta, J.C., Turbulent Boundary Layers in Incompressible Flow, *Progr. Aero. Sci.* **2** p.1 (1962)

[45] Schlichting, H., Experimental Investigation of the Roughness Problem, *NACA TM* **823** (1937)

[46] Schlichting, H., *Boundary Layer Theory, 5th ed.,* McGraw-Hill, New York (1968)

[47] Schoenherr, K.E., Resistance of Flat Surfaces Moving Through a Fluid, *Trans. Soc. Nav. Arch. Mar. Engrs.* **40** p. 279 (1932)

[48] Shaw, R., The Influence of Hole Dimension on Static Pressure Measurements, *J. Fluid Mech.* **7** p.550 (1960)

[49] Smith, D.W., Walker, J.H., Skin-Friction Measurements in Incompressible Flow, *NASA TM* **4231** (1958)

[50] Streeter, V.L., Frictional Resistance in Artificially Roughened Pipes, *Proc. Amer. Soc. Civil Engrs.* **61** p.163 (1935)

[51] Thompson, B.G.J., A New Two-parameter Family of Velocity Profiles for Incompressible Boundary Layers on Smooth Walls, *Aero. Res. Council R&M* **3463** (1967)

[52] Thwaites, B., *Incompressible Aerodynamics,* Clarendon Press, Oxford (1960)

[53] Todd, F.H., Skin Friction Resistance and the Effect of Surface Roughness, *Trans. Soc. Nav. Arch. Mar. Engrs.* **59** p.315 (1951)

[54] Townsend, A.A., *J. Fluid Mech.* **11** p.97 (1961)

[55] Townsend, A.A., *J. Fluid Mech.* **26** p.689 (1966)

[56] Townsend, A.A., *The Structure of Turbulent Shear Flow,* 2^{nd} ed., University Press, Cambridge (1976)

[57] Van Driest, E.R., On Turbulent Flow Near a Wall, *J. Aero. Sci.* **23** p.1007 (1956)

[58] Von Kármán, Th., Über laminare und turbulente Reibung, *ZAMM* **1** p.233 (1921)

[59] Von Kármán, Th., Turbulence and Skin Friction, *J. Aero. Sci.* **1** p.1 (1934)

[60] Wygnanski, I., Newman, B.G., General Description and Calibration of the McGill 3 ft. x 2 ft. Wind Tunnel, *Internal Report Ae4, Mech. Eng., McGill University* (1961)

[61] White, F.M., *Viscous Fluid Flow,* McGraw-Hill, New York (1974)

[62] Young, A.D., Maas, J.N., The Behaviour of a Pitot Tube in a Transverse Pressure Gradient, *Rep. Memor. Aero. Res. Coun.* **1770** (1937)

[63] Young, A.D., *Boundary Layers,* Blackwell Scientific Publications, Oxford (1989)

Supplementary References

[64] Bellhouse, B.J., Schultz, D.L., *Aero. Res. Council R&M* **3445** (1964)

[65] Duffy, J., Norbury, J.F., *J. Roy. Aero. Soc.* **71** p.55 (1967)

[66] Fage, A., Falkner, V.M., *Proc. Roy. Soc.* A **129** p.378 (1930)

[67] Wyatt, L.A., East, L.F., *Roy. Aero. Est. Tech. Rep.* **66027** (1966)

Appendix A

Integral Relations for the Turbulent Boundary Layer

A.1 Integral Definitions

A turbulent boundary layer may be described by its mean velocity profile and turbulence quantities; however, often it is preferable to work with simpler boundary layer quantities which, although not specific to a particular velocity profile, give a great deal of information about the boundary layer of interest. Most of these quantities are derived from integrals involving the boundary layer mean velocity profile.

The *boundary layer thickness*, δ, is first defined as the distance above the wall at which the mean flow velocity, $\overline{u}$ reaches 99 percent of the free-stream mean velocity, $\overline{U}$. This definition is rather arbitrary, but conventional. The boundary layer thickness is difficult to measure accurately, so its definition is more for conceptual value than practical use.

Two other thicknesses are also used to described the boundary layer. The *displacement thickness*, δ^*, is the thickness of a layer of the free-stream which contains the same mass flow rate that is lost in the boundary layer by the action of the wall shear stress. Or, in other words, a stagnant layer of thickness δ^* has the same mass flow defect as the actual boundary layer. Mathematically, it is defined as

$$\delta^* \equiv \int_0^\infty \left(1 - \frac{\overline{u}}{\overline{U}}\right) dy. \tag{A.1}$$

Similarly, *the momentum thickness*, θ, is the thickness of a layer of the free-stream which contains the same momentum that is lost in the boundary layer by the

action of the wall shear stress, and is defined by

$$\theta \equiv \int_0^\infty \frac{\overline{u}}{\overline{U}} \left(1 - \frac{\overline{u}}{\overline{U}}\right) dy. \tag{A.2}$$

A stagnant layer of thickness θ has the same momentum defect as the actual boundary layer. The integrals defining the displacement and momentum thicknesses can be taken between the wall and any upper limit outside the boundary layer, since neither mass flow nor momentum are lost in the free-stream by the action of the wall shear stress.

The ratio of these two thicknesses is an important parameter called the *momentum shape factor*:

$$H \equiv \frac{\delta^*}{\theta}. \tag{A.3}$$

Other shape factors exist for the boundary layer which are defined based on integrals involving the velocity defect law profile, $g(\eta)$, where $\eta \equiv y/\delta$. Two such shape factors are:

$$C_1 \equiv \int_0^1 g(\eta)\, d\eta \tag{A.4}$$

and

$$C_2 \equiv \int_0^1 (g(\eta))^2\, d\eta. \tag{A.5}$$

It can be easily shown that these shape factors are related to the three boundary layer thicknesses given above by the expressions

$$\frac{\delta^*}{\delta} = C_1 \lambda^{-1} \tag{A.6}$$

and

$$\frac{\theta}{\delta} = C_1 \lambda^{-1} - C_2 \lambda^{-2} \tag{A.7}$$

where $\lambda = \sqrt{2/c_f}$.

The ratio $G \equiv C_2/C_1$ is another useful shape factor in boundary layer studies. It's value depends only on the longitudinal pressure gradient, and is equal to approximately 6.1 for a zero pressure gradient boundary layer. This shape factor is related to the momentum shape factor through the expression:

$$H^{-1} = 1 - G\lambda^{-1}. \tag{A.8}$$

A.2 Momentum Integral Equation

The turbulent boundary layer equations can be integrated across the boundary layer to yield what is known as the *momentum integral equation.* Starting with the turbulent boundary layer equations:

$$\frac{\partial \overline{u}}{\partial x} + \frac{\partial \overline{v}}{\partial y} = 0, \tag{A.9}$$

$$\overline{u}\frac{\partial \overline{u}}{\partial x} + \overline{v}\frac{\partial \overline{u}}{\partial y} - \overline{U}\frac{d\overline{U}}{dx} = \frac{1}{\rho}\frac{\partial \tau}{\partial y} \tag{A.10}$$

where

$$\tau = -\rho\overline{u'v'} + \mu\frac{\partial \overline{u}}{\partial y} \tag{A.11}$$

and the smooth wall boundary conditions

$$\overline{u} = \overline{v} = 0 \qquad \text{at} \qquad y = 0,$$

$$\overline{u} = \overline{U}(x) \qquad \text{at} \qquad y \geq \delta, \tag{A.12}$$

the x-momentum equation is integrated from $y = 0$ to $y = h$ where h is beyond the boundary layer thickness. For flow over a flat surface, the total shear stress is zero outside the boundary layer, since the laminar component is zero by virtue of no velocity gradient, and the turbulent shear term is zero by virtue of isotropic turbulence. Thus, the integrated equation is

$$\int_0^h \left(\overline{u}\frac{\partial \overline{u}}{\partial x} + \overline{v}\frac{\partial \overline{u}}{\partial y} - \overline{U}\frac{d\overline{U}}{dx}\right) dy = -\frac{\tau_w}{\rho}. \tag{A.13}$$

From continuity, one has

$$\overline{v} = -\int_0^y \frac{\partial \overline{u}}{\partial x}\, dy \tag{A.14}$$

and upon substitution, gives

$$\int_0^h \left(\overline{u}\frac{\partial \overline{u}}{\partial x} - \frac{\partial \overline{u}}{\partial y}\int_0^y \frac{\partial \overline{u}}{\partial x}\, dy - \overline{U}\frac{d\overline{U}}{dx}\right) dy = -\frac{\tau_w}{\rho}.$$

Now integrating the second term by parts yields

$$\int_0^h \left(2\overline{u}\frac{\partial \overline{u}}{\partial x} - \overline{U}\frac{\partial \overline{u}}{\partial x} - \overline{U}\frac{d\overline{U}}{dx}\right) dy = -\frac{\tau_w}{\rho}$$

and

$$\int_0^h \frac{\partial}{\partial x}\left[\overline{u}(\overline{U}-\overline{u})\right]\,dy + \frac{d\overline{U}}{dx}\int_0^h (\overline{U}-\overline{u})\,dy = \frac{\tau_w}{\rho}.$$

Applying the definitions of δ^* and θ yields

$$\frac{d}{dx}(\theta\overline{U}^2) + \delta^*\overline{U}\frac{d\overline{U}}{dx} = \frac{\tau_w}{\rho}$$

and finally,

$$\frac{d\theta}{dx} + (2+H)\frac{\theta}{\overline{U}}\frac{d\overline{U}}{dx} = \frac{c_f}{2}. \qquad \text{(A.15)}$$

This momentum integral equation describes the balance of forces acting on a slice of the boundary layer of thickness dx. The first term is the change in the fluid's inertia or momentum, while the second and third terms are, respectively, the pressure force and the wall shear stress.

Because of the omission of the terms containing $\overline{u'^2}$ and $\overline{v'^2}$ from the turbulent boundary layer equations, this momentum integral equation is not strictly correct for turbulent flows. When used to determine the skin friction, this omission results in an error of c_f which is typically three percent in the absence of a pressure gradient, and may be considerably larger when a pressure gradient exists.

Appendix B

Consideration of a Two Tube Instrument

In the desire to obtain the simplest instrument to measure skin friction on a wall of unknown roughness, a two tube instrument was considered. As explained in Chapter 5, the pressure difference ΔP between the two tubes of diameter d and separation s will be a function of the seven independent variables:

$$\Delta P = \mathcal{F}(y, \rho, \mu, \tau_w, s, d, k_s) \tag{B.1}$$

where y is some length scale describing the vertical position of the two tubes. Non-dimensionalizing gives

$$\frac{\Delta P s^2}{\rho \nu^2} = \mathcal{F}\left(\frac{s u_\tau}{\nu}, \frac{y}{s}, \frac{k_s}{s}, \frac{d}{s}\right). \tag{B.2}$$

If the pitot tube diameter is small in comparison to both the tube separation and the vertical position of the instrument then the last term is probably not important. Even if large, this term can be fixed geometrically, and having done so, it is no longer a significant criterion of similarity. The non-dimensional pressure difference is then a function of the three remaining criteria of similarity, none of which will be known in practical situations, since the quantities u_τ, y, and k_s are all unknown. Therefore, this pressure difference can not be calibrated directly with the wall shear stress when the other two criteria of similarity are unknown.

This problem led to the consideration of placing the two tube instrument in the logarithmic region of the boundary layer and making use of the fact that the velocity gradient is independent of both viscosity and the surface roughness. In

Chapter 5, the expression

$$u_\tau = \frac{\kappa y_{12}}{\rho u_{12} s}(\overline{P}_1 - \overline{P}_2) \tag{B.3}$$

was derived using this idea, but the problem of the unknown vertical position y_{12} prevents the determination of the skin friction by this method.

However, a third possibility of using a two tube instrument may be considered. This possibility combines the two previous ideas: using the logarithmic distribution of the mean velocity profile and obtaining a calibrated relationship between the wall shear stress and some measurable quantity. For both smooth and rough surfaces, one has

$$\frac{y}{u_\tau}\frac{\partial \overline{u}}{\partial y} = \frac{1}{\kappa}, \tag{B.4}$$

with the understanding that the vertical position y which satisfies this equation is unknown on a rough surface because of its unknown origin. This equation implies that in this region of a turbulent boundary layer, the gradient of the mean velocity at a given vertical position depends only on the fluid density, the wall shear stress and the vertical position. Mathematically, this corresponds to

$$\frac{\partial \overline{u}}{\partial y} = f(\rho, \tau_w, y) \tag{B.5}$$

By considering two pitot tubes and single static tube in the logarithmic region, one can imagine recording two measurements of the time-averaged dynamic pressure at the two different vertical positions, as illustrated in Figure B.1. The partial derivative, $\partial \overline{u}/\partial y$, which is the slope of the velocity profile, could be replaced by the finite difference slope $(\overline{u}_1 - \overline{u}_2)/s$, provided that y is taken to be the vertical position where the true slope is equal to the measured finite difference slope. This position will depend on both the profile shape and the separation between the two pitot tubes. Hence,

$$\frac{\overline{u}_1 - \overline{u}_2}{s} = f(\rho, \tau_w, y_1, s). \tag{B.6}$$

Non-dimensionalizing this expression yields

$$\frac{\overline{u}_1 - \overline{u}_2}{u_\tau} = f\left(\frac{y_1}{s}\right). \tag{B.7}$$

Thus, such an instrument may be calibrated to work on a smooth surface, where the ratio y_1/s is known. In this case, since this ratio is fixed for a given geometry, the measured velocity difference would be proportional to the wall friction

velocity; the calibration would be required to find the correct constant of proportionality for the particular geometry. This instrument, however, could not be applied to a rough wall, because of the uncertainty in the value of y_1. While the function f may be found by calibrating the instrument on a smooth surface, the operating value of y_1/s will be unknown in practice, if the instrument is to be used on a surface of unknown roughness. Hence the utility of such a calibrated two tube instrument is limited to smooth surfaces only.

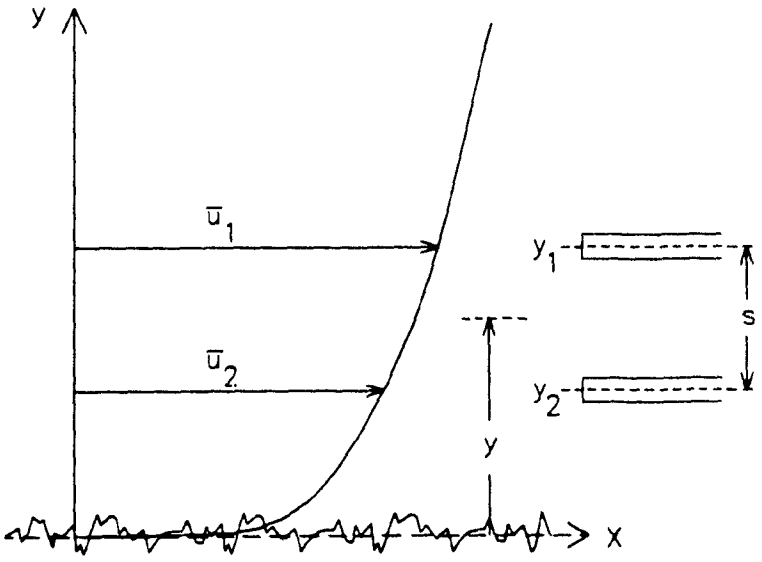

Figure B.1: Consideration of a Two Tube Device

Appendix C

Derivation of the Equations for the Three Tube Instrument

C.1 Pressure Derivation

The proposed method of determining the surface skin friction coefficient makes use of the fact that, in the logarithmic region of the boundary layer, the gradient of the velocity is independent of the viscosity and surface roughness. This statement was shown to be mathematically equivalent to

$$\frac{y}{u_\tau}\frac{\partial \overline{u}}{\partial y} = \frac{1}{\kappa}. \tag{C.1}$$

For smooth walls, this expression is valid when the origin of y is taken at the wall surface; for rough walls, the origin is some specific position, ϵ, below the top of the roughness elements.

Since the proposed instrument measures total pressures and not velocities directly, it is preferable to replace the mean velocity in this expression with the time-averaged mean total pressure. Because of the irrotational nature of the boundary layer, Bernoulli's equation can not be applied. But, by definition of the total pressure at a point, $\overline{P} = \overline{p} + \frac{1}{2}\rho\overline{u}^2$, one may write

$$\rho\overline{u}\partial\overline{u} + \partial\overline{p} = \partial\overline{P} \tag{C.2}$$

where $\overline{p}$ and $\overline{P}$ are the static and total pressures respectively. Now, assuming the static pressure to be constant at any x-wise position in the boundary layer, one has

$$\rho\overline{u}\frac{\partial \overline{u}}{\partial y} = \frac{\partial \overline{P}}{\partial y}, \tag{C.3}$$

which, upon substitution, gives

$$\frac{y}{u_\tau}\frac{1}{\rho\overline{u}}\frac{\partial\overline{P}}{\partial y}=\frac{1}{\kappa}. \tag{C.4}$$

The instrument, shown schematically in Figure 5.2, is designed to measure $\partial\overline{P}/\partial y$ at two very closely spaced vertical positions. Approximating the exact derivative $\partial\overline{P}/\partial y$ by the finite difference slope $\delta\overline{P}/\delta y$ yields, for the upper two pitot tubes,

$$\frac{y_{12}}{u_\tau}\cdot\frac{\overline{P}_1-\overline{P}_2}{\rho u_{12}s_{12}}=\frac{1}{\kappa}, \tag{C.5}$$

and for the lower two,

$$\frac{y_{23}}{u_\tau}\cdot\frac{\overline{P}_2-\overline{P}_3}{\rho u_{23}s_{23}}=\frac{1}{\kappa}, \tag{C.6}$$

where

$$u_{ij}\equiv\frac{\overline{u}_i+\overline{u}_j}{2}, \tag{C.7}$$

$$y_{ij}\equiv\frac{1}{2}(y_i+y_j), \tag{C.8}$$

and

$$s_{ij}\equiv y_i-y_j. \tag{C.9}$$

The vertical position y_{ij} is unknown on a rough wall because of the unknown origin for y; nevertheless, it is easily shown that

$$y_{12}-y_{23}=\frac{y_1-y_3}{2}=\frac{s_{12}+s_{23}}{2}. \tag{C.10}$$

Hence the unknown vertical locations are eliminated by subtracting the two difference equations, resulting in

$$\frac{1}{u_\tau}=\frac{\rho}{\kappa}\frac{2}{s_{12}+s_{23}}\left(\frac{u_{12}s_{12}}{\Delta_{12}}-\frac{u_{23}s_{23}}{\Delta_{23}}\right), \tag{C.11}$$

where

$$\Delta_{ij}\equiv\overline{P}_i-\overline{P}_j. \tag{C.12}$$

It must be emphasized here that only through the use of two simultaneous equations can the vertical positions be eliminated, and that this elimination is necessary since the y_{ij} values are unknown on a rough surface.

Once again, one is faced with velocity quantities which are not measured directly. The mean velocities u_{12} and u_{23} are eliminated in favour of measurable pressure quantities using

$$\overline{u}_1 = \sqrt{\frac{2}{\rho}(\overline{P}_1 - \overline{p})} = \sqrt{\frac{2}{\rho}(\overline{P}_2 - \overline{p} + \Delta_{12})}, \tag{C.13}$$

and

$$\overline{u}_3 = \sqrt{\frac{2}{\rho}(\overline{P}_3 - \overline{p})} = \sqrt{\frac{2}{\rho}(\overline{P}_2 - \overline{p} - \Delta_{23})}. \tag{C.14}$$

Thus,

$$\begin{aligned} u_{12} &= \frac{1}{2}\left(\sqrt{\frac{2}{\rho}(\overline{P}_2 - \overline{p})} + \sqrt{\frac{2}{\rho}(\overline{P}_2 - \overline{p} + \Delta_{12})}\right) \\ &= \frac{1}{2}\sqrt{\frac{2}{\rho}(\overline{P}_2 - \overline{p})}\left(1 + \sqrt{1 + \frac{\Delta_{12}}{\overline{P}_2 - \overline{p}}}\right) \\ &\approx \sqrt{\frac{2}{\rho}(\overline{P}_2 - \overline{p})}\left(1 + \frac{1}{4}\frac{\Delta_{12}}{\overline{P}_2 - \overline{p}}\right), \end{aligned} \tag{C.15}$$

provided Δ_{12} is small compared to $\overline{P}_2 - \overline{p}$. Similarly,

$$u_{23} \approx \sqrt{\frac{2}{\rho}(\overline{P}_2 - \overline{p})}\left(1 - \frac{1}{4}\frac{\Delta_{23}}{\overline{P}_2 - \overline{p}}\right). \tag{C.16}$$

Substituting into our previous expression and simplifying gives

$$\frac{1}{u_\tau} = \frac{2}{s_{12} + s_{23}}\sqrt{\frac{2\rho}{\kappa^2}(\overline{P}_2 - \overline{p})}\left(\frac{s_{12}}{\Delta_{12}} - \frac{s_{23}}{\Delta_{23}} + \frac{1}{4}\frac{s_{12} + s_{23}}{\overline{P}_2 - \overline{p}}\right). \tag{C.17}$$

Introducing the skin friction coefficient,

$$c_f \equiv \frac{\tau_w}{\frac{1}{2}\rho\overline{U}^2} = 2\left(\frac{u_\tau}{\overline{U}}\right)^2, \tag{C.18}$$

one arrives at

$$c_f = \frac{\kappa^2(s_{12} + s_{23})^2}{8\overline{Q}\overline{q}_2}\left(\frac{s_{12}}{\Delta_{12}} - \frac{s_{23}}{\Delta_{23}} + \frac{s_{12} + s_{23}}{4\overline{q}_2}\right)^{-2}, \tag{C.19}$$

where the free-stream and boundary layer dynamic pressures, respectively, are defined as

$$\overline{Q} \equiv \frac{1}{2}\rho\overline{U}^2, \tag{C.20}$$

and

$$\overline{q}_2 \equiv \overline{P}_2 - \overline{p}. \tag{C.21}$$

Finally, this expression can be simplified by introducing the geometrical quantity $\varsigma \equiv s_{23}/s_{12}$, to give

$$c_f = \frac{\kappa^2(1+\varsigma)^2}{8\overline{Q}\overline{q}_2}\left[\frac{1}{\Delta_{12}} - \frac{\varsigma}{\Delta_{23}} + \frac{1+\varsigma}{4\overline{q}_2}\right]^{-2}. \tag{C.22}$$

This is the final expression for the skin friction coefficient, in which c_f can be determined based on the four measurable quantities $\overline{Q}$, $\overline{q}_2$, Δ_{12} and Δ_{23}, plus the geometrical ratio ς.

C.2 Alternative Derivation

In the above derivation of the skin friction equation for the three tube instrument two linearizing approximations were used. First, the pressure gradient taken at the midpoint of two pitot tubes was approximated by the finite pressure difference divided by the separation between the tubes. Secondly, the velocities at tubes 1 and 3 were related to that at tube 2 using Taylor series expansions to first order terms. It can be shown that keeping terms of higher order in these expansions results in a final equation for the skin friction coefficient given by

$$c_f = \frac{\kappa^2(1+\varsigma)^2}{8\overline{Q}\overline{q}_2}\left[\frac{1}{\Delta_{12}} - \frac{\varsigma}{\Delta_{23}} + \frac{1+\varsigma}{4\overline{q}_2} + \frac{\varsigma\Delta_{23} - \Delta_{12}}{16\overline{q}_2^2}\right]^{-2}. \tag{C.23}$$

This equation differs from the previously derived expression by a correction term which is typically two to three orders of magnitude smaller than the preceding terms; hence, the expansion to higher order terms has a negligible effect on calculated values of the skin friction coefficient.

An alternative derivation of the three tube equation can be derived by considering the velocity gradient rather than the pressure gradient. The velocity gradient at the midpoint between two pitot tubes is approximated by the finite velocity difference slope, and then the velocities themselves are expanded in terms of the dynamic pressure $\overline{q}_2$ and the small pressure differences in the same manner as above. However, one finds that if only first order terms are kept in the Taylor series expansions of $\overline{u}_1$ and $\overline{u}_3$ then the equation for the skin friction coefficient will be missing the $(1+\varsigma)/4\overline{q}_2$ term, which will introduce a significant

error in the calculated values of c_f. Hence, in this alternative approach terms up to second order must be kept in the approximations until the final expression is arrived at. Once this final expression has been obtained, terms in $\Delta_{ij}/\bar{q}_2$ of second order or higher may be neglected, yielding the same skin friction equation as given by the pressure derivation.

Appendix D

Skin Friction Balance Measurements

As mentioned in Section 6.1.8, the skin friction balance measures not only the wall shear stress, but also forces due to inclination, acceleration, and pressure gradient. Vibrational acceleration, which is mostly a high frequency phenomenon, can be filtered electronically from the balance output. However, inclination and pressure gradient forces remain as components of the total force measured by the balance. This appendix briefly describes the how these two forces arise and how they were removed from the skin friction balance measurements.

D.1 Inclination

Since the static pressure in the test section of the wind tunnel is lower than the room static pressure, the floor of the wind tunnel rises at the center under the load due to this pressure difference. This displacement is small, but significant enough to change the inclination of the skin friction balance with respect to the horizontal plane. Since the balance is located downstream from the center of the floor in the test section, the rise in the floor results in an additional apparent "drag force" on the balance, which increases with free-stream velocity.

The balance measurements were corrected for this extra "force" by running the wind tunnel over the entire range of velocities with the balance covered, to isolate the inclination from dynamic effects. The measured inclination "force" was then subtracted from all succeeding balance readings.

D.2 Pressure Gradient

The small favourable pressure gradient which exists in the wind tunnel also produces an extra "drag" on the skin friction balance in the same direction as the inclination "drag". Because the pressure gradient is proportional to the free-stream dynamic pressure, the effect on the skin friction coefficient is constant and independent of free-stream velocity. The magnitude of the pressure gradient effect on the balance is calculated as follows.

The force on the balance head due to the pressure gradient is determined by integrating the pressure around the edge of the head. For a head of radius r and thickness h, the force is given by

$$F_x = \int_0^{2\pi} \frac{d\bar{p}}{dx} r(1 - \cos\theta) rh \cos\theta \, d\theta = -\pi r^2 h \frac{d\bar{p}}{dx}. \tag{D.1}$$

Thus, the force per unit area of the head is

$$\frac{F_x}{A} = -h\frac{d\bar{p}}{dx} = hQ \text{ x Const.} \tag{D.2}$$

where the constant is was found to be 0.023m^{-1} for the smooth wall and estimated from the change in the displacement thickness to be at most about 0.028m^{-1} for the fully rough wall.

Hence, the additional "skin friction" due to this pressure gradient force is

$$(c_f)_{\nabla p} = \frac{F_x/A}{Q} = h \text{ x Const.} \tag{D.3}$$

For the smooth wall measurements, $h = 0.95$ mm which gives an effective c_f of about 0.00002, or less than one percent of the true skin friction. For the thickest sandpaper, $h \approx 1.83$ mm, producing an effective c_f of about 0.00005. One again this is less than one percent of the true skin friction coefficient.

All skin friction coefficients determined from the skin friction balance were adjusted by these small amounts to correct for the contribution due to the longitudinal pressure gradient.

Appendix E

Three Tube Measurement Corrections

Various measurement corrections were considered and, where necessary, applied in the evaluation of Eq. 5.15. These corrections included modifications to the measured pressures involving the three tube apparatus and modifications to the geometrical factor ς. The pressure measurement corrections which were considered included effects on both pitot and static tube measurements due to viscosity, turbulence and wall proximity. The displacement corrections resulted from the effective displacement of the pitot tubes due to streamline curvature ahead of the apparatus. This appendix briefly describes these corrections and the extent to which these corrections were necessary.

E.1 Pressure Measurement Corrections

All pressure measurements performed with a pitot or static pressure tube are subject to corrections due to many effects which may be present. These corrections normally include the effects of yaw and pitch misalignment, viscosity, turbulence, Mach number, vibration, velocity gradients and wall proximity. In the present investigation, Mach number and vibration effects were both negligibly small. Misalignment was also negligible as the flow direction in the wind tunnel is well defined by the walls. Moreover, the effect due to a non-uniform velocity profile was taken into account in the displacement corrections described below. Thus, only corrections for viscosity, turbulence and wall proximity were considered for the pressure measurements.

E.1.1 Viscosity Correction

Total pressure measurements taken with a very small pitot tube are subject to errors due to viscosity. MacMillan [21] investigated this phenomenon and found that the error is dependent on the Reynolds number based on the pitot tube inner diameter, and that the error is negligible for a Reynolds number greater than about 300. In the present experiment, the hypodermic tubing used as pitot tubes have an inner diameter of only 0.40 mm, resulting in a Reynolds number as small as 175 at low velocity, but most often exceeding 300. At the lowest Reynolds number, the total pressure recorded by the pitot tube would be larger than the true total pressure by approximately 0.5 percent of the dynamic pressure. Thus, the measurement of the dynamic pressure, $\overline{q}_2$, was in error by at most 0.5 percent, and was therefore not corrected. However, since the values of Δ_{12} and Δ_{23} were typically one order of magnitude smaller than $\overline{q}_2$, these pressure measurements were corrected for the effect of viscosity. The correction procedure involved estimating the dynamic pressures $\overline{q}_1$ and $\overline{q}_3$ using the recorded values of $\overline{q}_2$, Δ_{12} and Δ_{23}, then re-calculating Δ_{13} and Δ_{23} from the corrected values of the total pressures. These corrections were performed, but generally found insignificant for two reasons. In most cases the Reynolds number greatly exceeded the limit of importance determined by MacMillan; furthermore, the corrections made to $\overline{P}_i$ and $\overline{P}_j$ nearly cancelled in determining the correction to Δ_{ij}.

E.1.2 Turbulence Correction

Turbulence affects the pressure measurements of both pitot and static tubes. For a pitot tube, the effect of velocity fluctuations is to increase the total energy per unit volume, and therefore the total pressure, so that the pitot tube would read the pressure

$$\overline{P} = \overline{p} + \frac{1}{2}\rho\overline{u}^2 + \frac{1}{2}\rho\left(\overline{u'^2} + \overline{v'^2} + \overline{w'^2}\right). \tag{E.1}$$

In isotropic turbulence, this is equivalent to a total pressure increase of $\frac{3}{2}\rho\overline{u'^2}$.

The effect of turbulence on the reading of a static pressure tube is much more complicated since it depends on the spectral distribution of the turbulence. When the turbulence scale is small compared to the static hole diameter, the turbulence at several static holes is uncorrelated, and the static pressure is expected to read high by $\rho\overline{u'^2}$ in an isotropic turbulent flow. On the other hand, when the

turbulence scale is large in comparison to the static hole diameter, the pressure becomes increasingly correlated at the many static holes, as if the flow direction were inclined to the tube at any instant. Hence, the static pressure would be expected to read low by an amount corresponding to a time-averaged fluctuation of angle of misalignment. In this case, the correction has been shown to be $-\rho\overline{u'^2}$. Investigations [28] have shown that the recorded static pressure is closer to the true static pressure than either of these two extremes, and therefore, a static pressure correction due to turbulence is normally not necessary.

The correction to the dynamic pressure is therefore due to the total pressure alone. In general the dynamic pressure will be

$$\overline{P} - \overline{p} = \frac{1}{2}\rho\overline{u}^2\left(1 + \frac{\overline{u'^2}}{\overline{u}^2} + \frac{\overline{v'^2}}{\overline{u}^2} + \frac{\overline{w'^2}}{\overline{u}^2}\right). \tag{E.2}$$

Hence in isotropic turbulence, the recorded dynamic pressure will be greater than the true dynamic pressure by a factor of $1 + 3\overline{u'^2}/\overline{u}^2$. In the foregoing experiment, the free-stream r.m.s. turbulence is about 0.4 percent of the free-stream velocity, yielding a correction of less than 0.01 percent to the measurement of the free-stream dynamic pressure. In the boundary layer, however, the turbulence is not isotropic and the fluctuations are considerably greater. Near the wall, the r.m.s. velocity fluctuations may be as large as eight, four and six percent for the u, v, and w components, respectively [63]. Even this amount of turbulence yields a theoretical correction to the dynamic pressure of less than five percent. Since this represents an upper limit on the correction, and the true correction is difficult to determine in practice, this correction to the present measurements was not performed, but incorporated instead into the uncertainties of the measurements. It is believed, however, that the omission of this correction to the pressure measurements may be significant, particularly close to the wall.

E.1.3 Wall Proximity Correction

An experimental investigation by MacMillan [22] demonstrated that the total pressure measured with a pitot tube must be corrected when the measurements are made within 1.7 pitot tube diameters of a solid boundary. The correction, however, is normally quite small, reaching a maximum of three percent when the pitot tube rests on the surface. In the present experiment, the lowest of the three

tubes in the apparatus is never closer than 1.5 diameters from the wall, and at this distance the correction is a negligible 0.1 percent. Hence, corrections to the total pressure measurements due to wall proximity were completely neglected.

E.2 Displacement Corrections

Displacement effects arise due to the curvature of a streamline which stagnates upon a body. For a pitot tube, which measures the total pressure, the location in the flow where this total pressure exists is not at the center of the pitot tube, but rather at the location where the stagnation streamline would exist if the pitot tube were not present. In a fully developed flow, or one which is slowly changing longitudinally, the location of the measured total pressure is that of the stagnation streamline upstream of the pitot tube. Thus, if the streamline has curvature near the pitot tube, then the position of the pitot tube must be corrected to account for this streamline curvature. This type of correction is called a displacement correction.

Streamline curvature may arise due to the influence on the flow of nearby objects, or by transverse velocity or pressure gradients. No displacement effect exists for a single circular pitot tube in a uniform flow, since, by symmetry, the stagnation streamline will be a straight line on the axis of the pitot tube. In this experiment, streamline curvature near the three tube instrument arises by the presence of more than one pitot tube, by the influence of the wall, and by the sheared velocity profile found in the boundary layer. The displacement effect on a circular pitot tube due to a non-uniform upstream velocity profile has been examined experimentally by several researchers; hence, this correction can be made based on empirical results. However, for the wall and pitot tube interference no such experimental results exists; therefore, the corrections were investigated by theoretical considerations.

E.2.1 Effect of Velocity Shear on a Pitot Tube

The effect of a velocity shear was accounted for using experimental results of Davies [13] for a circular pitot tube in a shear layer. These results indicate that the ratio of the displacement, d_e, to the pitot tube diameter, d_0, is a function of

α, where α is defined in the upstream velocity profile

$$\overline{u} = \overline{u}_c \left(1 + \frac{2\alpha}{d_0}(y - y_c)\right), \tag{E.3}$$

and $\overline{u}_c$ is the upstream velocity on the pitot tube centerline, at $y = y_c$. Now, the true velocity gradient in the region of the three tube instrument is not linear, but logarithmic, and therefore α will vary with y. To determine the corresponding α at a particular position in the logarithmic region, one equates the actual velocity gradient with that given in the above relation. Hence,

$$\frac{\partial \overline{u}}{\partial y} = \frac{u_\tau}{\kappa y} = \frac{2\alpha \overline{u}_c}{d_0} = \frac{2\alpha u_\tau}{d_0}\left(\frac{1}{\kappa}\ln\frac{y_c u_\tau}{\nu} + B - \frac{\Delta u}{u_\tau}\right). \tag{E.4}$$

Thus,

$$\alpha = \frac{d_0}{2\kappa y_c}\left(\frac{1}{\kappa}\ln y_c^+ + B - \frac{\Delta u}{u_\tau}\right)^{-1}. \tag{E.5}$$

For simplification, the final term was given the typical value of approximately 0.06 for the smooth wall measurements and 0.12 for the rough walls. This expression then becomes

$$\alpha \approx 0.08\frac{d_0}{y_c} \quad \text{(Smooth)} \tag{E.6}$$

$$\alpha \approx 0.16\frac{d_0}{y_c} \quad \text{(Rough)} \tag{E.7}$$

To apply this correction, α was calculated for each of the three pitot tubes, based on their diameters and vertical positions. The displacement correction was then determined based on the function

$$\frac{d_e}{d_0} = 1.16\alpha - 2.22\alpha^2 \tag{E.8}$$

which best approximates the experimental data of Davies [52]. Generally, these corrections were quite small, so that the assumptions made are justified.

E.2.2 Interference Due to Wall and Neighbouring Tubes

Since no available empirical results exist for the displacement effects on a pitot tube due to the interference of neighbouring pitot tubes, the problem was considered theoretically. The real situation was mathematically simulated, as shown in Figure E.1, by replacing the boundary layer flow by a two-dimensional shear layer

of constant velocity gradient, $\partial\overline{u}/\partial y$, and replacing the pitot tubes by three two-dimensional point sources. The wall effect was taken into account using three image sources and a reflected upstream velocity profile. The six point sources were taken to lie on the y-axis at positions $\pm y_1$, $\pm y_2$, and $\pm y_3$, and their strengths were chosen to produce two-dimensional open bodies whose widths far downstream were equal to the actual diameters of the pitot tubes. This two-dimensional model was a very inaccurate representation of the real three-dimensional situation; however, since the displacements predicted by a two-dimensional model would be considerably larger than the true three-dimensional displacements, it was hoped that by using this model, one could predict negligible displacement effects in three dimensions.

Since the upstream shear flow is rotational, a velocity potential does not exist for this situation. However, continuity is always satisfied, so a stream function does exist. The upstream boundary layer flow, including the image flow, was taken to be a uniform shear flow

$$\overline{u}(y) = -u_0 - \beta|y|, \tag{E.9}$$

where the values for u_0 and β were chosen to best approximated the actual velocity profile in the logarithmic region. The stream function for this flow is

$$\psi_0 = -u_0|y| - \frac{1}{2}\beta|y|y. \tag{E.10}$$

The purpose for having chosen this boundary layer profile rather than a more accurate logarithmic profile, was that since $\nabla^2\psi_0 = \beta$, a constant, this stream function can be superimposed with those of the point sources. A more complicated stream function would result in a superimposed flow not satisfying the momentum equation.

The stream function for each source and image is given by

$$\psi_n = \mathrm{Im}\left\{\frac{m_n}{2\pi}\ln(z - iy_n)\right\}, \tag{E.11}$$

so that the total stream function for this flow is then

$$\psi = -u_0|y| - \frac{1}{2}\beta|y|y + \sum_{n=1}^{3}\mathrm{Im}\left\{\frac{m_n}{2\pi}\ln(z^2 + y_n^2)\right\}, \tag{E.12}$$

where

$$z = x + iy, \tag{E.13}$$

and

$$m_n = d_0 \left| \frac{\partial \psi_0}{\partial y} \right|_{y=y_n} . \tag{E.14}$$

Typical values of u_0, β and the y_n's were substituted into Eq. E.12. The stagnation points were found by simultaneously solving the equations

$$\frac{\partial \psi}{\partial y} = 0, \quad -\frac{\partial \psi}{\partial x} = 0. \tag{E.15}$$

The locations of stagnation streamlines were then determined far upstream, allowing the displacements to be determined. It was discovered that for all three tubes, the stagnation streamlines originate from upstream positions closer to the wall. The curvature of these streamlines is greatest for the outer of the three, and least for the one closest to the wall.

Since the displacement effects are accounted for in Eq. 5.15 through the quantity ς, only the ratio of the distances between the stagnation streamlines is important and not the distances themselves. This ratio was calculated and found to be well within two percent of the value of the ratio s_{23}/s_{12}, even in the expected worst case values of u_0, β and y_n. In three dimensions there will certainly be much less streamline curvature than in the two-dimensional model, therefore it was assumed that in three dimensions the effects would be small enough to ignore. This conclusion was in agreement with the 8:1 scale smoke tunnel tests which showed no detectable streamline curvature due to interference effects.

An error analysis was performed to determine how significant is the uncertainty in ς on the value of c_f determined by Eq. 5.15. The results showed that an uncertainty in ς of 25 percent contributes at most about one percent to the overall uncertainty in c_f. Hence, it was concluded that neglecting these displacement corrections was relatively inconsequential to the final result, even when the corrections to ς are significant.

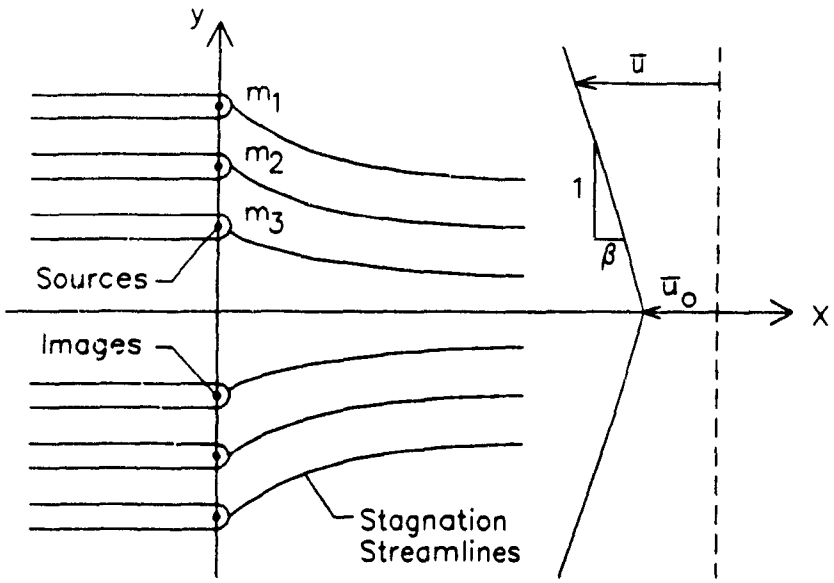

Figure E.1: Mathematical Model for the Determination of the Pitot Tube Displacement Corrections